# High-mobility graphene in 2D periodic potentials

## Dissertation

zur Erlangung des Doktorgrades der Naturwissenschaften (Dr. rer. nat)
der Fakultät Physik der Universität Regensburg

vorgelegt von

## Andreas Sandner

aus Dollnstein

unter Anleitung von Prof. Dr. Dieter Weiss

September 2017

Das Promotionsgesuch wurde am 03.05.2017 eingereicht.
Das Promotionskolloquium fand am 31.01.2018 statt.

Die Arbeit wurde von Prof. Dr. Dieter Weiss angeleitet.

Prüfungsausschuss:
Vorsitzende: Prof. Dr. Milena Grifoni
1. Gutachter: Prof. Dr. Dieter Weiss
2. Gutachter: Prof. Dr. Christian Schüller
weiterer Prüfer: Prof. Dr. Josef Zweck

# Contents

# List of Figures

# CHAPTER 1

# Introduction

Solid state physics has been studied for centuries with focus on electrical, magnetic or mechanical properties of different materials. During the past decades, the spotlight increasingly moved towards 2D electron systems, exhibiting unique phenomena compared to bulk crystals. Two-dimensional electron gases (2DEGs) are commonly realized in transistor-like semiconductor structures such as MOSFETs[1], HEMTs[2] or quantum wells, and mobilities can be even higher than $10^7$ $\mathrm{cm}^2/\mathrm{Vs}$ in AlGaAs/GaAs heterostructures [1]. After all, the 2DEG is not an intrinsic semiconductor property and needs to be formed with gating and modulation-doping techniques in MOSFET and HEMT structures, respectively.

This changed with the first successful isolation of graphene, a monolayer of graphite, by Novoselov and Geim [2]. Graphene is a 2D sheet of carbon atoms, arranged in a honeycomb lattice structure, and features remarkable mechanical and electronic properties. Since its discovery in 2004, graphene has attracted a huge amount of attention and the research field as well as the funding has expanded extensively. Many people expect graphene to be a promising material for a variety of possible applications. One characteristic that can be emphasized is graphene's high intrinsic carrier mobility up to room temperature that would be ideal for transistor devices and could potentially replace the state-of-the-art Si-technology. However, the lack of a band gap in single-layer graphene is a major drawback and hinders the utilization of graphene-based structures in this field. Nevertheless, there might be various applications where the outstanding properties of graphene can be employed: Among others, graphene can be used as an integral part of composite materials [3] (similar to carbon-fiber-reinforced

---

[1] metal-oxide-semiconductor field-effect transistor

[2] high-electron-mobility transistor

polymer), as an electrode for flexible and transparent displays [4], or as material for supercapacitors [5].

This work focuses on hBN-graphene van der Waals heterostructures and their investigation via transport experiments. For this purpose, we introduced a dry-transfer stacking technique for 2D crystals in our lab and fabricated a huge number of high-quality hBN-graphene hybrid structures. The stacks were analyzed in magnetotransport experiments and/or superposed with an additional 2D superlattice potential, subsequently. In this way, we could probe and characterize different commensurability effects stemming from the induced superlattice potential and report their influence on transport properties in graphene.

The first sections of this thesis address the fundamental and inherent properties of graphene and the advantages of graphene-hBN heterostructures over prevalently-used graphene on $SiO_2$ substrates. Moreover, the moiré superlattice, resulting from an alignment of graphene and hBN crystals, and the corresponding recursive Hofstadter spectrum will be discussed. Subsequently, commensurability effects in lateral superlattices - well-known and intensively studied in conventional 2DEGs - will be introduced for weak and strong potential modulation in graphene. Then, the various fabrication steps for the samples, including the fundamental stacking procedure and the patterning of local graphene gates, and the experimental setup will be discussed.

Our first goal was to implement the transfer procedure and regularly achieve high-mobility hBN-graphene heterostructures. In chapter 6, we report some of our experiments on graphene on hBN and encapsulated graphene that confirm progress and enhanced sample quality. We routinely observe ballistic transport in our devices with mobilities exceeding 100 000 $\mathrm{cm^2/Vs}$ and were able to investigate interaction-driven quantum Hall effects, such as quantum Hall ferromagnetism [6, 7] and the fractional quantum Hall effect [8, 9], in several samples.

The encapsulation of graphene between hBN significantly increases the bulk carrier mobility of graphene, and in chapter 7, we show that any further top-down patterning step does not necessarily degrade the intrinsic quality of the graphene sheet. The high sample quality can be preserved in graphene-based antidot lattices and we successfully probed pronounced commensurability features in antidot arrays with lattice constants down to 50 nm.

Antidot lattices show a nice realization of classical transport in mesoscopic systems and commensurability features arise from a correspondence of the patterned array with cyclotron orbits [10, 11]. In chapter 8, we study the interplay between a moiré and an imposed antidot superlattice potential and discuss their influence on magnetotransport measurements. Commensurability features can be characterized at various densities and be assigned to the antidot and the moiré potential. We observe a suppression of the antidot features by approaching the satellite Dirac points of the moiré potential, accompanied with a distinct superposition of the classical features with Shubnikov-de Haas oscillations.

In chapter 9, we discuss a new method for imposing lateral superlattice potentials, employing a local few-layer graphene patterned bottom gate [12]. The patterned graphene gate can be easily implemented in our stacking procedure, and by tuning the local bottom gate and the global back gate, we can consistently move between the unipolar and bipolar transport regime. In this way, we are able to report Weiss oscillations [13] in the weakly modulated unipolar regime and antidot peaks [14] for strong modulation in a bipolar gate configuration.

# CHAPTER 2

## Fundamental properties of graphene

Graphene is a 2D monolayer of graphite, arranged in a hexagonal honeycomb lattice of carbon atoms. It has outstanding material properties such as high stiffness and thermal stability. Additionally, graphene has unique electronic properties such as a linear dispersion relation of the band structure in the vicinity of the Dirac points, followed by a quasi-relativistic description of the charge carriers. Moreover, there are the electric field effect to tune the charge carrier density and many more interesting features of graphene. Graphene has a high intrinsic mobility due to its potentially nearly defect free lattice structure. But graphene on $SiO_2$ is influenced by various scattering mechanisms and the mobility is limited to several thousand $cm^2/Vs$. As a consequence, one can change the substrate to a more suitable one (e.g. hexagonal boron nitride) or even remove the substrate (suspended graphene), and the mobilities can be enhanced to a few hundred thousand $cm^2/Vs$. After that, the quantum Hall effect and *pn*-junctions in graphene will be discussed.

## 2.1 Allotropes of carbon

There are at least two allotropes of carbon that are quite common and universally known. On the one hand graphite, whose name stems from its ability to leave marks on paper and other objects *(ancient greek: graphein)*. Graphite is still a principal component of modern pencils. On the other hand there is diamond, which has various applications because of its exceptional properties, e.g. as cutting and polishing tools. Although both materials, graphite and diamond, are consisting of carbon atoms, they have very different characteristics. In diamond all p-orbitals are bound, forming a $sp^3$-hybridized crystal without any free elec-

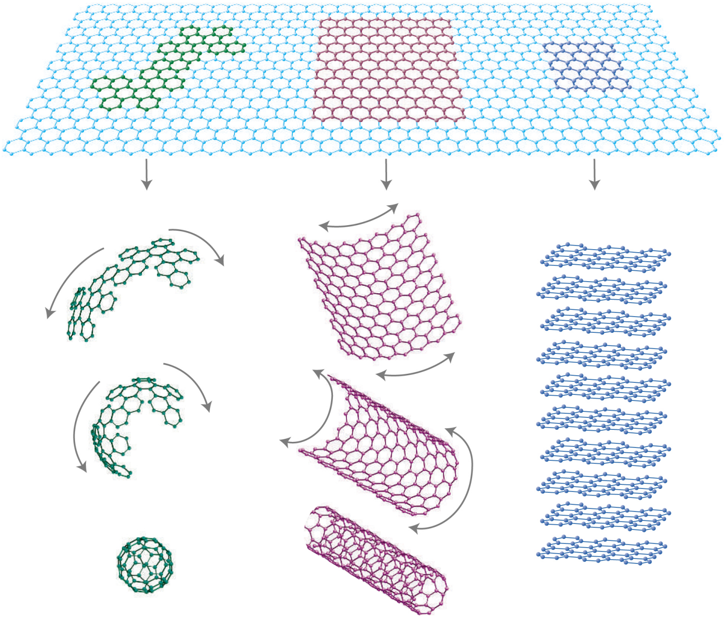

**Figure 2.1:** Graphene is a 2D basic building block for other sp$^2$-bonded carbon materials of different dimensions. It can be wrapped up into 0D buckyballs, rolled into 1D nanotubes and stacked into 3D graphite. Fig. from [15].

trons that could be used for charge transfer. So the electronic conductivity in diamond is very weak. In graphite, each carbon atom forms covalent bonds to its three close neighbors, and the additional p$_z$-orbital is perpendicular to the sp$^2$-hybrid orbitals and forms a $\pi$-bond. The sp$^2$-hybridization is the reason for the significantly higher conductivity of graphite [16]. Graphite is build up by many 2D carbon sheets, stacked on top of each other, which are bound with relatively weak van der Waals forces to each other.

The first theoretical studies of the bandstructure of 2D carbon layers, named graphene, were done back in the 1940s by Wallace [17], but it took more than 30 more years to isolate graphene for the first time. Eizenberg and Blakely managed to get a monolayer of carbon by phase condensation on the surface of a carbon-doped nickel single crystal. However, the graphene sheet was an integral layer of a 3D structure. Despite this first breakthrough, the existence of freestanding, infinitely sized 2D crystals was considered not realistic due to thermal fluctuations at finite temperatures. This has been the common belief for several years, because well-established theories showed that the divergent distribution of thermal fluctuations in low-dimensional crystals can lead to a displacement of the atoms in the lattice in the order of the magnitude of the atomic distances [18]. Many different experiments showed exactly this behavior and so the only way to get graphene was to isolate it as an integral part of 3D structures with matching lattice constants. Nevertheless, freestanding 2D carbon has been a theoretical system for graphene and its allotropes for many years.

This changed when K. S. Novoselov and A. K. Geim isolated graphene by mechanical exfoliation in 2004 [19]. Since graphite is build up by weakly coupled graphene layers, monolayer graphene is peeled off by chance with “Scotch tape” and gently rubbed on a Si/SiO$_2$ substrate. From now on, there was the possibility to explore graphene structures on different substrates, as suspended membranes or in suspension. For their significant discovery of graphene, Novoselov and Geim were awarded the Nobel prize in 2010 and started the fast-growing field of graphene research.

As already mentioned, graphene has been a basic concept for the theoretical description of different allotropes of carbon. Besides 3D graphite and 2D graphene, there are 0D buckyballs and 1D carbon nanotubes. Buckyballs are spherical carbon molecules that can be characterized by the number of carbon atoms. Carbon nanotubes are one-dimensional, tube-shaped carbon structures with diameters of a few nanometers. One interesting feature of these carbon structures is that all of them have the same hexagonal lattice structure and can be built with graphene. For this, graphene can be wrapped up into buckyballs, rolled into nanotubes and stacked into graphite (see Fig. 2.1). So graphene is the fundamental structure for all the mentioned carbon allotropes.

## 2.2 Lattice and band structure of graphene

Monolayer graphene consists of a planar, hexagonal lattice, where each carbon atom has three nearest neighbors and four valence electrons. This lattice structure is caused by the sp$^2$-hybridized orbitals in the $x-y$-plane that bind with an angle of 120° with their neighbors, the so called $\sigma$-bond. Only three of the four valence electrons of carbon form a covalent bond. The p$_z$-orbitals are sticking out of plane, forming the binding $\pi$-band and the antibinding $\pi^*$-band. The lateral overlap of the $p_z$-orbitals leads to a delocalized cloud of electrons, both over and under the carbon lattice plane. Since the delocalized electrons are extended laterally across the $x-y$-plane, graphene really is a two-dimensional electron gas (2DEG).

The hexagonally arranged carbon atoms, forming the graphene lattice, are shown in Fig. 2.2. The unit cell (dashed lines in Fig. 2.2a) consists of two carbon atoms A and B that give rise to two sublattices with their lattice vectors

$$\vec{a_1} = a\,(1,0)\,, \qquad\qquad \vec{a_2} = a\left(-\frac{1}{2},\frac{\sqrt{3}}{2}\right), \tag{2.1}$$

where $a = 2.46$ Å is the lattice constant. The corresponding reciprocal lattice is hexagonal, too, featuring the high symmetry points Γ, M, K and K’. Here, the Dirac points K and K’ in the corners of the graphene Brillouin zone (BZ) are of particular interest (see Fig. 2.2b). Wallace calculated the energy bands and the

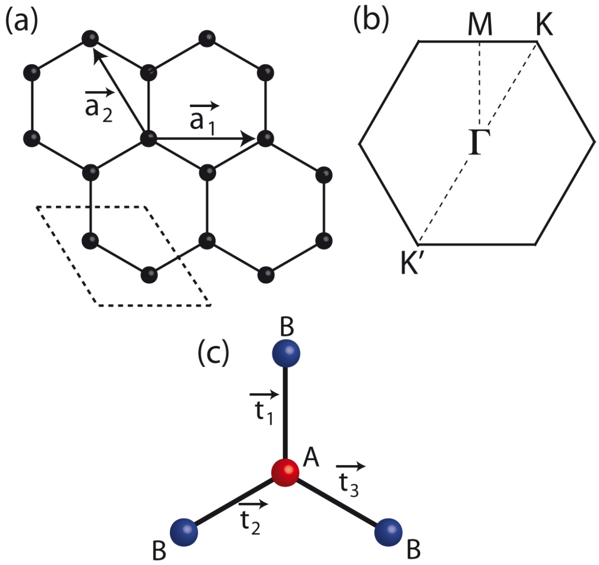

**Figure 2.2:** **(a)** Lattice structure of graphene with lattice unit vectors $\vec{a_1}$ and $\vec{a_2}$. The unit cell (dashed lines) consists of 2 atoms. **(b)** The reciprocal lattice with high symmetry points Γ, K, K' and M. **(c)** Each A Atom (red) is surrounded by 3 B neighbors (blue). The vectors $\vec{t_1}$, $\vec{t_2}$ and $\vec{t_3}$ connect the A atom with the B atoms of the other sublattice. Fig. adapted from [20].

corresponding bandstructure of graphene back in 1947 [17]. The bandstructure and the essential low-energy dispersion can be calculated employing a "tight-binding approach" [16], where the eigenfunctions of graphene $\Psi_i(\vec{k},\vec{r})$ (i=1,...,n) can, similar to other crystalline solids, be written as a linear combination of Bloch functions $\Phi_{i'}(\vec{k},\vec{r})$ and corresponding coefficients $C_{ii'}(\vec{k})$ [20]:

$$\Psi_i(\vec{k},\vec{r}) = \sum_{i'=1}^{n} C_{ii'}(\vec{k})\Phi_{i'}(\vec{k},\vec{r}) \tag{2.2}$$

Accordingly, eigenenergies of this system can be obtained with the following ansatz:

$$E_i(\vec{k}) = \frac{\langle \Psi_i \mid H \mid \Psi_i \rangle}{\langle \Psi_i \mid \Psi_i \rangle} = \frac{\sum\limits_{j,j'=1}^{n} H_{jj'}(\vec{k}) C^*_{jj'} C_{jj'}}{\sum\limits_{j,j'=1}^{n} S_{jj'}(\vec{k}) C^*_{jj'} C_{jj'}}, \tag{2.3}$$

with $H_{jj'}(\vec{k}) = \langle \Psi_j \mid H \mid \Psi_{j'} \rangle$ and $S_{jj'}(\vec{k}) = \langle \Psi_j \mid \Psi_{j'} \rangle$. The equation above needs to be minimized with respect to the coefficient $C^*_{jj'}$, resulting in the secular equation [20]:

$$\det[\mathbf{H} - E\mathbf{S}] = 0 \tag{2.4}$$

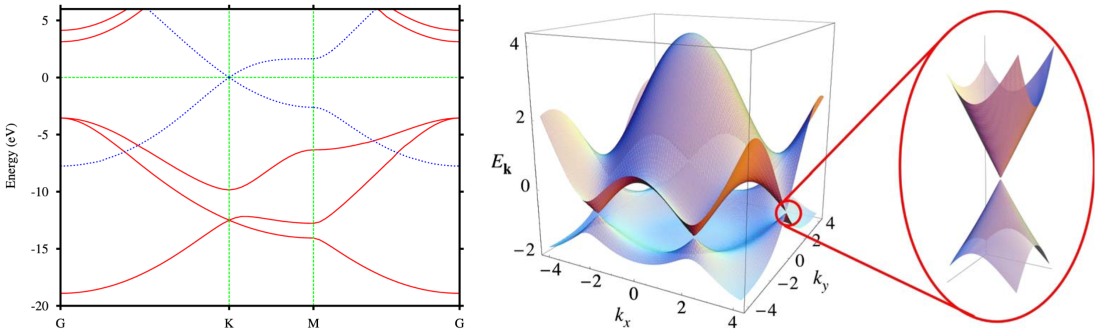

**Figure 2.3:** Band structure of graphene. The left figure shows the band structure of single layer graphene. Red lines are $\sigma$-bands and dotted blue lines are $\pi$-bands. The right one is a 3D plot of the electronic energy dispersion in graphene with its cone-like structure. Fig. from [23, 24].

Consequently, the determinant needs to vanish. As a simple first order approximation, only the next neighbor interaction will be taken into account. So just $H_{AA}$, $H_{BB}$ and $H_{AB}$ need to be evaluated, where A and B are the two atoms of the graphene unit cell. After solving the equations above, the energy dispersion relation of graphene reads as [16]:

$$E(\vec{k_x}, \vec{k_y}) = \pm\gamma_0 \sqrt{1 + 4\cos\left(\frac{\sqrt{3}k_x a}{2}\right)\cos\left(\frac{k_y a}{2}\right) + 4\cos^2\left(\frac{k_y a}{2}\right)}, \tag{2.5}$$

where $k_x$ and $k_y$ are components of the corresponding wavevectors, $a = 0.246$ nm is the lattice constant and $\gamma_0 \approx 3.2$ eV is the hopping integral [16, 21]. The resulting band structure is shown in Fig. 2.3.

The energy dispersion of graphene has six points, where valence and conduction band touch, and the non-equivalent points K and K' are resulting from the two basis atoms in the graphene unit cell. For small energies, in the vicinity of the Dirac points, the energy dispersion is linear in $\vec{k}$. This linear low-energy relationship gives graphene its unique electronic properties [15, 20, 22].

## 2.3 Dirac fermions and pseudospin

Looking closely at the Dirac points of graphene, the linear dispersion relation can be described by two cone-like structures that touch at the K- and K'-points (see Fig. 2.3). For ideal graphene, the Fermi energy is located exactly at the position of the charge neutrality point. But in realistic graphene devices, the Fermi energy can significantly differ from the Dirac energy. Furthermore, the linear dispersion relation only holds for low energy particles with $|E| \leq 1$ eV and can be well-described by the Dirac equation for massless fermions [25, 26].

The Dirac equation describes quantum particles with spin 1/2 (fermions). States with positive and negative energies are conjugated, being described by different components of the same spinor wavefunction [25]. The energy spectrum can be expressed by the following dispersion relation:

$$E(\vec{k}) = \pm\hbar v_F|\vec{k}|, \tag{2.6}$$

where the sign indicates if the charge carriers are located in the conduction band ($\pi^*$-band) or in the valence band ($\pi$-band). $v_F \approx 10^6$ m/s is the Fermi velocity for carriers in graphene, replacing the speed of light [15, 2, 27]. The low-energy Dirac fermions in the vicinity of the K and K' points can be characterized by the spectrum of the Dirac-like Hamiltonian:

$$\hat{H}_K = \hbar v_F \begin{pmatrix} 0 & k_x - ik_y \\ k_x + ik_y & 0 \end{pmatrix} = \hbar v_F \vec{\sigma} \cdot \vec{k}, \tag{2.7}$$

$$\hat{H}_{K'} = \hbar v_F \begin{pmatrix} 0 & k_x + ik_y \\ k_x - ik_y & 0 \end{pmatrix} = \hbar v_F \vec{\sigma}^* \cdot \vec{k}, \tag{2.8}$$

where $\vec{\sigma} = (\sigma_x, \sigma_y)$ is the 2D vector of the Pauli matrices ($\vec{\sigma}^*$ the complex conjugate) and $\vec{k}$ is the wavevector of the quasiparticles [22]. Here, the Pauli matrices represent the pseudospin that affiliates the charge carriers to one of the sublattices A and B [24]. The pseudospin in graphene is an additional degree of freedom, analogous to the spin symmetry [15, 28]. So all in all, graphene has two different quantum numbers for charge carriers, causing a fourfold degeneracy of states. The eigenfunctions, as solutions of the Hamilton operators in the vicinity of the Dirac points, can be written as [24, 29]:

$$\Psi_{\pm,K}(\vec{k},\vec{r}) = \frac{1}{\sqrt{2}} \begin{pmatrix} e^{-i\theta(\vec{k})/2} \\ \pm e^{i\theta(\vec{k})/2} \end{pmatrix} e^{i\vec{k}\cdot\vec{r}}, \tag{2.9}$$

$$\Psi_{\pm,K'}(\vec{k},\vec{r}) = \frac{1}{\sqrt{2}} \begin{pmatrix} e^{i\theta(\vec{k})/2} \\ \pm e^{-i\theta(\vec{k})/2} \end{pmatrix} e^{i\vec{k}\cdot\vec{r}}, \tag{2.10}$$

where the two-component spinor structure is related to the pseudospin of the system. Each graphene sublattice is responsible for one of the weakly interacting valleys of the dispersion and the pseudospin differentiates between the contributions of each sublattice [22, 30]. The projection of the pseudospin on the momentum $\vec{p} = \hbar\vec{k}$ is called chirality. Chirality is a conserved quantity and has important implications on electronic transport in graphene [31, 32]. In particular a non-trivial Berry phase ins associated with the rotation of the 1/2-pseudo spinor. A rotation of the angle in momentum space $\theta(\vec{k}) = \arctan\,(k_y/k_x)$ by $2\pi$ means a phase shift of the wavefunctions by $\pi$, and thus, the spinors will change sign [29]. This phase shift by $\pi$ is called Berry phase [33].

## 2.4 Electric field effect in graphene

The ability to manipulate the electronic properties of a material by applying an external voltage has a huge impact on modern electronic devices. The electric field effect allows to tune the charge carrier density in a semiconductor structure and consequently, to change the electric current through it [19]. This effect is equally important in graphene. One feature that differentiates monolayer graphene from conventional 2DEG structures is the absence of a band gap. The conduction and the valence band touch at the K-points of the energy dispersion. So the Fermi level can be shifted consistently between the valence and the conduction band, corresponding to hole and electron conduction, respectively. In this way, the induced carrier density in graphene can easily exceed $10^{12}$ cm$^{-2}$ [15].

This effect can be experimentally utilized in graphene flakes on a Si/SiO$_2$ wafer. The heavily doped Si wafer acts as a global back gate and the SiO$_2$ layer serves as a dielectric between gate and graphene sheet. Hence, the charge carrier density in the biased graphene flake can be tuned by applying an external potential to the Si back gate. Figure 2.4 shows a characteristic gate response of a monolayer graphene flake and schematics of the position of the Fermi level. The electrical resistivity of graphene has a maximum at the Dirac point, where the carrier density has a minimum (charge neutrality point). For undoped graphene the Dirac point should be at $V_g = V_{cnp} = 0$, where $V_g$ is the applied back gate voltage and $V_{cnp}$ the voltage that needs to be applied to get to the charge neutrality point. But in most realistic devices, especially in graphene on SiO$_2$, there is additional intrinsic/ extrinsic doping and $V_{cnp} \neq 0$.

The high, but finite resistivity peak at the Dirac point can be explained in terms of disorder. This means, in the inevitable presence of disorder, caused by interactions with the substrate or inhomogeneities, regions with electron-rich and hole-rich puddles will arise. These puddles could explain graphene's anomalous non-zero minimal conductivity at zero average carrier density [34]. The carrier inhomogeneity can be determined by analyzing the broadening of the resistivity peak. Generally, the disorder-induced carrier density fluctuation is a good indicator for the sample quality, being as low as $\delta n \approx 10^{10}$ cm$^{-2}$ in graphene-hexagonal boron nitride (hBN) heterostructures and $\delta n < 10^{8}$ cm$^{-2}$ in suspended graphene [35, 8, 36].

A simple approximation for the back gate induced charge carrier density in graphene on SiO$_2$ can be given with a standard capacitor model. If the lateral dimensions of the graphene flake are much bigger than the thickness of the oxide, the assumption of a plate capacitor is justified. Then, the carrier density on a 300 nm SiO$_2$ substrate can be written as [37]:

$$n = \frac{\epsilon_0 \epsilon_r}{de}(V_g - V_{cnp}) \approx 7.2 \cdot 10^{10}\ \mathrm{cm}^{-2}\mathrm{V}^{-1} \cdot (V_g - V_{cnp}), \tag{2.11}$$

where $\epsilon_0$ is the electric constant, $\epsilon_r = 3.9$ is the dielectric constant of SiO$_2$,

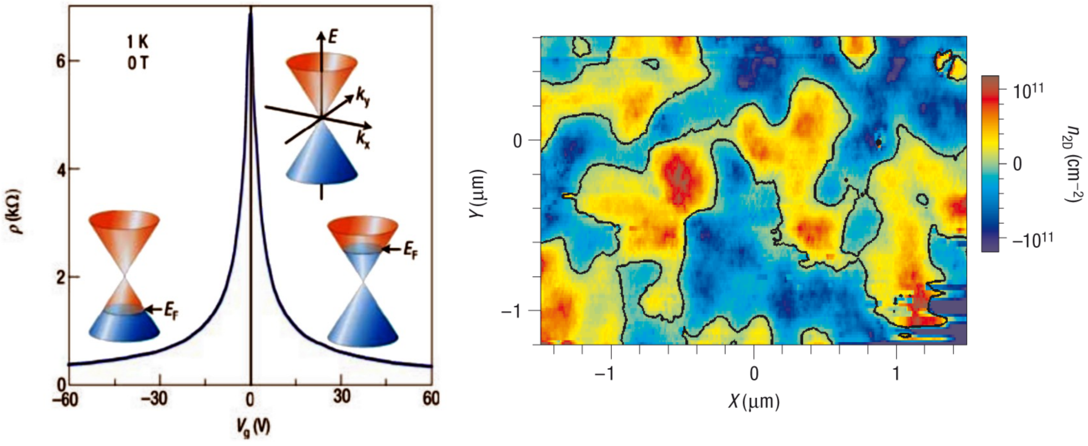

**Figure 2.4:** Electric field effect in graphene. The left figure shows the ambipolar electric field effect in graphene: The Fermi level can be shifted upwards or downwards by applying a positive and a negative gate voltage, respectively. The resistance has a maximum at the Dirac point, where the charge carrier density has a minimum. The right figure depicts a color map of the spatial density variations in a graphene flake for zero average carrier density. The blue regions correspond to holes and the red regions to electrons. Fig. from [15, 34].

$d = 300$ nm is the thickness of the $SiO_2$ layer and $e$ is the elementary charge. Using this model, the conductivity of the graphene sheet can be calculated with:

$$\sigma = en_s\mu = \frac{\epsilon_0\epsilon_r}{d}\mu(V_g - V_{cnp}) = C_g\mu(V_g - V_{cnp}), \tag{2.12}$$

where $C_g = \epsilon_0\epsilon_r/d$ is the gate coupling constant and $\mu$ is the charge carrier mobility in the sample. The relation above is one possibility to estimate the mobility of a gated graphene device.

Nevertheless, there are some situations where the plate capacitor model is not valid. In the previous case, the graphene flake is much larger than the thickness of the oxide layer and there is a global gate. Consequently, the electric field lines are parallel to each other and perpendicular to the graphene plane. This is no longer true for smaller lateral dimensions, such as graphene nanoribbons [38, 39] or locally acting gates [40, 41, 42]. Here, more elaborate simulation techniques for the estimation of the charge carrier density need to be applied.

## 2.5 Transport and scattering mechanisms in graphene

In contrast to theory, realistic graphene structures always contain defects and impurities [43, 44]. Additionally, the interaction with the underlying substrate induces edges and ripples [45]. These perturbations strongly influence the electronic properties of graphene and significantly decrease graphene's quality by acting as scattering centers and introducing spatial inhomogeneities [22]. The mentioned influences to graphene's transport properties cannot be neglected, and from a theoretical point of view, two different transport regimes can be considered in terms of electron mean free path $l_e$ and length of the graphene channel $L$.

On the one hand, there is the ballistic transport regime, where $l_e > L$. Here, charge carriers can run across the graphene sheet without any scattering event. In this case, transport can be characterized in terms of the Landauer-Büttiker formalism and the conductivity reads as [29]:

$$\sigma_L = \frac{4e^2}{h}\frac{L}{W}\sum_{n=1}^{\infty} T_n, \tag{2.13}$$

where $T_n$ are the transmission probabilities in all available transport modes. This approach leads to the following expression for the ballistic conductivity as a function of finite carrier density [46]:

$$\sigma_L(n_s) = \frac{2e^2\sqrt{n_s}}{\hbar} \tag{2.14}$$

Considering evanescent modes in the ballistic regime, this theory leads to a minimum conductivity at the charge neutrality point [22, 47]:

$$\sigma_{min} = \frac{4e^2}{\pi h} = 4.92 \cdot 10^{-5}\Omega^{-1} \tag{2.15}$$

On the other hand, for $l_e < L$, carrier experience elastic and inelastic scattering and enter the diffusive transport regime. In this case, the carrier density $n_s$ in graphene is much larger than the inherent impurity density $n_i$ and the system is homogeneous. Accordingly, diffusive transport can be described by the semiclassical Boltzmann theory, where scattering off various impurities is taken into account. At low temperatures the conductivity can be written as a function of the total relaxation time $\tau$ [30]:

$$\sigma_B = \frac{e^2 v_F \tau}{\hbar}\sqrt{\frac{n_s}{\pi}}, \tag{2.16}$$

where $\tau$ depends on the dominant scattering mechanisms in the sample. The most prominent and common ones include Coulomb scattering at charged impurities, short-range scattering at defects, and electron-phonon interactions. In the following part, I want to discuss some relevant scattering processes in graphene.

### 2.5.1 Phonon scattering

At finite temperatures, electron-phonon interactions are a dominant scattering mechanism in graphene structures. Phonons can be considered as an intrinsic scattering source, limiting the mobility even in absence of extrinsic scattering. In 3D bulk materials, we differentiate between two regimes in terms of temperature. On the one hand high temperatures $T > \Theta_D$, where the resistivity scales as $\rho(T) \propto T$, and on the other hand $\rho(T) \propto T^5$ for $T < \Theta_D$. Since the Debye temperature $\Theta_D$, the temperature scale where all phonon modes are populated, is approximately 2300 K in graphene, we would expect a $T^5$ dependence of the resistivity in our experimental range.

But this is not the case for graphene, where the Fermi surface is substantially smaller than in metals, and only a small fraction of acoustic phonons with momenta $k_{ph} < 2k_F$ can scatter with electrons [48]. Thereby phonon energies $\hbar\omega_{ph}$ are small in comparison to the Fermi energy of the electrons $E_F$, and scattering events can be considered as quasi-elastic. This restriction leads to a new temperature scale for electron-phonon scattering, the Bloch-Grüneisen temperature:

$$\Theta_{BG} = 2\hbar v_{ph} k_F / k_B < \Theta_D. \tag{2.17}$$

With the sound velocity $v_{ph}$ and the Fermi wave vector $k_F = \sqrt{n_s \pi}$, $\Theta_{BG}$ can be determined as

$$\Theta_{BG} = 54\sqrt{n_s}\ \mathrm{K}, \tag{2.18}$$

where $n_s$ is the carrier density in units of $10^{12}$ cm$^{-2}$ [49].

Again, we need to consider two different regimes, the high and the low temperature regime. A related experiment by Efetov *et al.* can be seen in Fig. 2.5 [48]. For $T \gg \Theta_{BG}$, we are in the equipartition limit and the Bose-Einstein distribution function for phonons is $N_{ph} \approx k_B T/\hbar\omega_{ph}$. As a result, there is a linear dependence of the scattering rate on $T$, and hence, the resistivity $\rho$ is linear in $T$ [49]. On the other hand, there is the low temperature (Bloch-Grüneisen) regime $T < \Theta_{BG}$, where $\hbar\omega_{ph} \approx k_B T$. Here, the scattering rate is strongly reduced by the more complicated occupation factor of the phonons. However, in the low temperature limit $T \ll \Theta_{BG}$, a $\rho \propto T^4$ relation can be obtained [49].

### 2.5.2 Coulomb scattering

Coulomb scattering stems from long-range interactions of charge carriers and charged impurities close to the graphene sheet. In this context, charged impurities can be trapped ions in the underlying substrate, fabrication residues, or intentionally deposited adatoms. Employing a semiclassical approach using the Boltzmann equation, one can estimate the influence of charged impurity scattering on transport characteristics in graphene. It was predicted that the backscattering probability is proportional to $\sqrt{n_s}/n_i$, where $n_s$ is the charge carrier density and $n_i$ is the charge impurity density in graphene [50]:

$$\tau_i \propto \frac{\sqrt{n_s}}{4 v_F n_i \pi^{3/2}} \tag{2.19}$$

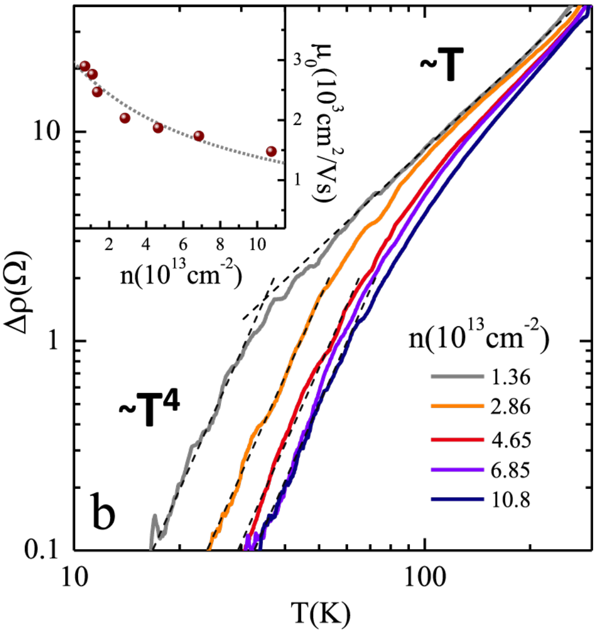

**Figure 2.5:** Temperature dependent part of the resistivity as a function of temperature for different densities $n$. $\Delta\rho(T)$ scales as $T^4$ for low T and crosses over into a linear $T$ dependence at higher $T$. The inset shows the mobility $\mu_0$ as a function on density $n$. Fig. from [48].

Considering this relation, the conductivity at high carrier densities ($n_s \gg n_i$) can be written as:

$$\sigma_i = \frac{Ce^2}{h}\frac{n_s}{n_i}, \tag{2.20}$$

where $C$ is a dimensionless parameter characterizing the scattering strength [22]. This formula suggests a linear increase of conductivity with charge carrier density for a transport regime mostly influenced by Coulomb scattering. The linear behavior was observed in various experiments on graphene on $SiO_2$, confirming charged impurities as dominant scattering source [15, 43].

Chen *et al.* obtained a factor of $C \approx 20$ in their experiments, considering dielectric screening from the substrate and random-phase approximation. They conducted a systematic study on Coulomb scattering in graphene by depositing a variable amount of adatoms (potassium) onto a initially clean graphene surface in ultrahigh vacuum (UHV) [43]. Fig. 2.6a illustrates conductivity versus gate voltage for a pristine sample and three different potassium doping concentrations taken at $T = 20$ K in UHV. A striking result of this experiment is the shift of the Dirac Point with variation of the adatom concentration. The back gate position of the charge neutrality point becomes more negative with increasing doping, because of the shift of the Fermi level induced by the $K$ adatoms. Additionally, the conductivity as a function of the gate voltage becomes more linear for increasing impurity concentration, which is is good agreement with equation 2.20 for dominant Coulomb scattering. At the same time, there is a noticeable broadening of the width of the minimum conductivity region, indicating a reduction of the sample quality. This decrease in mobility is highlighted in Fig. 2.6b, where the

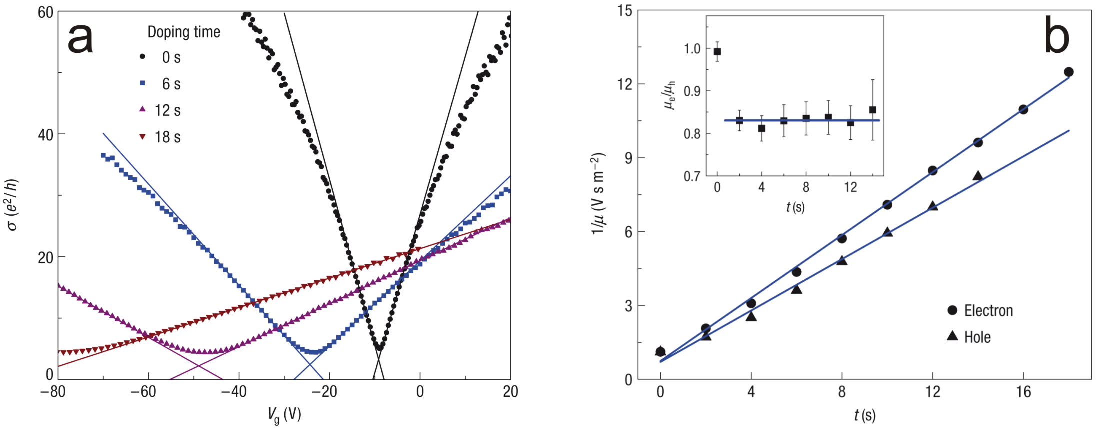

**Figure 2.6:** Charged impurity scattering in potassium doped graphene. **(a)** The conductivity $\sigma$ as a function of gate voltage $V_g$ for pristine graphene and three different doping concentrations taken at 20 K in UHV. The lines are fits according to equation 2.20 and their crossing defines the points of residual conductivity and the gate voltage at minimum conductivity. **(b)** Inverse of electron mobility $1/\mu_e$ and hole mobility $1/\mu_h$ as function of doping time. Inset: Ratio of $\mu_e$ to $\mu_h$ versus doping time. Fig. from [43].

authors found an inverse dependence of the carrier mobility on the density of charged impurities for electrons and holes.

### 2.5.3 Short-range scattering

Another source of perturbation in graphene are short-range defects such as vacancies, cracks, step edges and any other topographic defects [51]. Stauber *et al.* proposed an additional scattering mechanism involving midgap states, which is introduced by these defects. Vacancies lead to a similar $k$ dependence of the relaxation time as charged impurities and the conductivity is roughly linear in $n_s$ [22, 52]:

$$\sigma_d = \frac{2e^2}{\pi h}\frac{n_s}{n_d}\ln^2(\sqrt{\pi n_s}R), \tag{2.21}$$

where $n_d$ is the defect density and $R$ is the radius of the defect in this model. This formula is in close analogy to the equation derived for Coulomb scattering (equation 2.20), with an additional logarithmic dependence on $n_s$. The almost linear relation between conductivity and carrier density and the inverse scaling of mobility with defect density could be proved in experiments in graphene on $SiO_2$ [44].

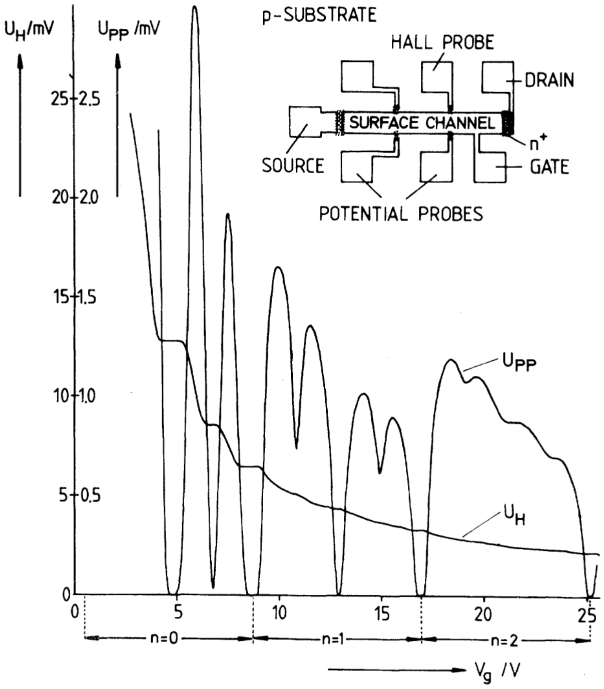

**Figure 2.7:** Original QHE experiment in the inversion layer of a MOSFET: The graph shows the Hall voltage $U_H$ and the voltage drop between the potential probes $U_{PP}$ as a function of gate voltage $V_g$ at $T = 1.5$ K and $B = 18$ T. Fig. from [54].

## 2.6 Introduction to Quantum Hall effect

More than 130 years ago, Edwin Hall interpreted the influence of a magnetic field on a conducting material [53]. The classical Hall effect describes the creation of a potential difference across a conductor, transverse to an electric current, in the presence of a magnetic field. Using this effect, it is possible to determine the density and the sign of of the charge carriers in a bulk material.

Almost exactly 100 years later, Klitzing *et al.* observed a quantization of the Hall resistance in 2DEG systems [54]. Since its discovery, the so called Quantum Hall effect (QHE) has created great interest in the experimental study of the properties of low-dimensional systems [22]. In their experiments at low temperatures and high magnetic fields, Klitzing and coworkers found a quantization of the Hall resistivity $\rho_{xy}$, corresponding to the value $h/Ne^2$ (with $N$ being an integer), and a simultaneous modulation of the longitudinal resistivity $\rho_{xx}$ as a function of the the carrier density (see Fig. 2.7). The oscillations of the longitudinal resistance, the so called Shubnikov-de Haas oscillations (SdHOs), were analyzed precisely and $\rho_{xx}$ was going down to zero over the range of each plateau of the quantized Hall resistance. The plateaus can be assigned to integer filling factors $\nu = n_s h/eB$, where $n_s$ is the sheet carrier density [55].

The quantization and oscillation of $\rho_{xy}$ and $\rho_{xx}$, respectively, is universal to all 2D electron systems. In the following part, I want to introduce the integer QHE in conventional 2DEGs and discuss the formation of Landau levels (LLs), the existence of edge states and the role of disorder. For a 2DEG sample with

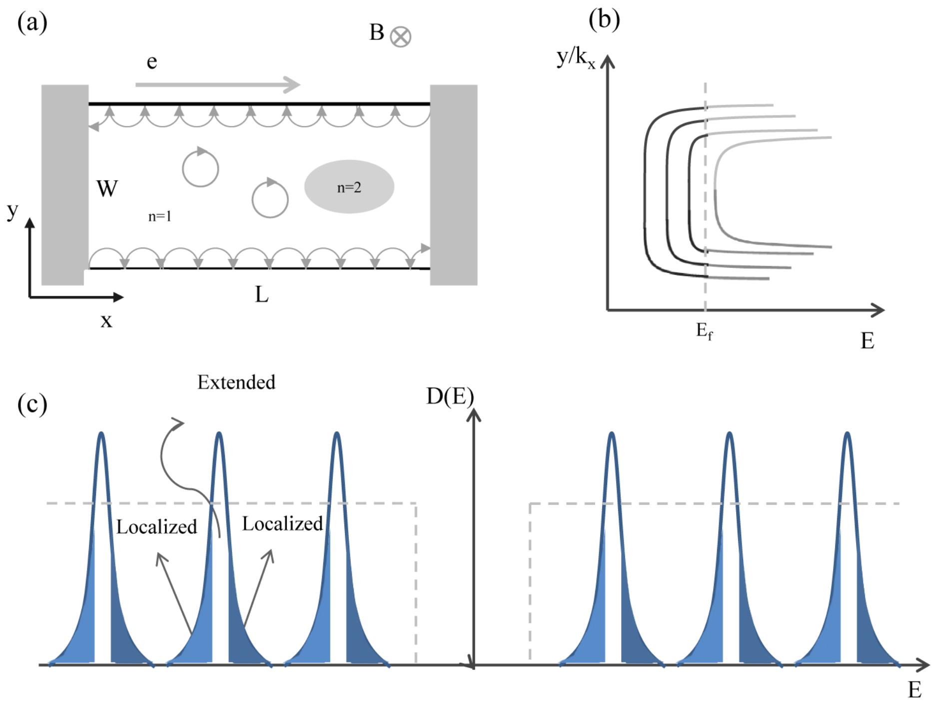

**Figure 2.8:** Schematics of edge states and broadening of LLs in the QHE: **(a)** A finite 2DEG under a perpendicular magnetic field B. A large area is quantized at n =1 while, due to potential difference, a small n = 2 LL is formed in the middle of the sample. Grey circles with arrows indicate the cyclotron motion. **(b)** Formation of edge channels in the LLs. (c) Density of states with broadened LLs. Fig. from [55].

finite dimensions, exposed to a magnetic field $B$ (see Fig. 2.8a), we can approach the energy spectrum and the quantization of the LLs by solving the Schrödinger equation of a single particle [56]:

$$\left[\frac{1}{2m}(\vec{p}+e\vec{A}(\vec{r}))^2+V(z)\right]\Psi(\vec{r})=E\Psi(\vec{r}), \tag{2.22}$$

where $\vec{A}$ is the vector potential of the magnetic field $\vec{B}$ and $V(z)$ is the quantized potential along the $\hat{z}$-direction. The solution of the Schrödinger equation gives the quantized, equidistant Landau levels:

$$E_n=\hbar\omega_c(n+\frac{1}{2}) \qquad \text{with} \quad n=0,1,2,3,..., \tag{2.23}$$

where $\omega_c$ is the cyclotron frequency of the electrons. For the integer Quantum Hall effect, the transverse conductivity can be written as:

$$\sigma_{xy}=\nu\frac{e^2}{h}=fn\frac{e^2}{h}, \tag{2.24}$$

where $n$ is the number of filled LLs and $f = 2$ is the spin degeneracy in the 2DEG system.

The quantized Hall resistance and the SdHOs can be explained with 1D conducting edge channels, originating from the LL bending. Fig 2.8b shows the LLs and the formation of channels along the edges of the sample. Considering the edge boundary condition $\Psi(x = 0, W) = 0$ and the approximately parabolic band structure of the band edges in momentum space, the energy of the LLs increases as they approach the edges [55]. The only states that carry the current are the edge states at the Fermi level $E_F$. Filling factor $\nu = N$ implies, there are $N$ conducting edge states, coinciding with a quantized Hall resistance $\rho_{xy} = h/Ne^2$ [57]. The currents on each edge are running in opposite directions, due to the cyclotron motion in the perpendicular magnetic field. Thus, the only source of backscattering would be electrons going from one edge to the other. In this way, the onset of interaction between the two sets of edge states leads to deviations from exact quantization and eventually to a breakdown of the quantum Hall regime [57]. Otherwise, the suppression of backscattering in the QHE regime leads to a vanishing $\rho_{xx}$ and induces dissipationless transport.

Nevertheless, the model of conducting edge channels does not explain the Fermi level pinning between the LLs. Here, we need to consider vacancies and impurities that cause the broadening of the density of states (DOS) and the formation of localized states at its slopes (see Fig. 2.8c). The charge carriers cannot scatter into the localized states and the Fermi energy gets pinned, resulting in the experimental observation of QHE plateaus with finite width [22].

### 2.6.1 Quantum Hall effect in graphene

Since graphene is a 2D material, one of the first and most important experimental results was the observation of the quantum Hall effect (see Fig. 2.9) [2, 27]. Considering its unique properties regarding lattice and band structure, the quantum Hall effect in graphene is significantly different than in conventional 2DEG structures. Graphene's sublattice symmetry adds an additional degree of freedom, so the charge carriers have a fourfold degeneracy (two spin, two pseudospin). Thus, the resulting energies of the LLs are no longer equidistant, but have a square root dependence on the magnetic field $B$:

$$E_n = \pm\sqrt{2e\hbar v_F^2\,|n|\,B} \qquad \text{with} \quad |n| = 0, 1, 2, 3, ... \tag{2.25}$$

Here, $n > 0$ and $n < 0$ are for electron-like and hole-like Landau levels, respectively. This energy spectrum results in an unconventional, half-integer sequence of energy levels with the presence of a distinctive LL at $E_n = 0$ [58, 59]. The $n = 0$ LL is formed with degenerate electron and hole states, leading to a half-integer shift in the number of flux quanta needed to fill an integer number of LLs (see Fig. 2.9) [55].

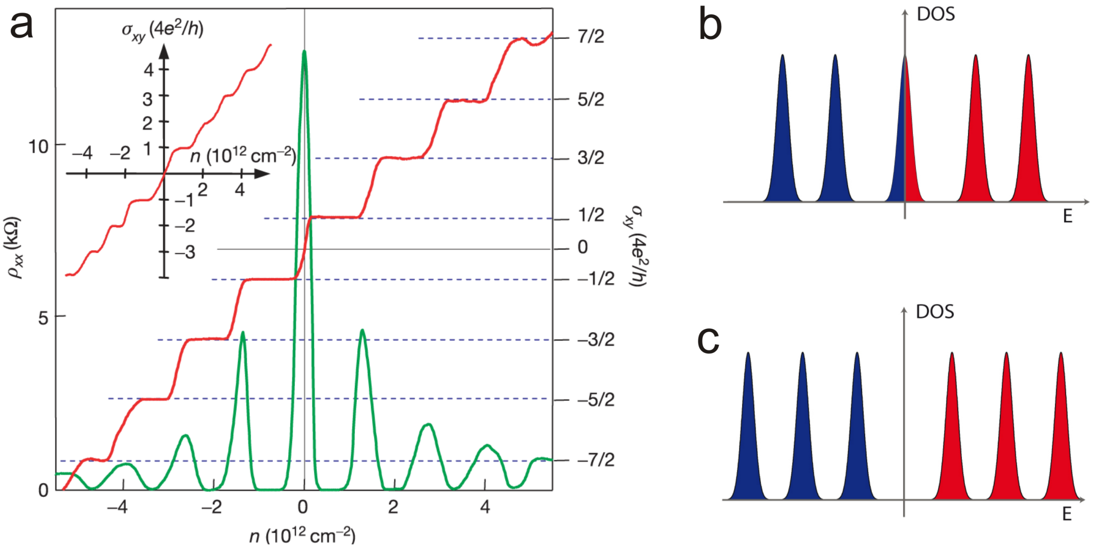

**Figure 2.9:** Quantum Hall effect and density of states in graphene. **(a)** Hall conductivity $\sigma_{xy}$ and longitudinal resistivity $\rho_{xx}$ as a function of carrier density $n$ at $B = 14$ T and $T = 4$ K in monolayer graphene. The minima of the SdHOs follow the half-integer plateaus in $\sigma_{xy}$. **(b)** DOS of graphene with the zero-energy LL and **(c)** DOS of a conventional 2DEG with equidistant LLs. Fig. from [2].

As a consequence of the half-integer quantization of the energy levels, the quantum Hall conductivity is shifted with respect to the standard QHE sequence by 1/2 and reads as follows:

$$\sigma_{xy} = \nu \frac{e^2}{h} = \frac{4e^2}{h}(n + 1/2). \tag{2.26}$$

Since the energy difference between the first and the second LL $\Delta E = \sqrt{2e\hbar v_F^2 B} \approx$ 200 meV (at $B = 30$ T) is significantly higher than the thermal energy at room temperature, the quantum Hall effect in graphene can even be observed at high temperatures (and high magnetic fields) [60].

### 2.6.2 Quantum Hall ferromagnetism in graphene

Two different kinds of massless Dirac particles, centered on the two inequivalent valleys, can be described in a low-energy effective theory of graphene. In high magnetic fields, the valley and electron spin degeneracy lead to the anomalous graphene quantum Hall sequence (Equation 2.17). Many different broken symmetry states can appear in electronic systems with multiple degenerate degrees of freedom [61]. Strong Coulomb interactions and a fourfold spin-valley degeneracy cause a SU(4) isospin symmetry in graphene Landau levels [62, 6]. At partial filling of these LLs, exchange interactions can break this symmetry and polarize

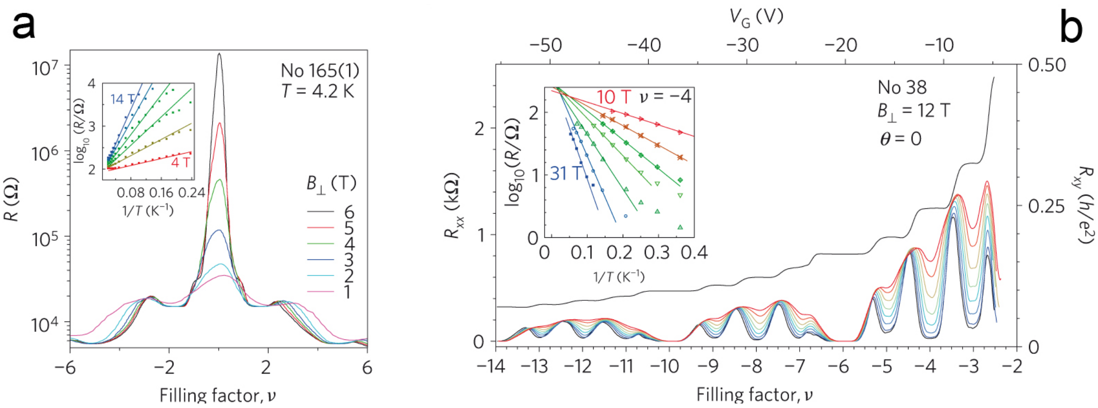

**Figure 2.10:** Symmetry broken integer quantum Hall effect in graphene. **(a)** Development of the $\nu = 0$ insulating state. Inset: Arrhenius plot for $\nu = 0$ as a function of $B$. **(b)** Temperature dependence of $R_{xx}$ minima and plateaus in $R_{xy}$ of symmetry broken IQHE. Inset: Arrhenius plot for $\nu = 4$ as function of $B$. Fig. adapted from [6].

the ground state ferromagnetically. This fact is manifesting as additional quantum Hall plateaus beside the normal integer sequence in high-quality graphene samples (see Fig. 2.10b) [6, 63, 7].

The SU(4) polarization of graphene is influenced by the interplay between anisotropies arising from the Zeeman effect, disorder, and lattice scale interactions. The large activation gaps confirm the Coulomb origin of all broken symmetry states, but the order strongly depends on the LL index [6]. Different groups observed the ferromagnetic polarization of the QHE in graphene [63, 64, 65, 66], featuring broken symmetry states beside the normal sequence, but there was an ongoing controversial debate about its origin [61, 67, 68].

In order to explore the origin of the lifted degeneracy, Young *et al.* performed magnetotransport measurements on graphene-hBN heterostructures in tilted magnetic fields [6]. Since graphene is a monolayer, the in-plane magnetic field can only couple to the electron spin of the system. By changing the tilt angle, they could examine the variation of the energy gaps of different quantum Hall states as a function of the in-plane magnetic field. The perpendicular magnetic field remained constant during these measurements. In this way, they were able to explore the spin structure of the broken symmetry states.

One essential result is the different influence of exchange interactions on the $n = 0$ and the $n > 0$ LLs . Large activation gaps prove the Coulomb origin of all broken symmetry states, but the order depends critically on the Landau level index [6, 69]. The zero energy LL is half-filled at $\nu = 0$ and an isolating state is emerging at higher fields (Fig. 2.10a) [9, 70]. The resistance of this state decreases with increasing in-plane magnetic field, indicating broken valley symmetry. On the contrary, the energy gap of half-filled higher LLs (e.g.

$\nu = 4, 8, 12, ...$) is increasing with in-plane field, suggesting a spin polarization of the ground state. Further measurements reveal a spin polarization of $\nu = 1$ and a valley polarization of higher quarter filled LLs ($\nu = 3, 5, 7, ...$). The origin of this behavior is not really understood, yet. One possible reason for the difference between $n = 0$ and $n > 0$ LLs could be the different influence of the magnetic field on the symmetry breaking effects: The Zeeman energy scales proportionally with B, but the Coulomb interactions scale with $\sqrt{B}$ [69].

Due to the 2D confinement of electrons in graphene, many-body interactions between electrons are expected to be strongly enhanced. Sufficient electron-electron interaction in the SU(4) isospin symmetry can manifest in fractional quantum Hall states in high-quality graphene [71, 72], where additional Hall plateaus with rational filling factors $\nu$ appear. Fractional quantum Hall states can be considered as realization of the IQHE for weakly interacting quasiparticles, named composite fermions [22, 73]. The huge improvements in sample quality, employing suspended graphene or graphene-hBN heterostructures, gave the possibility to observe the fractional quantum Hall effect in graphene devices [8, 9, 74, 65].

## 2.7 *pn*-junctions in graphene

Graphene can be tuned between the hole ($p-$) and electron ($n-$) regime by using the electric field effect. So regions with different potential $V$ can be achieved by locally gating the graphene sheet. Thus, *pn*-junctions in graphene are created artificially with local gates, imposing a negative and positive potential (with respect to the Dirac point) to two regions next to each other. Additionally, *pn*-transitions play an important role in the low-density regime, where transport properties are dominated by electron-hole puddles [75]. Considering electron optics, where the charge carriers can be guided and lensed analogous to light rays across an optical boundary, the negative refraction and the angular dependence of transmission in a *pn*-junction are equally important [76, 77]. These mechanisms and their influence on transport experiments will be discussed by introducing Snell's refraction law and Klein tunneling in graphene.

### 2.7.1 Snell's law in graphene

Ballistic electrons in graphene behave in close analogy to light. When transmitted across a boundary, located between two separate regions of different potential, charge carriers get refracted, similar to light rays crossing a boundary between two materials of different optical index [76]. In this way, mirrors, lenses, splitters, and other optical manipulators can be realized in graphene.

In graphene devices, where the parallel momentum at an interface needs to be conserved, the Fermi level is responsible for the refractive index. Snell's law for refraction in graphene structures can be written as:

$$E_l \cdot \sin(\theta_l) = E_r \cdot \sin(\theta_r) \tag{2.27}$$

Here, $E_l$ and $E_r$ are the Fermi energies on the left and on the right side, respectively, and $\theta_l$, $\theta_r$ are the corresponding refraction angles. Snell's law is depicted in Fig. 2.11 for incident electrons on an unipolar ($nn'$-) and a bipolar ($np$-) junction. The former is shown in Fig. 2.11a, where the Fermi level on the left side in higher than the right one. This discrepancy in Fermi energy causes a different $k$-circle at the Fermi level for the right and the left area. Considering the conservation of the parallel momentum $k_y$ at the interface, this situation will lead to a refraction towards the junction.

The latter situation, where a electron runs into a *pn*-junction, is illustrated in Fig. 2.11b. Since the momentum $k_y$ needs to be conserved, the angle of back-reflection is $\theta_l' = \theta_l$. However, the situation for the transmitted electron is slightly different. This electron needs a positive group velocity $\vec{v}$ in x-direction, and since $\vec{v}$ is anti-parallel to $\vec{k}$, $k_{x,l} = -k_{x,r}$ for a symmetric *pn*-junction [77].

The negative refraction index in graphene *pn*-junctions, defined by equation 2.27, is the basic principle for Veselago lenses. There, charge carriers can be focused from a point-like injector to a point-like detector, employing a *pn*-interface for lensing (see Fig. 2.11c) [78, 79]. In order to transmit and focus trajectories with large angles of incidence, these lenses need sharp and symmetric *pn*-interfaces. Figure 2.11d shows the electron trajectories for an asymmetric case, where $|n_l| < |p_r|$. In this situation the focus point is blurry and forms a caustic pattern [77].

### 2.7.2 Chiral Klein tunneling in graphene

The Klein paradox, proposed by Oskar Klein in 1929 [80], describes a tunneling process of relativistic particles penetrating a potential barrier if its height $V_0$ exceeds the electron's rest energy $mc^2$ [81]. This tunneling mechanism is in stark contrast to conventional quantum mechanics for non-relativistic particles, where the tunneling probability depends on the barrier height $V_0$. The Klein paradox refers to perfect tunneling of normally incident relativistic particles through a sharp potential barrier of sufficient height. But it is also true for a gradually changing potential $V(x)$, where the change in potential occurs on a smaller length scale $d$ than the Compton wavelength $\lambda_c = h/mc$ [82].

For many years, the Klein paradox has only been relevant in very special situations, such as positron production around super-heavy nuclei or evaporation of black holes [83]. This changed with the discovery of graphene, where Klein tunneling could be studied experimentally [41, 84, 85]. The charge carriers in

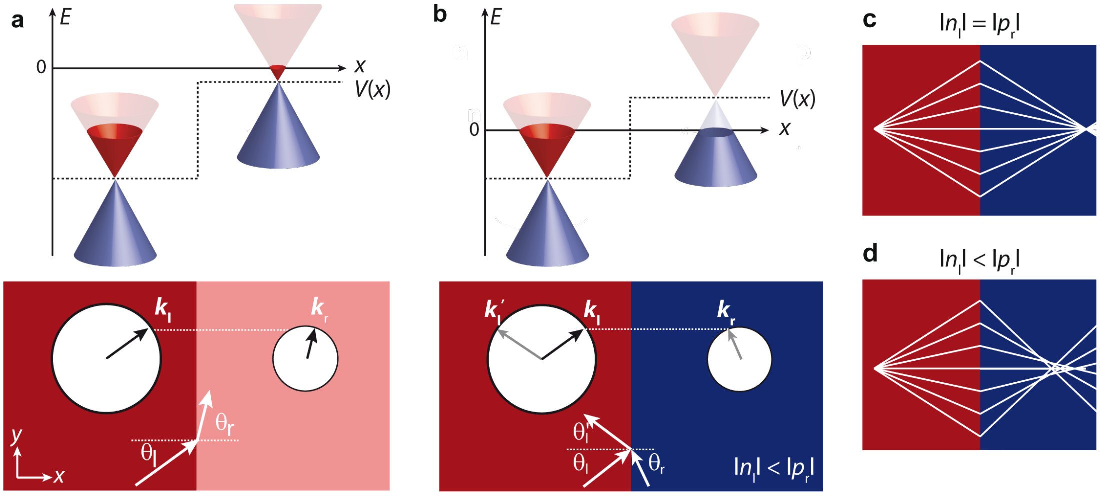

**Figure 2.11:** Illustration of Snell's law in graphene. **(a)** Snell's law for a unipolar $nn'$-junction with angle of incidence $\theta_l$ and transmission angle $\theta_r$. **(b)** $pn$-interface, where the incident electron gets reflected under $\theta_l$' or transmitted under $\theta_r$. **(c)** Considering the negative refraction index at the $pn$-interface, electrons can get focused from one point to another with a straight lens (Veselago lens). **(d)** The focal points becomes blurry for asymmetric doping. Fig. from [77].

graphene act as relativistic, massless Dirac fermions, and graphene's gapless dispersion relation allows to observe the Klein paradox. A sufficiently high potential barrier can be easily created by electrostatic gating, forming regions of electron ($n$) and hole doping ($p$) next to each other [86].

Klein tunneling in graphene can be explained with the absence of backscattering due to the conservation of chirality and can be experimentally realized with a rectangular shaped $npn$-junction, as shown in Fig. 2.12a. For normally incident electrons with $\vec{k} = \vec{k}_x$, backscattering is forbidden due to pseudo-spin conservation [87]. Additionally, the parallel momentum $k_y$ needs to be preserved, because of the symmetry of the potential barrier. As a consequence, there is perfect transmission for normally incident carriers ($\theta = 0$) [77, 81]:

$$|t(\theta = 0)|^2 = 1. \tag{2.28}$$

During the tunneling process, chirality is conserved since the pseudospin is parallel to $\vec{k}$ in the conduction band and anti-parallel in the valence band. In this picture, an incident electron in the conduction band with momentum $\vec{k}_x$ and energy $E$ tunnels into the valence band with momentum $-\vec{k}_x$ and energy $-E$ inside the barrier. Due to chirality, the group velocity stays the same during the interband transition and the incident electron is perfectly transmitted. So Klein tunneling is not a genuine quantum tunneling effect as it does not necessarily rely on evanescent waves [87].

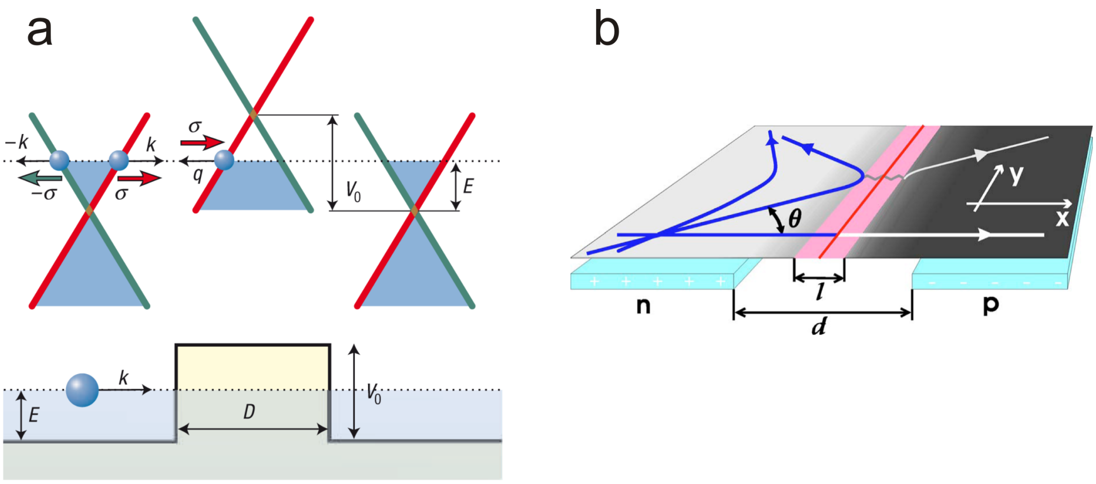

**Figure 2.12:** Tunneling through a potential barrier in graphene. **(a)** Sketch of the spectrum of quasiparticles in monolayer graphene. The bottom picture shows a incident electron with momentum $\vec{k}$ and energy $E$ on a potential barrier with width $D$ and height $V_0$. The upper one depicts the corresponding spectrum of the quasiparticles. The blue areas are occupied states within the linear spectrum, and the red and green lines emphasize the pseudospin $\vec{\sigma}$. **(b)** Angular dependence of the transmission in a smooth *pn*-junction. $d$ is the length scale of the potential variation and $l$ the turning point at the interface. Fig. from [83, 88].

In the following part, the angular dependence of the transmission probability $t$ at a symmetric and rectangular *pn*-junction will be discussed. For the situation of oblique incidence of carriers on the potential barrier, backscattering is no longer forbidden and $t$ decreases. The angular dependence of $t$ can be obtained by matching the real-space wavefunctions on both sides of the *pn*-junction and can be written as [88]:

$$|t(\theta)| = \cos^2(\theta). \tag{2.29}$$

This simple relation gives a 50% transmission and reflection probability for $\theta = 45°$.

In real devices, the assumption of perfectly sharp and rectangular interfaces is not valid. They vary gradually from $p$- to $n$-type on a length scale $d$ [88]. Here, the junction is considered smooth if $k_F d \gg 1$. A rather simple potential profile for a smooth and symmetric *pn*-junction is:

$$V(x) = \begin{cases} -V/2 & , \quad x < 0 \\ Fx & , \quad 0 \leq x \leq d \\ V/2 & , \quad x > d \end{cases} , \tag{2.30}$$

where $\pm V/2$ is the Fermi potential in the outer areas and $F = V/d = \hbar v_F/d$ is the electric field created by the changing potential [77]. Now the transmission probability shows an exponential decay for $\theta \neq 0$ (and $\theta$ not too close at $\pi/2$)

[88]:

$$|t(\theta)| = e^{-\pi(k_F d)\cdot\sin^2(\theta)} \tag{2.31}$$

By deriving the results in equations 2.29 and 2.31, we can determine the conductance per unit length of a broad and smooth junction, where only carriers, approaching within a small angle $\theta \leq \theta_0 = (\pi k_F d)^{-1/2}$, are selectively transmitted [88]:

$$\sigma_{pn} \approx \frac{2e^2}{\pi h}\sqrt{\frac{k_F}{d}}. \tag{2.32}$$

The exponential decay of $t$ as a function of $\theta$ in equation 2.31 can be understood with the decline of the potential in the immediate vicinity of the $pn$-junction, at the turning point $l = v_F p_y / F$ (see Fig. 2.12b). There, the trajectories entering the smooth region of the potential, are gradually diverting from the interface due to the additional electric field $F$. This situation is quite similar to the exponential decay of $t$ for massive relativistic particles described by Sauter [82], where the only difference would be the replacement: $v_F \to c, \lambda_F \to \lambda_c$, and $\sin(\theta) \to m$. Nevertheless, this gradually smooth and symmetric model is not realistic for a potential induced by electrostatic gating. In this case, a non-linear potential profile would be created, and therefore, the modeling of the transmission probability needs a more elaborate simulation technique, such as tight-binding theory [89].

### 2.7.3 *pn*-junctions in a magnetic field

The presence of a magnetic field substantially changes the electronic transport properties of a conductor. Lorentz forces are acting on the charge carriers, bending their trajectories and constraining them onto cyclotron orbits in a quasi-classical picture. At moderate magnetic fields charge carriers are not localized at the boundaries of the conducting channel and can propagate via so-called skipping orbits [77]. This effect also influences the propagation of electrons encountering $pn$-interfaces in the presence of magnetic fields. It was predicted that a relatively small magnetic field will suppress the conductance of a $pnp$-junction below the series conductance of the individual interfaces by bending the trajectories away from normal incidence [88, 91]. This mechanism, induced by the angular dependence of the transmission, can be seen in Fig. 2.13a, where the left trajectory is transmitted for zero magnetic field and the right one is reflected in a small magnetic field.

Rickhaus *et al.* describe the evolution of electron states in a graphene $pn$-junction for increasing perpendicular magnetic fields with the sketches depicted in Fig. 2.13b-e [90]. At low magnetic fields (Fig. 2.13b) transport is dominated by Fabry-Pérot oscillations with slightly bent trajectories [41]. The cyclotron orbits

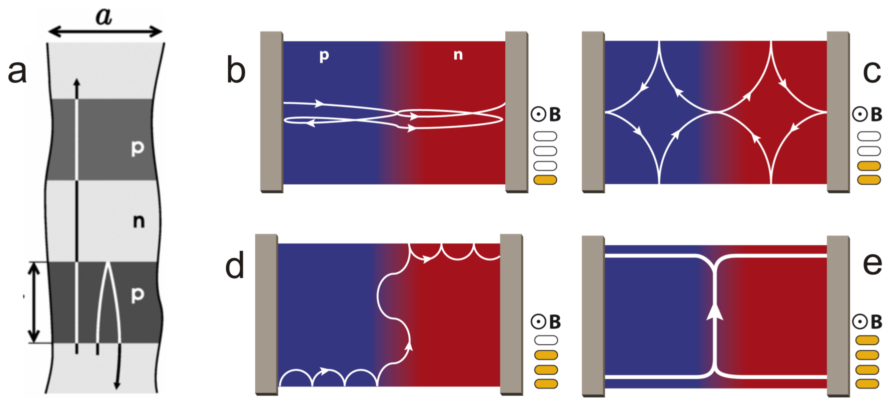

**Figure 2.13:** *pn*-junctions in the presence of a magnetic field. **(a)** Electron trajectories in a *pnp*-junction: the left one (transmitted) in zero $B$ and the right one (reflected) in small non-zero $B$. **(b)** Two-terminal graphene device with $p$- and $n$-region. By applying a weak field, the electron trajectories are bent, manifesting in Fabry-Pérot oscillations. **(c)** The field is increased until the cyclotron orbit becomes comparable to the cavity size, where resonant scar states can occur. **(d)** The field is further increased and transport is described by quasi-classical cyclotron orbits forming snake states along the interface. **(e)** Finally, quantum Hall edge states propagate in opposite direction in the $p$- and $n$-region at higher $B$. Figures adapted from [88, 90].

are increasing with magnetic field until the cyclotron orbits become comparable to the cavity size. Here, resonant scar states (Fig. 2.13c) may occur [92]. At higher fields snake states, propagating along the *pn*-interface, are governing the transport properties (Fig. 2.13d) [90], and finally counter-propagating quantum Hall edge states in the $p$- and $n$-region are formed (Fig. 2.13e).

Shytov *et al.* report calculations for a single *pn*-junction, where they claim a strong dependence of quantum transport on the magnitude of the magnetic field [93]. The angle of perfect transmission is shifted to a non-zero angle $\theta_{max} = \arcsin(B/B_*)$ in the presence of a moderate magnetic field (see Fig. 2.14), and the transmission $T(\theta)$ can be written as:

$$T(\theta) = e^{-\alpha\gamma^3(\sin\theta - B/B_*)^2}, \tag{2.33}$$

where $\alpha = \pi(d/\lambda_F)^2$ and $\gamma = 1/\sqrt{1-\beta}$ with boost parameter $\beta = -v_F B/cE = -B/B_*$. At the critical field

$$B_* = (c/v_F)E \approx \frac{\hbar}{e}\frac{k_F}{d} \tag{2.34}$$

the cyclotron radius $R_C = \hbar k_F/eB$ becomes comparable to the width of the interface $d$. When the magnetic field exceeds a critical value of $B > B_*$, the junction is pinched off by the Landau level formation and no transmission is

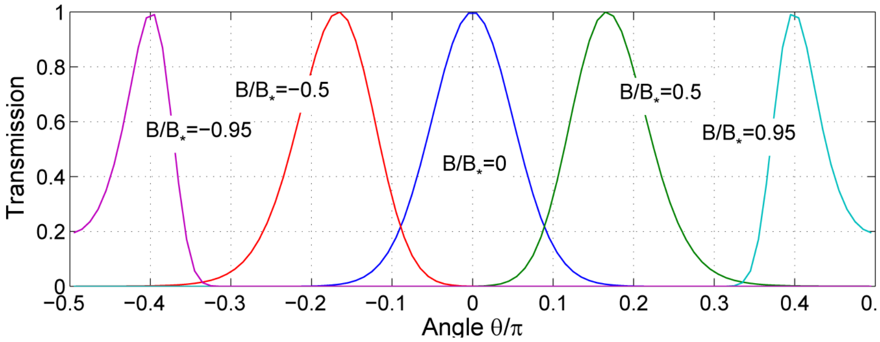

**Figure 2.14:** Angular dependence of transmission for different magnetic field values, plotted according to Eq. 2.33, for $\alpha = \pi(d/\lambda_F)^2 = 20$. Transmission reaches unity at a field-dependent angle $\theta_B = \arcsin B/B_*$. Fig. adapted from [93].

possible through the *pn*-interface. In this case charge carriers propagate parallel to the interface [91, 94].

# CHAPTER 3

# Graphene-boron nitride heterostructures

The characteristics of graphene devices are significantly influenced by the underlying substrate. Standard $SiO_2$ substrates are highly disordered and strongly decreasing graphene's quality by scattering from charged surface states and impurities, substrate roughness and surface phonons [43, 50, 7]. Additionally, the substrate-induced disorder forms electron-hole pairs in the vicinity of the charge neutrality point [34, 75].

One approach to avoid these limitations is removing the substrate and suspending the graphene layer. While the quality of suspended graphene is substantially increased and carrier mobilities are more than one order of magnitude higher than on $SiO_2$ [95], the absence of a supporting substrate imposes serious restrictions in functionality and device architecture [35]. Therefore, there was an extensive search for other, more suitable substrates that retained the functionality of $SiO_2$ and the quality of a suspended device. One appealing substrate that came up was hexagonal boron nitride (hBN), an insulating isomorph of graphene, and since 2010, hBN-graphene heterostructures have triggered a new field for high-quality graphene research. This chapter focuses on the properties of hBN and the advantages of hBN-graphene heterostructures, fabricated with a dry-transfer method. I will discuss the influence of the supporting hBN layer and the effect of potentially arising superlattice structures.

## 3.1 Hexagonal boron nitride

Hexagonal boron nitride is an interesting insulating isomorph of graphite with boron and nitrogen atoms occupying the A and B sublattices. Thus, hBN has a crystalline, layered structure and an atomically flat surface. Similar to graphene,

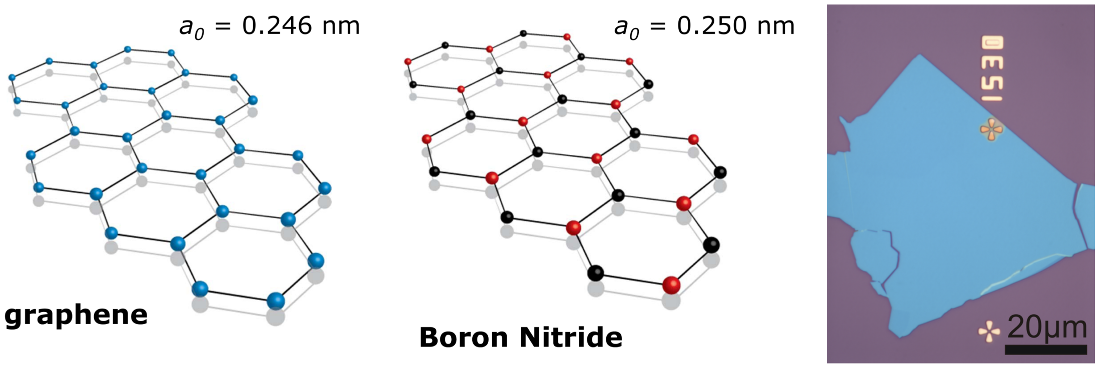

**Figure 3.1:** Lattice structure of graphene and hBN and a optical micrograph of an exfoliated hBN flake. The structure of both crystals is very similar, forming a planar, hexagonal lattice. Instead by carbon atoms for graphene, hBN is build up by boron and nitrogen atoms (red and black). The lattice mismatch of graphene and hBN is only 1.7 %. The right picture shows an exfoliated hBN crystal on a Si/$SiO_2$ wafer. Fig. on the left from [101].

the atoms in each layer are covalently bound, but the different layers are held together by van der Waals forces. Due to weak interlayer van der Waals forces, hBN can be exfoliated in the same way as graphene and we can get few tens of micrometer large flakes with a thickness down to monolayers. Resulting from the different onsite energies of the boron and nitride atoms, hBN has a large band gap (5.97 eV) and a small lattice mismatch (1.7 %) with graphene [7, 96]. The lattice structure of hBN, compared to graphene, and an exfoliated hBN crystal are illustrated in Fig. 3.1. Because of its strong in-plane bonding in the hexagonal lattice structure, hBN is relatively inert and the smooth surface is free of dangling bonds and charge traps [97].

The insulating behavior of hBN is providing great potential for an application as substrate, encapsulating layer, dielectric buffer layer, or tunneling barrier [35, 98, 99, 100]. Here, the dielectric properties of hBN ($\epsilon \approx 3, V_{breakdown} \approx 0.7$ V/nm) excel those of $SiO_2$, making hBN a favorable gate dielectric. Additionally, surface optical phonon modes in hBN have energies two times larger than similar modes in $SiO_2$, paving the way for improved high-temperature and high-electric field performance of hBN-graphene heterostructures [7].

## 3.2 Advantages of hBN-graphene stacks

The atomically flat surface of hBN is probably its greatest advantage over thermally grown and amorphous $SiO_2$ substrates. Since graphene tends to conform to its substrate, ripples and surface roughness are strongly influenced by the supporting substrates. Due to the atomically smooth surface of hBN crystals, hBN-graphene heterostructures are expected to have a significantly reduced sur-

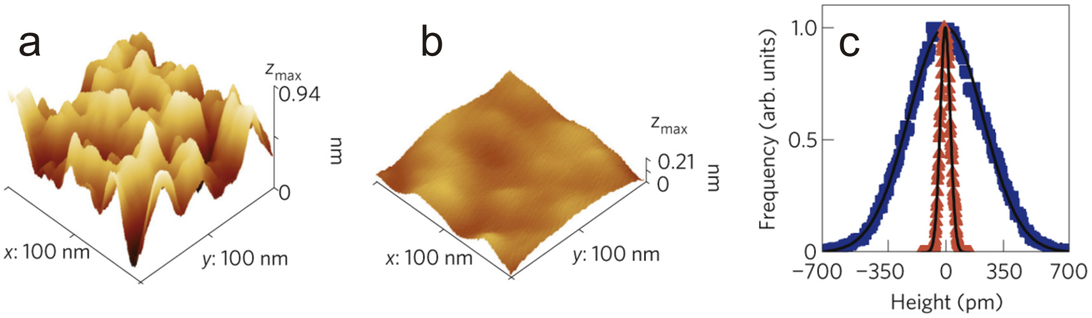

**Figure 3.2:** Topography comparison of graphene on hBN and $SiO_2$. **(a)** STM topographics image of graphene on $SiO_2$ showing pronounced surface corrugations. **(b)** STM topographics image of graphene on hBN showing significantly reduced corrugations. **(c)** Histogram of height distributions for graphene on hBN (red) and graphene on $SiO_2$ (blue) along with Gaussian fits. Fig. from [97].

face roughness compared to graphene devices on $SiO_2$. This can be clearly seen in experiments by Xue *et al.*, where the authors conducted STM topography measurements of graphene on hBN and compared the results to graphene on $SiO_2$ (see Fig. 3.2) [97]. There is a striking difference between the obtained histograms resulting from the supporting substrates. Both curves are well fit by a Gaussian distribution, yielding standard deviations of 225 pm for $SiO_2$ and 30 pm for hBN. Since the roughness of graphene on hBN is similar to graphene on HOPG (**H**ighly **O**riented **P**yrolytic **G**raphite), we can expect it to be at the ultimate limit of flatness [69]. The increased flatness leads to a suppression of rippling and thus to a reduction of electron-hole puddles in graphene. Local spectroscopy measurements demonstrated that, employing hBN substrates, the electron-hole charge fluctuations can be reduced by two orders of magnitude compared to standard $SiO_2$. Hence, the charge fluctuations are as small as in suspended devices, giving the opportunity to examine very low densities in the vicinity of the charge neutrality point without the challenges and limitations of a freestanding flake [97].

Another interesting experimental observation is the perfect local stacking of graphene and hBN (see Fig. 3.3a,b) [102]. Obviously hBN-graphene heterostructures often exhibit different kinds of bubbles and wrinkles, originating from trapped residues between the layers. Nevertheless, there are large areas where the different layers of the stack are free of contaminants and lying perfectly on top of each other. Figure 3.3c shows an AFM amplitude error image of one of our heterostructures, exhibiting several bubbles and wrinkles, as well as plain areas of perfect stacking. The reason for such behavior is the so-called “self-cleansing” mechanism, where the residues between the layers are pushed away and congregating in separate pockets. This effect can be understood in terms of energy, where the energetically favorable situation is when the two crystals have the largest possible common interface [103, 104].

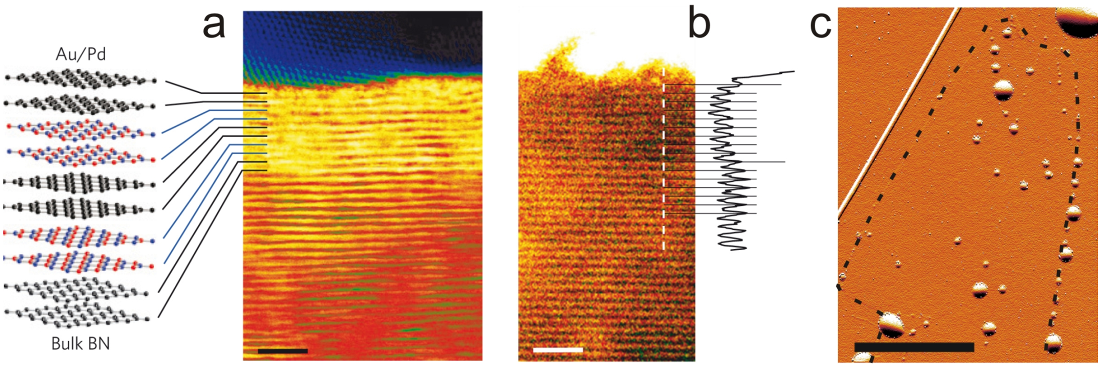

**Figure 3.3:** STEM image of a hBN-graphene heterostructure consisting of several bilayers. **(a)** Bright-field cross sectional STEM of the stack with the specific layer sequence shown on the left. **(b)** HAADF STEM image of the same structure, showing the perfect stacking of the layers with no residues or adsorbates in between. **(c)** AFM amplitude error image of an encapsulated graphene device with several bubbles and wrinkles. The dashed black line encircles the graphene flake and scale bar is 5 $\mu$m. Fig. a,b adapted from [102].

For the fabrication of these heterostructures, hBN and graphene are stacked and put on a Si/SiO$_2$ wafer. Similar to graphene on SiO$_2$, the charge carrier density can be tuned by varying the voltage applied to the highly-doped Si back gate. Since there is an additional dielectric material between graphene and the back gate, we also need to take into account the hBN flake. As a simple approach, the capacitive gate coupling can be considered as two serial plate capacitors:

$$C_g = \left( \frac{d_{SiO_2}}{\epsilon_0 \epsilon_{SiO_2}} + \frac{d_{hBN}}{\epsilon_0 \epsilon_{hBN}} \right)^{-1}, \tag{3.1}$$

where the corresponding dielectric constants for SiO$_2$ and hBN are $\epsilon_{SiO_2} \approx 3.9$ and $\epsilon_{hBN} \approx 3$. Using this equation, one can estimate the carrier density induced by the global back gate. Obviously the formula can be modified for top gate or bottom gate structures, separated from graphene by hBN flakes. But it can be only a first approximation for the induced carrier density, and more advanced gate geometries need more elaborate simulation techniques.

Another important improvement in sample quality came with the encapsulation of graphene between two layers of hBN. Although there were some device geometries with encapsulated graphene [99, 100], one drawback was the requirement to transfer and pattern each crystal separately in order to contact the sandwiched graphene. So for example we needed to start with a suitable hBN flake and transfer graphene on top of it. Subsequently, we etched graphene in Hall bar shape and deposited metallic contacts. In a last step, another hBN flake was put on the stack and the encapsulated graphene heterostructure was finished. Of course, the different processing steps left a significant amount of fabrication residues on graphene and between each layer of the vertical heterostructure, leading to a strongly reduced device quality.

This problem could be solved by Wang *et al.*, who introduced a new sample design, employing a dry transfer technique and 1D edge contacts to graphene [98]. Thus, the stack could be assembled right away, and after that, further fabrication steps such as etching Hall bars and evaporating contacts were carried out. In that way, graphene is protected from any environmental influences such as fabrication residues and other adsorbates. With this, mobilities can be considerably increased with encapsulated graphene, exceeding a million $\mathrm{cm}^2/\mathrm{Vs}$ in the best samples [105]. These numbers are in the same order of magnitude as for suspended graphene, with the advantages of heterostructures discussed before.

Recently, 2D materials and their novel van der Waals heterostructures got more and more attention and a huge amount of research focused on them. Besides graphene and hBN, there is a growing zoo of new 2D materials, covering a very broad range of properties [103, 106]. Combining them opens an exciting playground and gives the opportunity to tailor heterostructures with controlled and unique properties [107].

## 3.3 Moiré superlattice and Hofstadter butterfly in graphene

The unique electronic properties of graphene, caused by massless Dirac fermions, have motivated several theoretical simulations, investigating its behavior in periodic superlattice potentials [108, 109, 110]. In contrast to the Schrödinger equation for nearly free electrons subjected to a periodic potential, the Dirac equation for graphene's chiral particles does not predict the opening of a band gap [108]. Instead, periodic potentials are expected to cause an anisotropic particle propagation and generate additional Dirac points at energies $E = \pm\hbar v_F \left|\vec{G}\right|/2$, where electron and hole bands touch [109, 111]. Here, the energy is given by the reciprocal superlattice vector $\vec{G}$ and the Fermi velocity $v_F$.

Originally, hBN-graphene heterostructures have been used because of their far superior electronic qualities compared to graphene on $\mathrm{SiO}_2$. Owing to the similar hexagonal lattice structure of hBN and graphene and their lattice mismatch of only 1.8 %, stacks of both materials exhibit a rotation-dependent moiré pattern. Scanning tunneling microscopy (STM) experiments suggest that the arising superlattice moiré structure is causing an effective periodic potential to graphene and confirm the formation of new Dirac points at the expected energies near the edges of the superlattice Brillouin zone (SBZ) [111]. Considering the lattice mismatch $\delta$ between hBN and graphene, the relative rotation angle $\phi$ between the lattices and the graphene lattice constant $a$, the moiré wavelength $\lambda$ can be

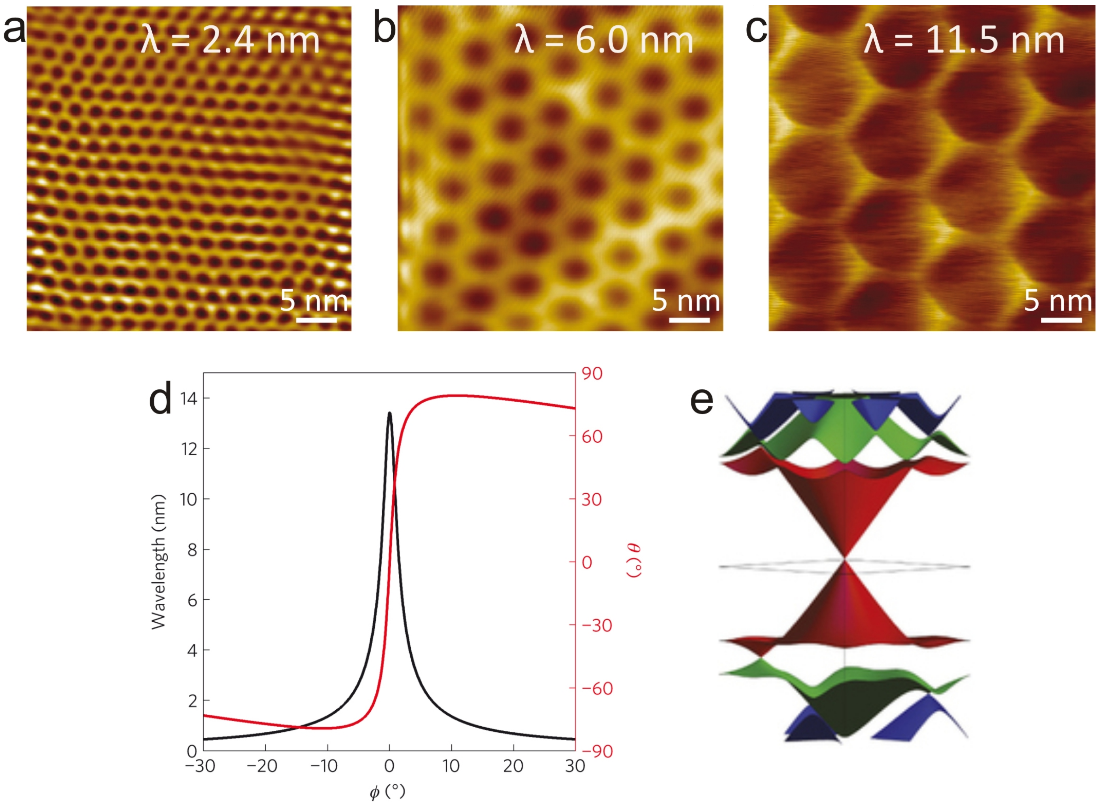

**Figure 3.4:** Moiré superlattices in hBN-graphene heterostructures. **(a)** - **(c)** STM images of different hBN-graphene superlattices with corresponding moiré wavelength $\lambda$. **(d)** Superlattice wavelength (black) and rotation (red) as a function of the angle between graphene and hBN lattices. **(e)** One of the theoretically proposed scenarios for the low-energy band structure. Fig. from [111, 112].

determined as

$$\lambda = \frac{(1+\delta)a}{\sqrt{2(1+\delta)(1-\cos\phi)+\delta^2}} \tag{3.2}$$

Accordingly, the relative rotation angle $\theta$ between the moiré pattern and the graphene lattice can be written as

$$\tan\theta = \frac{sin\phi}{(1+\delta)-\cos\phi} \tag{3.3}$$

Fig. 3.4a-c shows STM topography images of three aligned hBN-graphene stacks with rotation angles $\phi \leq 3°$ and the corresponding moiré wavelength $\lambda$ [111]. The arising moiré superlattice pattern is nicely resolved and the different length of $\lambda$ can be easily understood. The relation between rotation angles $\phi$, $\theta$ and wavelength $\lambda$, described by the equations above, is plotted in Fig. 3.4d. Owing to the lattice mismatch between hBN and graphene, there is a moiré pattern for any rotational alignment of the two layers. But the wavelength has a maximum of $\lambda \approx 14$ nm and is strongly decreasing with increasing rotation angle.

Moreover, assuming a filled band model, we can deduce the moiré wavelength $\lambda$ from gate sweep experiments according to [113]

$$\frac{n_{sat}}{n_0} = g_s g_v, \tag{3.4}$$

where $n_{sat}$ is the field effect density at the satellite peak position, $n_0 = 1/A$ ($A = \sqrt{3}a^2/2$) is the unit cell area of the moiré pattern, and $g_s$ and $g_v$ are the spin and valley degeneracy, respectively. $n_{sat}$ can be calculated following a standard plate capacitor model with $n_{sat} = C_g(V_{sat} - V_{cnp})/e$ and the solution for the moiré wavelength can be written as

$$\lambda = \sqrt{\frac{8e}{\sqrt{3}C_g(V_{sat}-V_{cnp})}} \tag{3.5}$$

The bandstructure in a hBN-graphene superlattice is quite complicated and different from pure graphene. One of the theoretically calculated scenarios for the low-energy bandstructure can be seen in Fig. 3.4e, where the second-generation Dirac cones are singly and triply degenerate for the valence and conduction bands, respectively [112]. Nevertheless, there is an ongoing debate about the exact shape of the superlattice dispersion, especially in the vicinity of the charge neutrality point [114]. Some transport experiments propose a gap of decreasing size with reducing moiré wavelength [115, 116], while other groups cannot observe any gap [117].

As an explanation, Woods *et al.* found the presence of a gap being dependent on the encapsulation of the graphene layer. They only observed gaps for

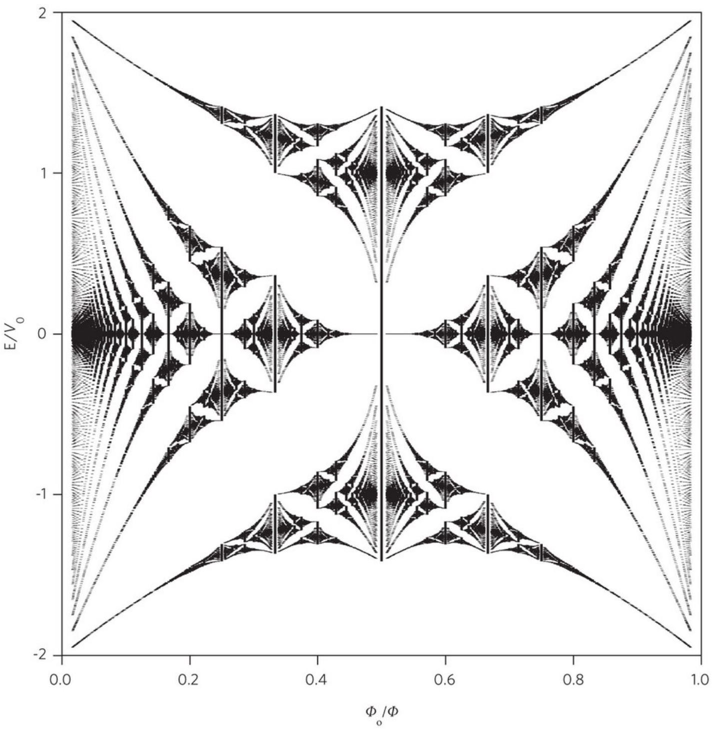

**Figure 3.5:** Hofstadter's butterfly with energy levels E of Bloch electrons in a magnetic field. Graph shows the limit of weak modulation, where the inverse magnetic flux ratio $\Phi_0/\Phi$ determines the internal structure of a Landau band. The spectrum was calculated for a square lattice potential with the same energy modulation amplitude $V_0$ along x and y directions [121].

non-encapsulated hBN-graphene heterostructures and attributed this aspect to a difference between a commensurate and incommensurate state of the moiré superlattice [118]. However, Gorbachev *et al.* saw a band gap in both encapsulated and non-encapsulated devices by probing the valley Hall effect at zero magnetic field [119]. They explain this experimental discrepancy by two routes. First, inhomogeneity in the system causes electron-hole puddles, and by tuning the Fermi energy, the small gaps will be covered by this fluctuations [34]. Alternatively, edge states could short the gap and decrease its visibility [120].

The Hofstadter butterfly represents one of the first quantum fractals discovered in physics and results from the interplay of a periodic potential and a magnetic field on 2D charge carriers [122]. On the one hand, 2D electrons moving in a periodic lattice potential, called Bloch electrons, are developing a quantized spectrum of discrete energy bands. On the other hand, electrons in 2D devices subjected to a magnetic field, develop degenerate Landau levels. Now, the interplay between both fields leads to a development of energy levels when the ratio of magnetic flux $\Phi$ through the lattice unit cell to the magnetic flux quantum $\Phi_0$

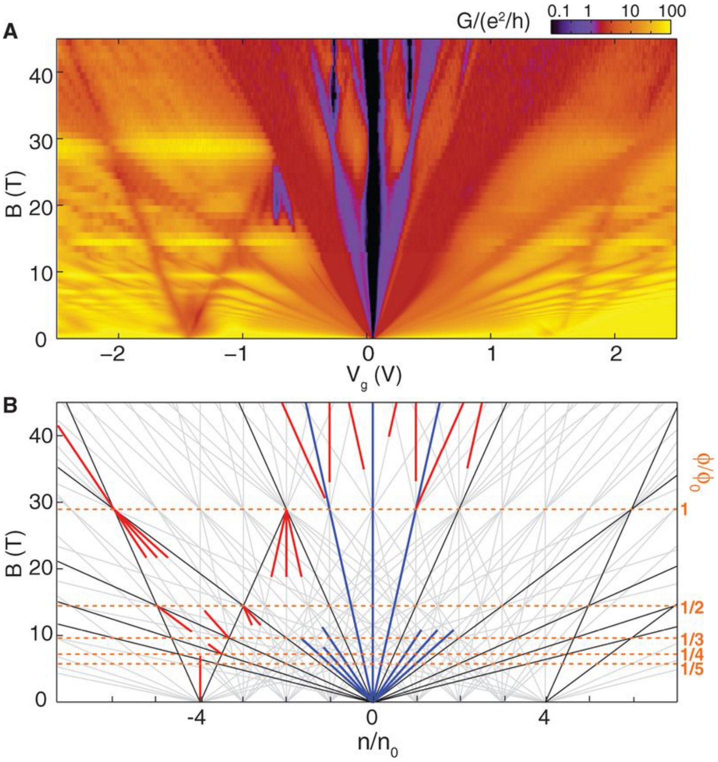

**Figure 3.6:** Hofstadter butterfly in graphene. **(a)** Magnetoconductance of a graphene-hBN heterostructure with almost perfect rotational alignment. Landau fans originate from the main Dirac point as well as from the superlattice Dirac points. **(b)** Corresponding theoretical calculation, where black lines represent gaps requiring no broken symmetry, and blue and red lines are broken symmetry states of the main and the satellite Landau fans, respectively. Fig from [115].

is a rational number [123]:

$$\Phi/\Phi_0 = Ba^2e/h \equiv a^2/2\pi l^2 = p/q \tag{3.6}$$

As a result, there is a quasi-continuous distribution of incommensurate quantum states with a self-similar recursive structure, where electron bands split into $p$ sub-bands when the flux $Ba^2$ through one unit cell is a rational multiple of the flux quantum $h/e$ [113, 124].
The resulting fractal energy spectrum for a square lattice, calculated by Douglas Hofstadter, is plotted in Fig. 3.5 [122]. However, as the unit cell in typical crystals is very small, and consequently the magnetic fields required for one flux quantum per unit cell are very high, experimental studies of the Hofstadter butterfly were restricted to artificial superlattice structures in 2DEGs [125, 126].

In carefully aligned hBN-graphene heterostructures, the properties of graphene are strongly modified by a hexagonal superlattice potential stemming from the hBN substrate, and the superlattice wavelength can be as large as $\lambda \approx 14$ nm. The significantly larger superlattice unit cell compared to graphene allows the experimental exploration of the Hofstadter energy spectrum for Dirac-type electrons. Thus, replicas of the main Dirac spectrum appear at the edges of the superlattice Brillouin zones, and the secondary Dirac cones can be accessed via electric field doping [112]. Exposing moiré heterostructures to magnetic fields gives rise to self-similarity in the form of many replicas and their quantization leads to the fractal pattern of Landau levels, characteristic for the Hofstadter butterfly.

Transport experiments showed Landau fans originating from both the original and the superlattice potential (see Fig. 3.6a) [115, 117, 113]. At low magnetic fields the satellite Landau fans can only be accessed by tuning the carrier density via back gate. However at higher fields, Landau levels originating from the original and the extra Dirac points cross for $\Phi/\Phi_0 = 1/q$, proving the expected recursive spectrum. Fig 3.6b depicts a simulation according to Wannier's theory, where energy gaps in the Hofstadter spectrum are constrained to linear trajectories $\Phi/\Phi_0 = (n/n_0 - s)/t$ in the density-field diagram [127]. Here are $s$ and $t$ integers denoting the Bloch band filling index and the quantized Hall conductance of the gapped state, respectively [115]. This plot allows to identify the origin of the different broken symmetry states in the experimental data.

Recently, Chen *et al.* reported the emergence of tertiary Dirac points in magnetotransport experiments on graphene moiré superlattices [128]. This set of further Dirac points gives rise to additional sets of Landau levels in a magnetic field, which proves the emergence of a miniband. By analyzing the Zak oscillations [113, 117] (magnetic flux penetrates the unit cell area of the superlattice in unit fractions with periodicity $1/Bq$) at the tertiary Dirac points, the authors estimated a superlattice wavelength of over 21 nm, which was about $\sqrt{3}$ times larger than the moiré wavelength $\lambda$. This observation suggests the formation of an additional superstructure on top of the moiré superlattice in highly-aligned hBN-graphene heterostructures [128].

# CHAPTER 4

# Commensurability features in lateral superlattices

Lateral superlattices in conventional semiconductor heterostructures have been studied intensively and revealed several novel phenomena in mesoscopic transport. Commensurability features, arising from the interplay of the magnetic miniband structure and the periodic electrostatic modulation, were probed in various experiments employing 1D [13, 129] and 2D superlattice potentials [14, 130]. Recent advances in fabrication techniques and sample quality allowed the observation of commensurability features in 2D etched graphene antidot lattices [10, 131].

The recursive spectrum of the Hofstadter butterfly, discussed in the section before, is one feature generated by a commensurate relation of magnetic field and 2D periodic potential. In this chapter, additional commensurability features, arising in magnetotransport experiments on potential-modulated 2DEGs, will be introduced. Overall, two different regimes can be classified by the imposed superlattice potential $V_0$. We will discuss transport characteristics of weakly perturbed systems $V_0 \ll E_F$, exhibiting distinct commensurability oscillations, and of antidot lattices, featuring dominant commensurability peaks for strong potential modulation $V_0 > E_F$.

## 4.1 Weiss oscillations for weak 1D modulation

Originally, Weiss *et al.* reported a new set of magnetoresistance oscillations in semiconductor 2DEGs with an induced 1D periodic potential [13]. The novel oscillations, known as Weiss oscillations, were periodic in $1/B$ and could be observed in weakly modulated 2DEGs with sufficiently high electron mean free paths (see Fig. 4.1). The authors used a L-shaped sample geometry and could probe

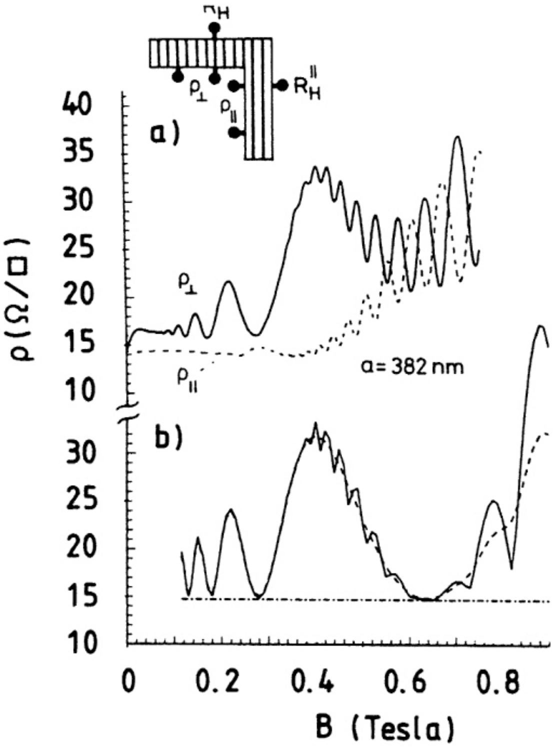

**Figure 4.1:** Weiss oscillations in a weakly modulated 2DEG. **(a)** Magnetoresistance traces of a sample shown in the inset. The solid and broken curves represent the data with current perpendicular and parallel to the stripes, respectively. (b) Calculation for $T = 2.2$ K (solid) and 4.2 K (dashed line). Fig. adapted from [132].

the magnetoresistance perpendicular and parallel to the imposed 1D potential modulation in the system. In addition to the Shubnikov-de Haas oscillations at higher fields, they observed another set of $1/B$-periodic oscillations at low fields. The minima of the Weiss oscillations in $\rho_{xx}$, perpendicular to the modulation, could be characterized with the commensurability condition for cyclotron radius $R_C$ and potential period $a$ [123]:

$$2R_C = (\lambda - \frac{1}{4})a \qquad\qquad \lambda = 1, 2, ... \tag{4.1}$$

which gives a periodicity for the oscillations of:

$$\Delta\frac{1}{B} = \frac{ea}{2\hbar\sqrt{2\pi n_s}}. \tag{4.2}$$

Here, $\Delta(1/B)$ is the distance between two neighboring minima. A similar condition holds for the minima in $\rho_{yy}$, parallel to the stripes. The only remarkable difference is a shift by half a period: $2R_C = (\lambda + 1/4)a$.

The origin of the commensurability oscillations can be explained with modifications of the Landau level energy spectrum [133]. Winkler *et al.* [129] and Gerhardts *et al.* [132] proposed that Weiss oscillations are a result of the oscillating bandwidth of modulation-broadened Landau levels. Hence, the arising group velocity leads to a strongly anisotropic, oscillatory Landau band-conductivity in the modulated 2DEG.

The following discussion on Weiss oscillations for a weak superlattice potential will be mostly referring to the derivations given in references [134, 132]. For a weak, cosine-type potential modulation $V_0 \ll E_F$ along the $x$-axis and a uniform magnetic field in $z$-direction, the one-electron Schrödinger equation can be written as:

$$\left\{ \frac{\hbar^2}{2m^*} \left[ \left( \frac{\partial}{i\partial x} \right)^2 + \left( \frac{\partial}{i\partial y} - eBx \right)^2 \right] + V_0 \cos(Kx) \right\} \psi(x,y) = E_n \psi(x,y), \tag{4.3}$$

where $K = 2\pi/a$ is the wavevector of the potential modulation. Without the potential term, the formula would give a series of Landau levels $E_n = \hbar\omega_c(n+1/2)$ with a degeneracy $1/2\pi l^2$ regarding the guiding center coordinate $x_0 = -k_y/l^2$, for each of them. Here, $l = \sqrt{\hbar/eB}$ is the magnetic length. However, the presence of a potential lifts the degeneracy of the Landau levels and generates Landau bands. The subband dispersion may be derived perturbatively:

$$\begin{aligned} E_n(k_y) &= \hbar\omega_c(n+1/2) + \langle n x_0 | V_0 \cos(Kx) | n x_0 \rangle \\ &\approx \hbar\omega_c(n+1/2) + V_0 J_0(KR_C)\cos(Kx_0), \end{aligned} \tag{4.4}$$

where $R_C = \hbar k_F/eB$ is the cyclotron radius at the Fermi level and $k_F$ is the Fermi wavevector. Now, the Landau band dispersion vanishes at zeros of the asymptotic Bessel function

$$J_0(KR_C) = \sqrt{2/\pi K R_C}\cos(KR_C - \pi/4), \tag{4.5}$$

which can be approximated as

$$2R_C = (\lambda - 1/4)a, \qquad \lambda = 1, 2, ... \tag{4.6}$$

This is the commensurability condition for cyclotron radius and potential period, which was observed experimentally [13]. The dependence of the Landau level width on the center-coordinate $x_0$ (a) and the magnetic field (b) is depicted in Fig. 4.2. Broad and narrow bands are alternating for different quantum numbers $n$ and the density of states oscillates over a large energy scale compared to the cyclotron separation $\hbar\omega_c$ [135]. This behavior is resulting in a strong temperature-robustness of the Weiss oscillations compared to Shubnikov-de Haas oscillations [13, 136]. Whenever the commensurability condition is fulfilled, the Fermi bands become flat, the density of states becomes maximum and the electron velocity at the Fermi level vanishes [134]. On the contrary, an increasing dispersion (width) of the Landau bands results in a smaller density of states. The correlated oscillating band-conductivity can be calculated based on Kubo's formulas, where the conductivity of a periodically modulated 2DEG depends on the square of the

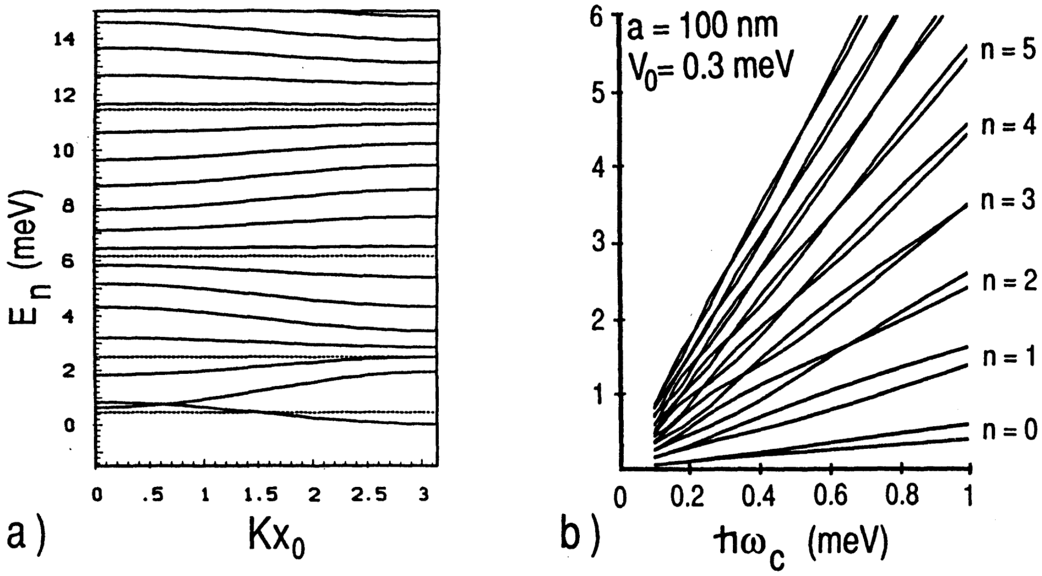

**Figure 4.2:** Landau band dispersion in a weak periodic potential. **(a)** Landau band dispersion for $B = 0.5$ T, $V_0 = 1.5$ meV, and $a = 100$ nm according to equation 4.4. The flat band situation is marked by the dotted lines. **(b)** Band width oscillations as function of $B \propto \hbar\omega_c$. Fig. adapted from [132, 135].

DOS at the Fermi energy [137].

Another explanation for the appearance of Weiss oscillations in weakly modulated 2DEGs can be given in a semi-classical picture, proposed by Beenakker and van Houten [138, 139]. This is a valid approach, as long as the Fermi wavelength $\lambda_F = 2\pi/k_F$ is small compared to the potential period $a$, and consequently, the electrons can be treated semi-classically [123]. The authors report a classical analogue of the band-conductivity, which they call “guiding center drift resonance”. In this picture, the commensurability oscillations can be explained by an average $\vec{E} \times \vec{B}$-drift of the center-coordinate of the cyclotron motion, where $E$ is the periodic potential in $x$-direction and $B$ the perpendicular magnetic field. The center of the cyclotron orbits drifts along the $y$-direction and the drift velocity $v_d$ vanishes only for the $2R_C = (\lambda - 1/4)a$. The experimentally observed oscillations of the longitudinal resistivity $\rho_{xx}$ can be explained according to a Boltzmann transport picture for an oscillating drift velocity $v_d$.

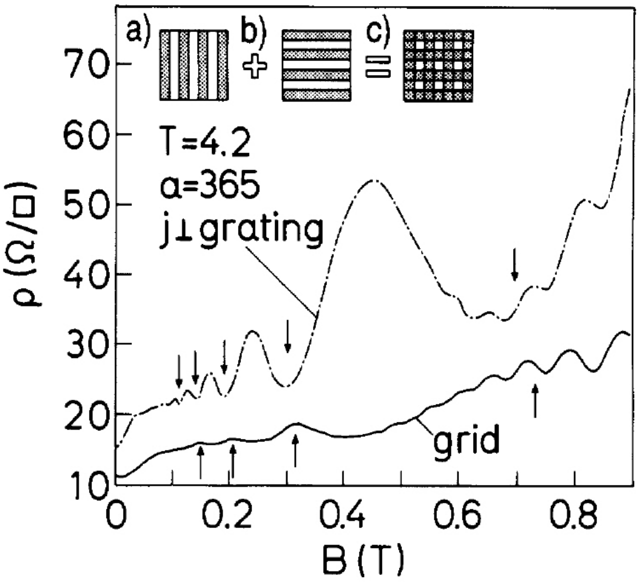

**Figure 4.3:** Magnetotransport in a weak, 2D-periodic potential. First, a 1D-periodic modulation is probed, featuring Weiss oscillations with minima for flat bands. Subsequently, a second illumination with a 90° rotation is performed and the magnetotransport trace features weak maxima for the commensurability condition in equation 4.6. Fig. adapted from [133].

## 4.2 Commensurability features for weak 2D modulation

The energy spectrum becomes even more complicated for 2D superlattice modulation [122, 140]. As discussed in section 3.3, a weak 2D-periodic potential modulates the Landau level spectrum, depending on the flux $\phi = Ba^2$ per unit cell, and the Landau bands split into $p$ subbands for

$$\phi/\phi_0 \equiv a^2/2\pi l^2 = p/q, \tag{4.7}$$

This equation is an additional commensurability condition and the corresponding energy spectrum is known as the Hofstadter butterfly.
The Landau level width, however, is modulated in a very similar way as in the 1D-periodic case (equation 4.4). In this way, the flat band condition is the same for 1D and 2D modulation [141, 133].

Fig. 4.3 depicts an experiment of Weiss *et al.* on 2D-periodic potentials ($V_0 \ll E_F$), created by successive holographic illumination of a high-mobility GaAs-AlGaAs heterostructure. Again, the illumination (1D in a first step) produces additional magnetoresistance oscillations at low magnetic fields due to an additional band-conductivity. The dashed-dotted trace in the graph displays minima for the flat band condition (positions marked by arrows). Subsequently, a second illumination pattern is rotated by 90° and the obtained results are plotted in the lower trace for the 2D grid. The magnetoresistance for 2D modulation is considerably decreased, but there is still a weak oscillating behavior according to the commensurability condition in equation 4.6, manifesting in maxima for flat bands. Therefore one can conclude that the band-conductivity oscillations are considerably suppressed in the 2D-periodic case, and the observed maxima are induced by scattering rate oscillations, displaying maxima for the flat band condition [141, 133].

However, this mechanism seems only valid for 2D-periodic modulation in high-mobility 2DEGs. Several different groups observed $1/B$-periodic oscillations with minima for $2R_C = (\lambda - 1/4)a$ in 2D modulated samples [142, 143]. Similar to 1D modulation, these contributions can be attributed to band-conductivity oscillations. So commensurability oscillations in a weak 2D-periodic potential can feature maxima or minima for the flat band condition, depending on the mobility of the structures [123].

## 4.3 Strong Modulation: Antidot lattices

Several novel phenomena have been observed in antidot lattices in perpendicular magnetic fields, including quenching of the Hall effect and commensurability peaks in the magnetoresistance [14, 144, 145]. At the magnetic fields corresponding to the magnetoresistance peaks, the classical cyclotron orbit becomes commensurate to the antidot period and encircles a specific number of antidots and get pinned [146]. Additionally, fine quantum oscillations, superposed to the classical features were observed in some experiments [147, 148].

Antidot lattices are a periodic array of nanometer-sized discs, etched into a 2DEG. Initially, antidot lattices have been studied intensively in high-mobility semiconductor structures. The observation of antidot features in magnetotransport experiments requires a sufficiently large electron mean free path $l_e$ compared to the superlattice period $a$. Then, electron transport in the antidot array is ballistic and scattering is essentially induced by scattering at the etched holes rather then impurities. A sketch of the antidot lattice and the corresponding periodic potential landscape is depicted in Fig. 4.4. Etched antidot arrays are representing a strong superlattice potential with $V_0 > E_F$ and electrons moving at the Fermi surface are responsible for the magnetoresistance peaks.

Weiss *et al.* conducted measurements on GaAs-AlGaAs heterostructures, where they compared magnetotransport traces of patterned and unpatterned sample areas (see Fig. 4.5) [14]. There is an obvious influence of the antidot potential on the transport properties. The most important features arise at low magnetic fields, where two prominent peaks appear in $\rho_{xx}$. Correspondingly, several step-like, non-quantized features are present in the Hall resistance, similar

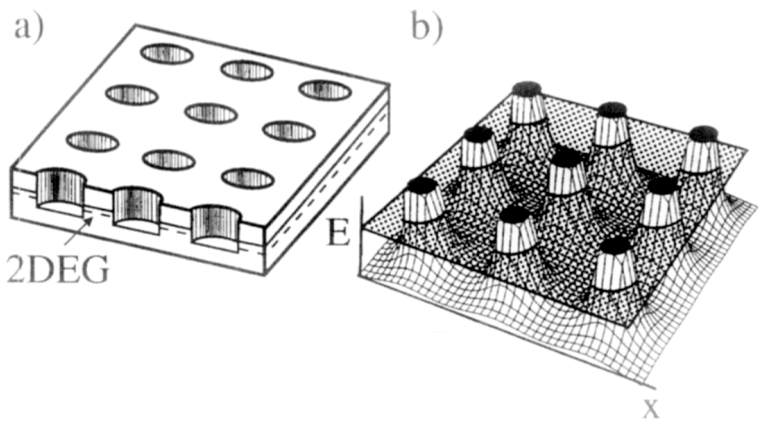

**Figure 4.4:** Schematic of an etched antidot array. **(a)** Sketch of an antidot array consisting of periodically arranged holes, etched into the heterostructure. **(b)** Corresponding potential landscape, probed by the electrons. Electrons moving at the Fermi energy, depicted by a semitransparent plane, are responsible for the commensurability features. Fig. adapted from [149].

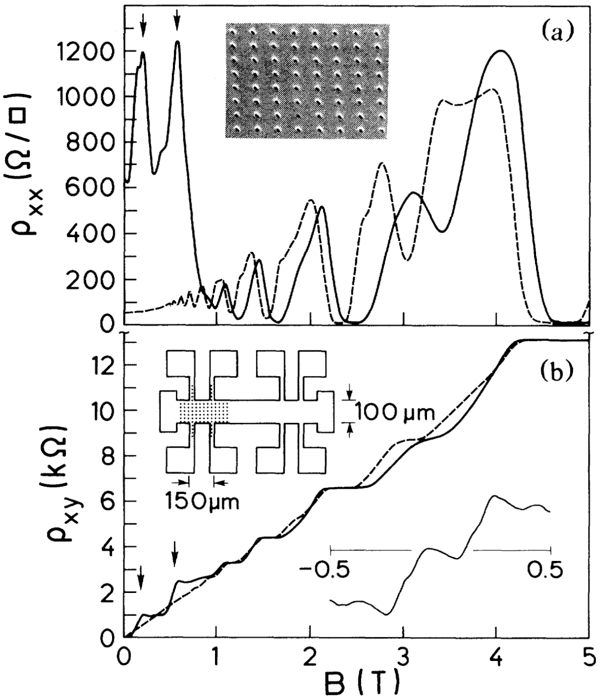

**Figure 4.5:** Magnetotransport in an antidot superlattice. **(a)** Magnetoresistance and **(b)** Hall resistance in patterned (solid line) and unpatterned (dashed line) sample segments at $T = 1.5$ K. The arrows mark magnetic field positions where $R_C/a \approx 0.5$ and 1.5. Inset of **(a)** shows the etched antidot array. Insets of **(b)** depict a sketch of the sample geometry and a magnification of the quench in $\rho_{xy}$ around $B = 0$. Adapted from [14].

to the unpatterned device. Thus, the high intrinsic mobility of the 2DEG is preserved, despite the relatively small antidot period of $a = 300$ nm. At zero field, however, the mobility is limited by scattering off the antidots [149]. Each peak in the magnetoresistance trace can be attributed to a commensurate orbit around a specific number of antidots. Nevertheless, the number of peaks in the experiment critically depends on the effective diameter $d$ and the period $a$ of the potential. The larger the ratio $d/a$ the fewer peaks are observable in the longitudinal resistance.

Commensurability peaks are emerging at magnetic fields, where the cyclotron orbits with radius $R_C = \hbar\sqrt{2\pi n_s}/eB$ are matching the imposed antidot lattice. Therefore, the most dominant peak, the so-called fundamental antidot peak, is for $2R_C = a$. However, at higher fields, where the cyclotron orbits are smaller than the neck width $a-d$ of the square antidot lattice, the longitudinal resistivity drops rapidly and quantum Hall features arise.

As an explanation, the authors proposed a model based on “pinned orbits”, where electrons running on commensurate orbits around one or several antidots do not contribute to charge transport, and hence, peaks in the magnetoresistance appear. This chaotic pinball model, where electrons are non-interacting spheres, scattered by a periodic array of columns of infinite strength, is closely related to the so-called Sinai billiard [150].

The approximation, given above, is a good one, as long as the effective potential steepness is very high. Otherwise the pinball model has some weakness in explaining specific aspects of the antidot system, e.g. the peak corresponding to $n = 4$ antidots [151]. Numerical simulations based on classical transport suggested that chaotic motion of electrons as an origin of the commensurability peaks (FGK model) is more important [152]. Fleischmann *et al.* suggested that not primarily pinned regular orbits, but chaotic orbits with a character close to the periodic orbits give the largest contribution to the peaks. Actually, the change in the volume of the pinned orbits in the phase space is not enough to induce the pronounced antidot peaks.

Additionally, trajectories skipping regularly from antidot to antidot in the same direction, so-called “run-away” trajectories, can contribute to the formation of antidot features [153].

# CHAPTER 5

## Sample fabrication and experimental setup

The transport characteristics of graphene can be significantly improved by employing heterostructures with hexagonal boron nitride, and thus, novel phenomena can be experimentally explored.

In this chapter, we want to show the key elements of the fabrication methods and subsequent patterning techniques for graphene based heterostructures. Starting with the standard "Scotch tape" exfoliation method and characterization of suitable graphene and hBN flakes, the main focus of this chapter will be on the dry-transfer process we used for the fabrication of the van der Waals heterostructures for our devices. Therefore, the transfer procedure will be introduced and the advantages will be compared to the former wet-transfer method. Additionally, we will discuss different patterning techniques that can be implemented in this process and the influence of thermal annealing on the assembled stacks. We report the advantages and versatility of few-layer graphene patterned bottom gates, which were also published in reference [12]. In the end, the used measurement setup will be introduced.

### 5.1 Mechanical exfoliation of graphene and hBN

As a first step towards hBN-graphene heterostructures, flakes of both crystals need to be prepared and characterized. In order to get suitable flakes from both materials, we need to employ mechanical exfoliation or chemical vapor deposition (CVD). For a long time, CVD-grown graphene gave the possibility for large scale applications, but its quality was limited due to defects and grain boundaries. So exfoliated, single-crystalline graphene flakes were the material of choice for devices with the highest electronic quality. Although this general statement is no

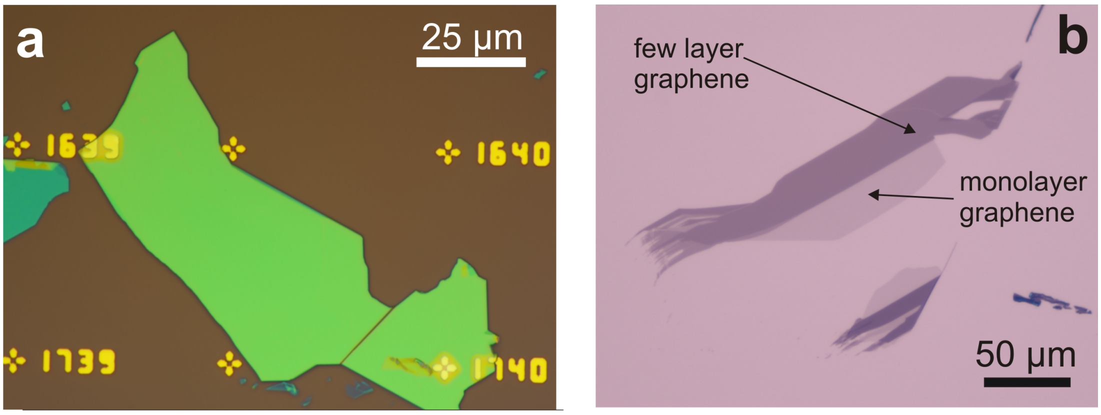

**Figure 5.1:** Exfoliated graphene and hBN crystals on a Si/SiO$_2$ substrate. **(a)** Optical micrograph of a hBN flake with a thickness of several tens of nm. The Cr/Au markers are deposited for easier identification and subsequent handling. **(b)** Microscope image of graphene flakes of different thicknesses. The lowest optical contrast is for monolayer graphene flakes.

longer true and the quality of CVD-based graphene has considerably improved [105, 154], exfoliated graphene is still more practical and common for small scale and customized devices. Mechanical exfoliation is based on micromechanical cleavage of 2D bulk crystals such as graphite, hBN, MoS$_2$, or NbSe$_2$. The most important requirement for the materials is a strong in-plane and a weaker out-of-plane binding.

All heterostructures in this work were assembled with exfoliated crystals obtained from natural graphite or HOPG (**H**ighly **O**riented **P**yrolitic **G**raphite) and hBN single-crystals, provided by T. Taniguchi and K. Watanabe [155]. Therefore, individual layers of the material can be cleaved and put on an appropriate substrate. As substrates for exfoliation and subsequent analysis, Si/SiO$_2$ wafers with a specific oxide thickness (e.g. 285 nm) are commonly used. Here, the thickness of the SiO$_2$ layer is critical for the optical contrast of the exfoliated crystals and needs to be tuned properly for the observation and identification of few-layer flakes [156]. Additionally, we use different band pass filters for the enhancement of the contrast of thin hBN flakes.

For the exfoliation of the crystals, we start with an adequate tape (ELP BT-150ECM, Nitto Denko Corp.), cleave the bulk crystal several times and press it on the Si/SiO$_2$ substrate. After suitable force for enhancing the attachment between flakes and substrate, the tape will be peeled off and leave flakes of different thickness on the target substrate. The lateral size of the exfoliated crystals can be as large as one millimeter for thick and hundreds of micrometers for monolayer flakes. Fig. 5.1 shows exemplary exfoliated hBN and graphene flakes on Si/SiO$_2$ wafers. Some of the substrates we use are pre-patterned with an array of Cr/Au

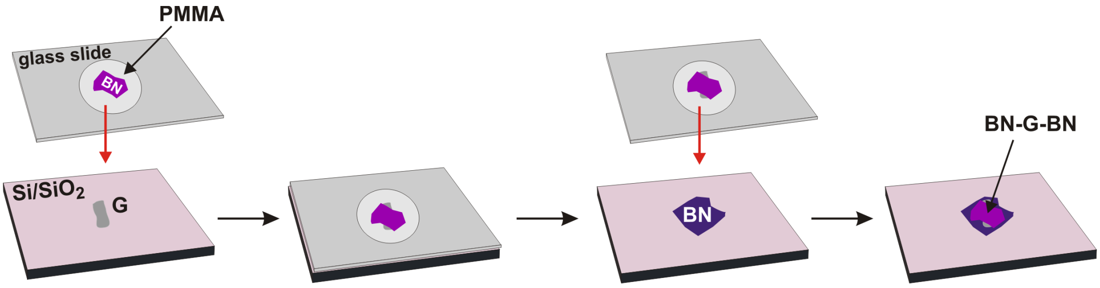

**Figure 5.2:** Schematic of mechanical dry-transfer process for van der Waals heterostructures. A hBN flake on a freestanding PMMA membrane is brought into contact with a graphene flake on a Si/$SiO_2$ substrate. Strong van der Waals forces between the 2D materials allow to lift the graphene crystal, and once again, the stack is put onto a hBN flake. Subsequently, the PMMA layer is dissolved and the encapsulated graphene structure is finished.

markers in order to simplify the identification and the further processing of the devices. Obviously, the markers are limiting the lateral size of the exfoliated flakes, so we only use them for the bottom flake of any heterostructure. In this way, we take advantage of the markers, but aren't restricted to smaller flake sizes in the following transfer process.

## 5.2 Transfer methods and 1D edge contacts

The most important point for assembling van der Waals heterostructures is to stack the layers with the least possible contamination. Overall, there are many different transfer techniques, utilizing various polymers, but generally we can distinguish between a wet transfer and a dry transfer method.

During a wet transfer, the flakes will get exposed to water or solvents, which can cause contamination and strongly decrease the properties of graphene. One example for this process is spinning PMMA on graphene on Si/$SiO_2$ and subsequent etching of the supporting substrate with KOH. After that, the PMMA layer with graphene is floating on top of KOH and can be transferred on top of another crystal.

Another method is the layer-by-layer transfer, which allows to stack one layer after another, and processing of each of them can be done sequentially. On the one hand, this approach offers a high flexibility in device geometries, but on the other hand it is very time-consuming, and even worse, all layers of the hybrid structure get exposed to polymers during stacking and patterning.

Obviously, these stacking methods are not perfect and most groups are using a dry van der Waals transfer technique, yielding higher sample quality, now. In our case, we use a co-laminating and restacking method for the assembly of our devices. The general idea is to exfoliate the upper flake of the future heterostruc-

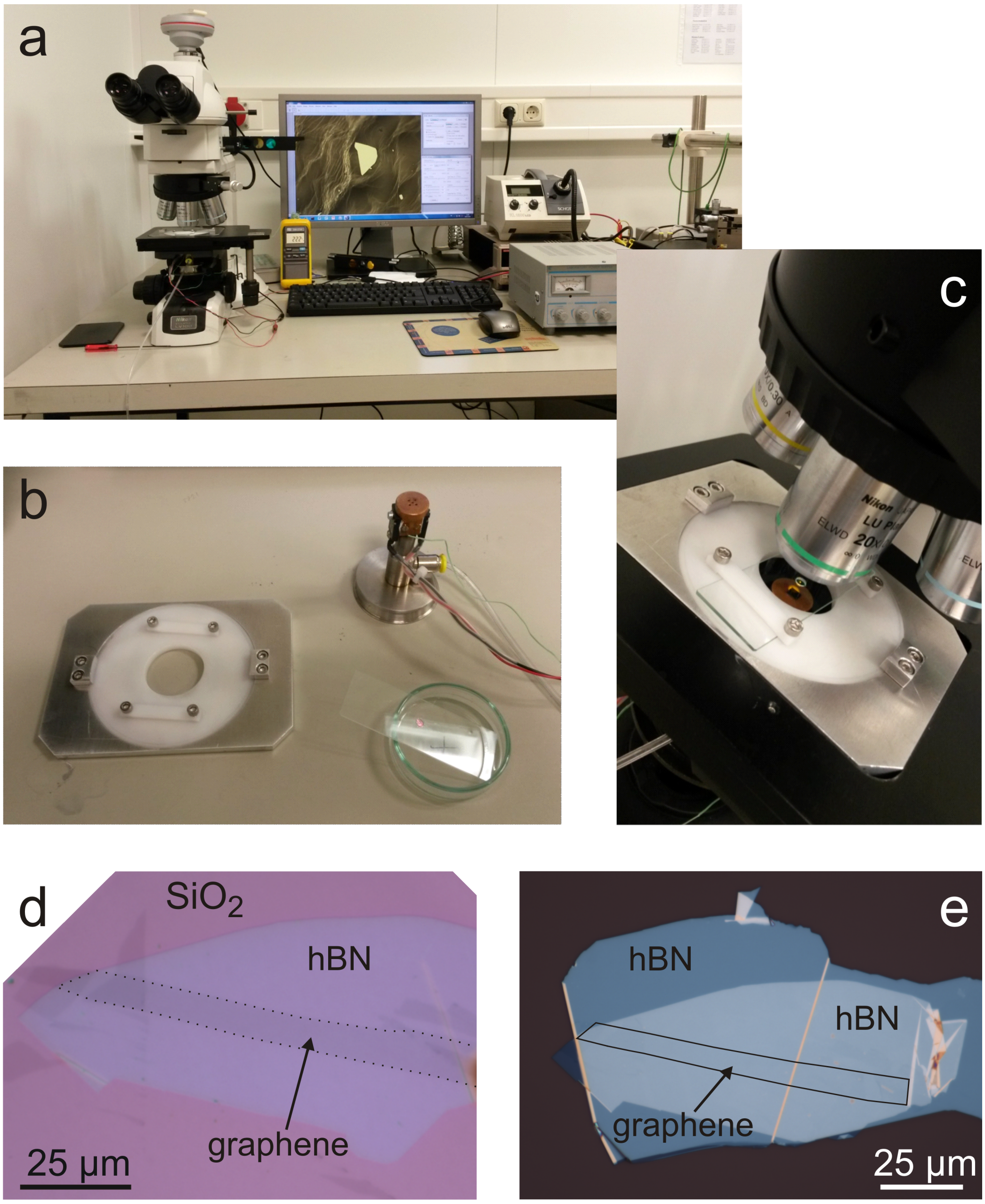

**Figure 5.3:** Transfer setup for heterostructures and assembled hBN-graphene-hBN stack. **(a) - (c)** One of our transfer setups that can be easily integrated in an optical microscope. Fig. adapted from [157]. **(d)** Optical micrograph of the first transfer step, showing the top hBN crystal on PMMA in contact with graphene on a Si/SiO$_2$ wafer. **(e)** Microscope image of a graphene stack, encapsulated between hBN, on Si/SiO$_2$. The black line is highlighting the graphene area.

ture onto a stack of polymers consisting of a sacrificial layer (PMGI in our case) and a PMMA transfer layer. Using this stack, we can pick-up further crystals. The transfer process is depicted in Fig. 5.2. First, we search for suitable hBN flakes on the polymer stacks with optical microscopy and band pass filters for enhanced contrast. Accordingly, we identify proper graphene and bottom hBN flakes, exfoliated on a Si/SiO$_2$ wafer. Since we want to avoid adsorbates such as water on our crystals, it is very important to start the transfer procedure right after cleaving the graphene and hBN flakes.

Starting with the top hBN on the polymer stack, we dissolve the sacrificial PMGI layer in photoresist developer. The highly hydrophobic PMMA layer is then floating on top of the water bath. After fishing the film with a glass slide, the suspended PMMA/hBN stack is inverted and mounted on an optical microscope. By using the micro manipulator of the microscope, the position of the hBN flake can be located and precisely aligned with respect to the graphene crystal located right beneath the glass slide. The graphene chip is heated up to approximately 80 °C during the transfer in order to support the adhesion of the PMMA, and alignment precision can be as good as a few $\mu$m. After attaching the crystals to each other, the PMMA layer is slowly peeled off the Si/SiO$_2$ chip and due to strong van der Waals forces between the two flakes, graphene can be lifted from the substrate. Similar to before, we repeat the procedure by lowering the hBN/graphene stack on the PMMA layer to a target hBN flake.

The assembled stack is heated up once more, and the PMMA layer is cut from the supporting glass slide, leaving the encapsulated graphene heterostructure and the polymer on top of the target wafer. Finally, the PMMA film is dissolved in acetone and the sample is annealed in flowing forming gas (N$_2$/H$_2$) at $320 - 400$ °C for several hours to remove resist residues and relax strain in the hybrid structure. One of our microscope-based transfer setups and the stacking of hBN-graphene hybrid structures, described above, can be seen in Fig. 5.3.

As discussed in section 3.3, hBN and graphene can form a rotation-dependent moiré pattern in heterostructures with well-aligned crystals. Unfortunately, it is often really hard to achieve very small rotation angles, and we needed several attempts to get a few stacks that were showing the moiré superlattice structure. In many cases it is difficult to identify crystallographic edges of hBN and especially of graphene, and without more complicated techniques (e.g. Raman spectroscopy), we cannot clearly distinguish between zigzag and armchair edges of hexagonal crystals.

Fig. 5.4a,b depicts the transfer of a hBN-graphene-hBN structure with almost perfect rotational alignment of two crystals ($\phi < 1°$).

After the transfer procedure, the stacks undergo further fabrication steps. Considering the encapsulation of graphene between two hBN flakes, any environmental influences, such as residues from patterning, can be avoided. While the

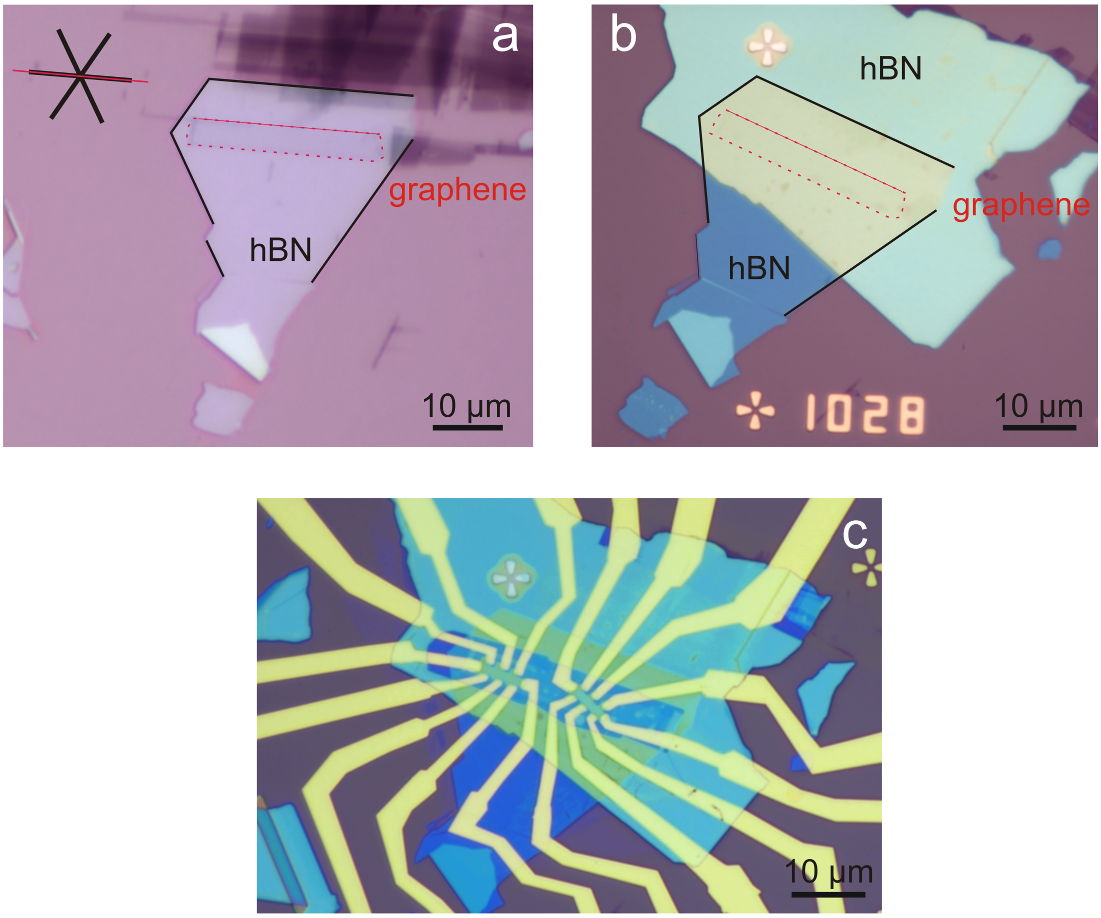

**Figure 5.4:** Micrographs of a hBN-graphene heterostructure with crystallographic alignment of two flakes. **(a)** Van der Waals pick-up of graphene with a hBN flake on PMMA. The black highlighted edges form angles of 120° and follow the crystallographic edges of the hBN flake. One edge of the graphene flake (red) is aligned to an edge of the hBN crystal (see inset). **(b)** Assembled heterostructure, with graphene aligned to the top hBN flake and randomly rotated with respect to the bottom hBN. **(c)** Finished hybrid structure after stacking, etching of the Hall bars and metallization of the 1D side contacts.

van der Waals pick-up allows a fast and convenient assembly of hybrid structures, the subsequent etching and contacting methods are highly non-trivial. Wang *et al.* reported a novel contact geometry in which they metalized 1D edge contacts to the 2D graphene sheet [98]. Therefore, a hard mask for etching is prepared and the whole hBN-graphene-hBN stack is submitted to $CHF_3/O_2$ or $SF_6$ based reactive ion etching (RIE). The profile of the stack is sloped because of the isotropic plasma etching, and subsequently, reliable 1D side contacts (Cr/Au) can be evaporated at the edges of the heterostructures. An equivalently patterned stack with two Hall bar structures can be seen in Fig. 5.4c.

Obviously this method is a huge improvement, allowing to separate the layer assembly and the further patterning steps for high-quality graphene structures. However, there are also some disadvantages of this method, such as limits for top and bottom gate geometries.

## 5.3 Thermal annealing of van der Waals heterostructures

Any exfoliation, transfer or patterning step for hBN-graphene hybrid devices inevitably introduces contaminants on their surfaces, and we found electron beam lithography and reactive ion etching to be the most critical fabrication steps. The residues cannot be simply removed by standard solvents such es acetone and isopropanol, and are obstinately remaining on the samples. As discussed before, this describes a problem for non-encapsulated hBN-graphene stacks, where graphene is exposed to any environmental influences.
A commonly used attempt to remove organic fabrication residues is heat treatment at moderate temperatures of 300 - 350 °C in $Ar/H_2$ or $N_2/H_2$ atmosphere [35]. However, we found this recipe to be ineffective at removing residues for many of our assembled heterostructures. This observation is in line with reports of other groups that performed Raman spectroscopy before and after the annealing cycles [158, 159].

Garcia *et al.* observed a clear evidence that annealing in $Ar/H_2$ atmosphere at 350 °C effectively removes adhesive residues from exfoliation, but organic contaminants remain virtually untouched . They used different atmospheres in their experiments and claimed that the annealing process is purely thermal at these temperatures and does not involve chemical reactions, introduced by the gaseous environment. However, at more elevated temperatures (500 °C), they see a strong influence on the atmosphere, with significantly better results for $Ar/O_2$ treatment [158].

Similar to this observation, Gong *et al.* report selective etching of polymer residues in oxidative atmospheres. In their experiments $CO_2$ annealing at 500 °C outperforms other commonly used recipes, because of its moderate oxidative strength to remove organic contaminates, while preserving the quality of the underlying graphene sheet [159].

Contamination of graphene can be mostly eliminated by employing the van der Waals stacking method for encapsulation of graphene. Nevertheless, annealing is an important fabrication step, performed right after the assembly of the heterostructure. While heat treatment cannot remove residues from the interfaces of the crystals, we often see a congregation of sparsely distributed contaminants after annealing. A heat treatment of 350 - 400 °C for several hours is supporting the self cleansing mechanism of the stack, forming larger pockets of trapped residues and wide areas of perfectly clean interfaces [104]. We cannot make a positive statement on the influence of annealing on the distribution of strain in our heterostructures, but we often observe a movement or extinction of wrinkles in the hybrid structure during heat treatment.

In addition to the improvement in quality, the annealing procedure can induce further alterations to a hBN-graphene heterostructure. Annealing can cause a thermally induced rotation of graphene on hBN, where twisting angles of $\phi = 0°$ and $\phi = 30°$ are two thermally stable configurations [160]. This method is a convenient approach for the fabrication of hybrid structures with imposed moiré superlattice. However, the cleanliness of the interface, the amount of trapped residues, and the flake sizes are influencing the thermally induced rotation.

## 5.4 Fabrication of graphene patterned bottom gates

In graphene, a local potential modulation can be imposed by various approaches, including chemical gating [161], geometrical variation [162], or patterned gate electrodes. Local gating can induce *pn*-junctions in graphene and generate unique effects such as Klein tunneling [83], Klein collimation [88], and lensing behavior [79].

Many of the early experiments with density-modulated graphene were relying on metallic top gates, separated from graphene by an evaporated insulating layer such as alumina. However, the electronic quality of graphene was significantly decreased by the deposited dielectric, fabrication residues and impurities [163, 12]. All these factors became negligible with the introduction of encapsulated hBN-graphene heterostructures. Nevertheless, the fabrication of metal top gates remained challenging, because usually the heterostructures require additional side-passivation steps to prevent shortcuts between the bare graphene edges and the metallic top gate. Furthermore, the stability and reproducibility of stripe-like metallic gates strongly depends on their dimensions, especially on

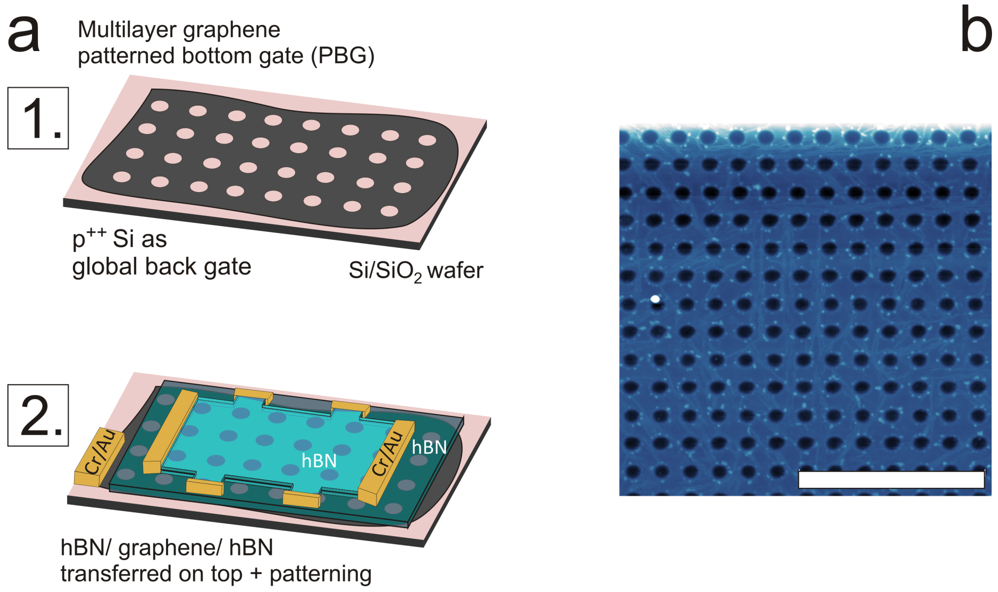

**Figure 5.5:** Few-layer graphene patterned bottom gate and subsequent stacking of the device. **(a)** Schematic of the fabrication steps for a device employing a multilayer graphene PBG. First, the few-layer graphene on the Si/SiO$_2$ wafer gets patterned with a hole array, using standard EBL and RIE. After that, an encapsulated graphene structure is transferred on top of the structured graphene, and further patterning steps are done. In this geometry, both gates, the global Si and the local graphene gate, can be independently contacted and tuned. **(b)** AFM image of a graphene PBG with a period of $a = 150$ nm and diameter $d = 75$ nm of the 2D hole array. Scale bar is 1 $\mu$m.

their widths. While relatively wide stripes (in the micrometer scale) are stable, narrow stripes in the range of a few tens of nanometers width tend to move on the chemically inert hBN surface, or even rip, when deposited over the edges of the mesa [12].

A convenient alternative for metallic top gates are local bottom gates, and different geometries, using metals, or planar and step-like graphite, have been reported [76, 115, 164]. While step-like metallic bottom gates are perfect for suspended graphene devices [42, 165], their finite height induces strain to van der Waals heterostructures, transferred on top.

Our method relies on the atomic flatness, negligible height and distinct stability of few-layer graphene as a versatile material for locally acting bottom gates [12]. Graphene gates can be easily implemented in the commonly used transfer methods and can be patterned to create any 1D or 2D periodic potential landscape, providing sharp potential steps. Furthermore, it was shown that graphite or few-layer graphene gates provide an improvement in sample quality compared to encapsulated graphene on $SiO_2$ by quenching the disorder potential as a screening gate. In this geometry, charged impurities at the surface of $SiO_2$ are exponentially suppressed over a few Thomas-Fermi screening lengths (a few $\mathring{A}$) in the bottom gate, and cannot influence the graphene sheet [98, 166].

Fig. 5.5a depicts a sketch of the fabrication of a device employing a 2D periodically patterned graphene bottom gate. For the preparation of the few-layer graphene gates, we select graphene flakes consisting of only a few layers to minimize spatial perturbation, but to assure full screening of the global back gate electric field. First, the multilayer graphene on the $Si/SiO_2$ wafer gets patterned with a hole array, using standard EBL and RIE (see also Fig. 5.5b). After that, an encapsulated graphene structure is transferred on top of the structured graphene gate and further fabrication steps such as etching of the Hall bar and evaporation of the contacts are performed. Similar to commonly used top gate geometries, the structured bottom gate and the global back gate can be independently contacted and tuned, in order to induce local potential modulation to the system.

## 5.5 Measurement setup

The transport measurements for our experiments were acquired in a four-terminal geometry, using standard AC lock-in technique at low frequencies. A schematic of the measurement setup can be seen in Fig. 5.6. The blue lock-in amplifier is used as a voltage source and the series resistor (1 - 10 MΩ), connected between lock-in and sample, ensures a relatively constant AC current for the experiment. In order to prevent Joule-heating and to preserve low electron temperatures in the device, we apply a current of 10 nA to the Hall bar structure. Additional lock-in amplifiers (green) can be used to independently probe the longitudinal (4-point)

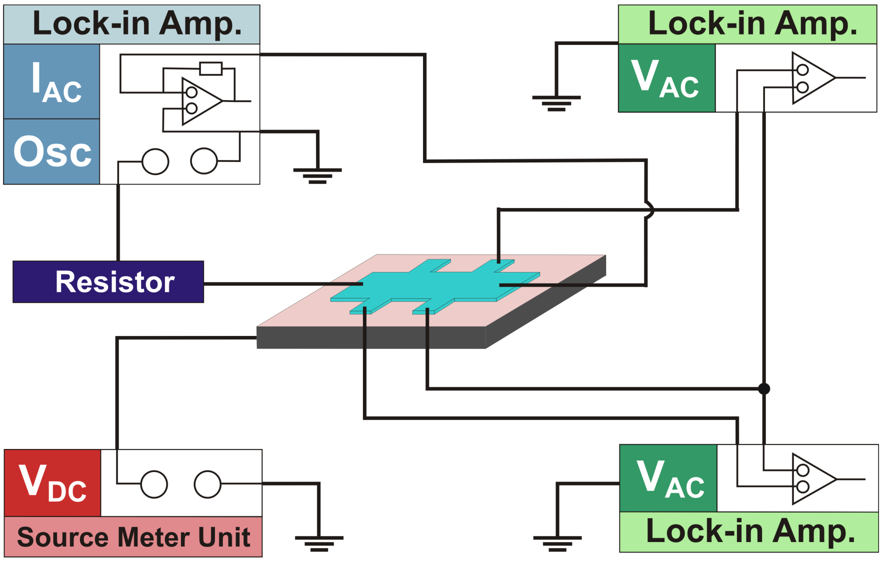

**Figure 5.6:** AC measurement setup for longitudinal and transverse voltage at a hBN-graphene heterostructure in Hall bar geometry, patterned on a Si/SiO$_2$ wafer.

and transverse voltage drop in the experiment. Thus, a Hall bar structure is the perfect geometry to examine transport properties, especially in applied magnetic fields. Typically, we use another lock-in for acquiring the 2-point voltage, but of course the setup can be adjusted to the specific needs of each measurement. In our experimental setups, we work with Signal Recovery 7265 lock-in amplifiers. The charge carrier density of graphene can be tuned with a source meter unit (Keithley 2400) by applying a DC-voltage to the global Si back gate.

For the transport experiments, we used two different $^4$He-cryostats from Oxford Instruments, which provide magnetic fields up to 14 T along the z-axis. The cryostats are equipped with a variable temperature insert (VTI), connected to the bath with a needle valve. Usually, the sample is not surrounded by liquid helium and the base temperature of the system is depending on the gas pressure in the VTI (T $\approx$ 1.3 K). An integrated heater can be used to increase the temperature up to 200 K.

# CHAPTER 6

# Ballistic transport in hBN-graphene heterostructures

The quality of a graphene sheet is significantly influenced by the supporting substrate and considerably limited on commonly used Si/SiO$_2$ wafers. However, many novel transport experiments require high mobilities and large electron mean free paths. Some interesting phenomena in high-mobility graphene include interaction driven quantum Hall effects, such as spin and valley quantum Hall ferromagnetism [6, 63, 7] and the fractional quantum Hall effect [8, 9] (see chapter 2.6.2). In graphene, strong Coulomb interactions and a fourfold spin-valley degeneracy cause a SU(4) isospin symmetry within its Landau levels. At partial filling of these LLs, exchange interactions can lift the degeneracy and polarize the ground state ferromagnetically, manifesting in all integer LL filling factors outside of the normal sequence [61]. At higher magnetic fields, quantized Hall plateaus at fractional filling factors appear that can be associated with the formation of a quantum liquid with topological order [21, 167].

In order to improve sample quality, we focused on hBN-graphene hybrid structures and introduced the associated transfer procedure in our lab [168]. Here, we want to report some of our experiments on graphene on hBN and encapsulated graphene that confirm the enhanced sample quality. We regularly observe mobilities exceeding several tens of m$^2$/Vs, giving us the possibility to examine ballistic transport features in graphene.

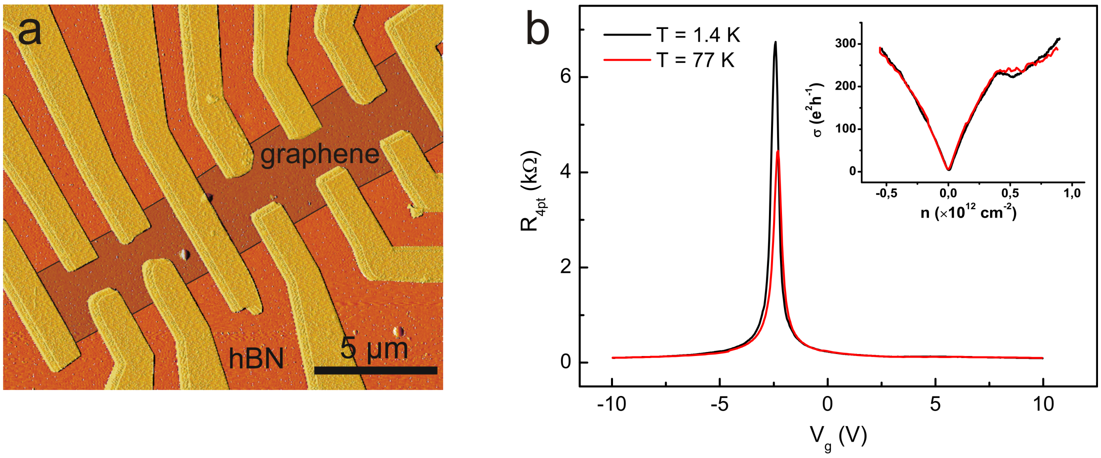

**Figure 6.1:** Graphene-hBN heterostructure. **(a)** False-color AFM image of a graphene-hBN hybrid structure with Ti/Au contacts. **(b)** Resistance versus gate voltage of monolayer graphene at $T = 1.4$ K and $T = 77$ K measured in 4-probe geometry. The inset depicts the corresponding sheet conductivities.

## 6.1 Improved transport properties of graphene on hBN

Initially, we started with a wet transfer technique for the assembly of graphene-hBN heterostructures, as described in chapter 5.2. While the mobilities were consistently higher than on SiO$_2$, there were many crucial fabrication steps that had a severe impact on graphene's quality [169, 170]. Especially reactive ion etching leaves residues on the graphene surface and limits its mobility. So we started to fabricate some hBN-graphene heterostructures without the critical etching procedure, and just put contacts on top of a stripe-like graphene flake. An exemplary device can be seen in the false-color AFM image in Fig. 6.1a. The surface of the graphene sheet is almost free of any residues and wrinkles, and indicates a good quality of the hBN-graphene hybrid structure.

This first impression from the AFM images can be confirmed by the evaluation of the back gate response in our sample. Fig. 6.1b shows the 4-probe resistance as a function of the back gate at $T = 1.4$ K and 77 K, and the inset depicts the corresponding sheet conductivities $\sigma_s$. There is virtually no difference in $\sigma_s$ between the two curves and the carrier mobility is around 190 000 cm$^2$/Vs. Thus, we cannot see any temperature dependence of the mobility, at least below 77 K. The charge neutrality point around $V_g = -2.5$ V and the narrow peak with a charge carrier inhomogeneity as low as $\delta n \approx 3 \cdot 10^{10}$ cm$^{-2}$ indicate relatively low residual doping and high sample quality.

If we keep the carrier density constant and sweep the perpendicular magnetic field, we observe clearly developed quantum Hall states in magnetotransport measurements (Fig. 6.2a). In addition to the ordinary quantum Hall states of

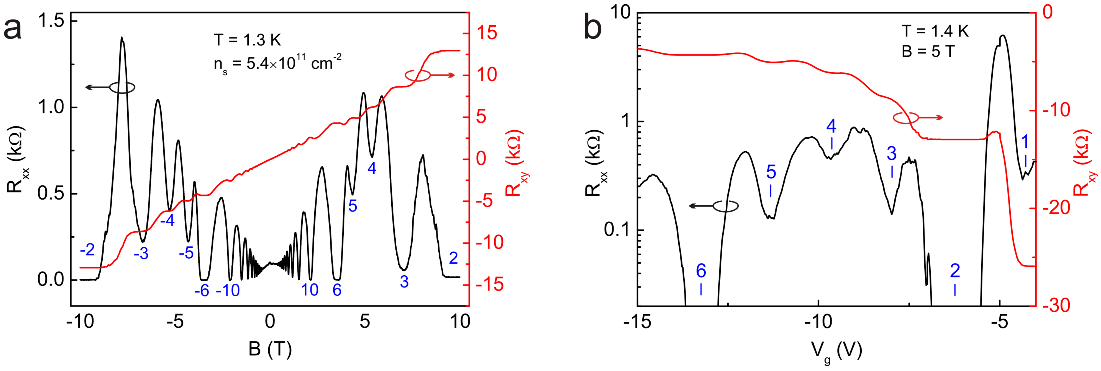

**Figure 6.2:** Quantum Hall ferromagnetism in graphene on hBN. **(a)** Magnetotransport measurement at $n_s = 5.4 \cdot 10^{11}$ cm$^{-2}$ and $T = 1.3$ K. Landau level filling factors are labeled in blue. **(b)** Magnetoresistance (black) and Hall resistance (red) versus gate voltage of the same sample. Symmetry broken quantum Hall states can be observed at $B \geq 5$ T.

monolayer graphene at filling factors $\nu = \pm 2, \pm 6, \pm 10, \ldots$, we can report minima in the longitudinal resistance $R_{xx}$ and related plateaus in the Hall resistance $R_{xy}$ that can be assigned to filling factors of $\nu = \pm 3, \pm 4, \pm 5$. So we achieve a complete symmetry breaking of the $n = \pm 1$ LL at low temperatures. The symmetry breaking of quantum Hall states starts at magnetic fields less than $B = 5$ T. At $B = 5$ T, our experiment shows pronounced dips in the magnetoresistance and plateaus in the Hall resistance corresponding to all integer filling factors between $\nu = 1$ and 6 (Fig. 6.2b).

A detailed classification of the interaction-induced IQHE states according to their real spin structure via tilted magnetic field experiments has been done by Young *et al.* [6]. They performed activation gap measurements and reported an absence of an universally dominant anisotropy in graphene quantum Hall isospin ferromagnetic states. In their experiments they observed real spin-polarized states supporting Skyrmionic excitations, charge- or spin-density order, and valley textured excitations for different filling factors [21].

## 6.2 Magnetotransport in high-mobility encapsulated graphene structures

One approach to increase sample quality and mobility even further is the encapsulation of a graphene sheet between two flakes of hBN. On the one hand, full encapsulation of graphene provides screening from any negative environmental influences, but on the other hand, there is still the requirement of producing reliable contacts to graphene. This issue has been solved by Wang *et al.* with their proposal of 1D edge contacts to an encapsulated graphene flake [98]. Em-

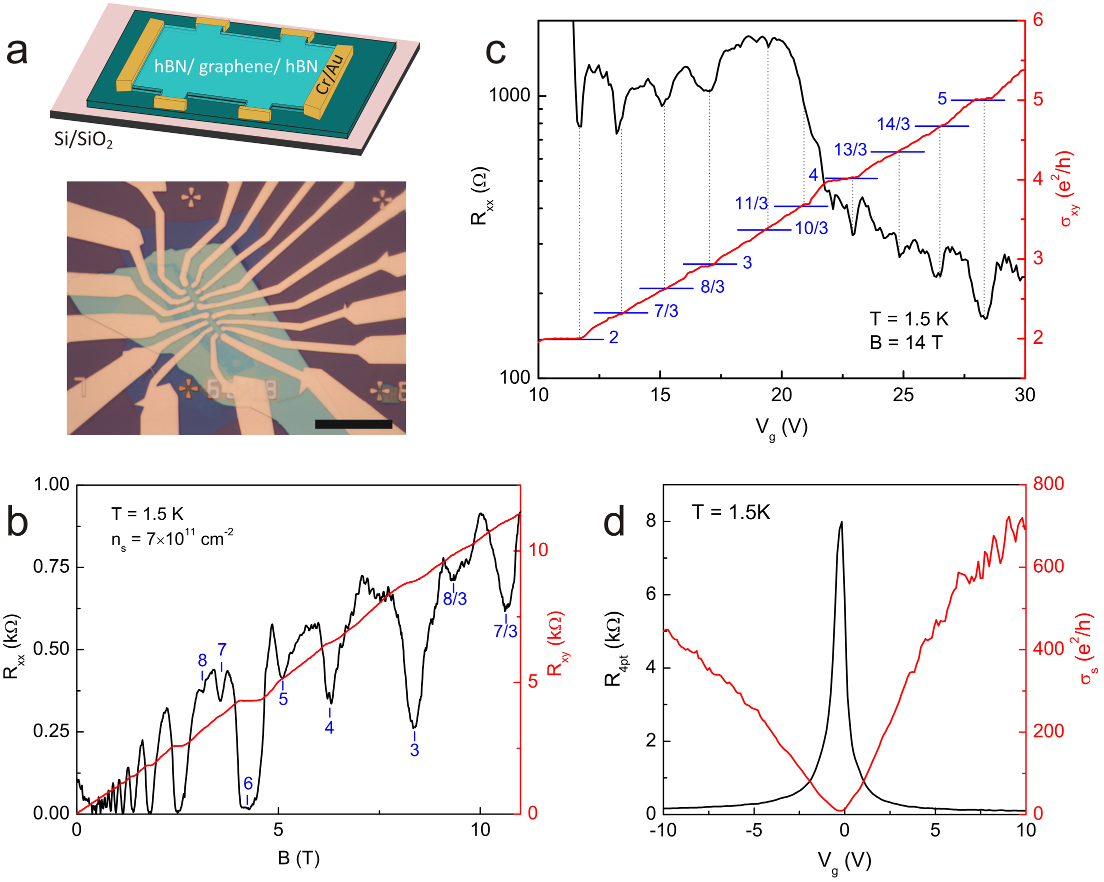

**Figure 6.3:** High-mobility encapsulated graphene structure. **(a)** Schematic and optical micrograph of an encapsulated graphene device with 1D side-contacts. Scale bar is 20 $\mu$m. **(b)** Magnetotransport experiment for $n_s = 7 \cdot 10^{11}$ cm$^{-2}$ at $T = 1.5$ K, featuring broken symmetry integer and fractional quantum Hall effect (blue). **(c)** Magnetoresistance and Hall conductivity as a function of gate voltage. Several fractional states can be observed in the $n = 1$ LL between $\nu = 2$ and 5 at $T = 1.4$ K and $B$ =14 T. **(d)** 4-point resistance $R_{4pt}$ and sheet conductivity $\sigma_s$ measured at zero magnetic field.

ploying this method, the layer assembly of the heterostructure can be completely separated from the contact metallization process and most of the residues stemming from processing can be avoided. Following this approach, we introduced a dry-transfer procedure to our lab, where we started with stacking the device and subsequently performed any further patterning steps such as lithography, reactive ion etching and metal evaporation. Figure 6.3a depicts a sketch as well as an optical micrograph of an encapsulated graphene structure with 1D edge contacts located on a Si/SiO$_2$ wafer.

Gate sweeps at low temperatures and in the absence of magnetic fields prove the exceptional quality of the encapsulated graphene device (see Fig. 6.3d). We can extract a field effect mobility of $\mu > 300\,000$ cm$^2$/Vs and a carrier inhomogeneity of $\delta n \leq 3 \cdot 10^{10}$ cm$^{-2}$ at $T = 1.4$ K. The high mobility of the sample can be confirmed with magnetotransport measurements at relatively low densities ($n_s \approx 7 \cdot 10^{11}$ cm$^{-2}$), where we get mobilities exceeding 350 000 cm$^2$/Vs (see Fig. 6.3b). In this graph, we observe pronounced interaction-induced IQHE states with full lifting of the four-fold degeneracy between $\nu = 3$ and 8, similar to the experiments discussed in the section before. But what is new in this experiment, is the development of minima in the magnetoresistance $R_{xx}$ in the $n = 1$ LL at fractional filling factors $\nu = \frac{7}{3}$ and $\frac{8}{3}$.

We report more fractional states in the $n = 1$ LL over a wide range of charge carrier density (see Fig. 6.3c). This experiment reveals further FQHE states at most multiples of $\nu = \frac{1}{3}$ between $\nu = 2$ and 5 at $T = 1.5$ K and a perpendicular magnetic field $B = 14$ T. There are pronounced dips in the longitudinal resistance $R_{xx}$ at the mentioned fractional values of the Hall conductivity $\sigma_{xy}$ in units of $e^2/h$. Besides the QHE states in the $n = 1$ LL, we could observe indications of fractional states in the $n = 0$ LL at $\nu = \frac{1}{3}$ and $\frac{2}{3}$, but these states are not fully developed and do not show exact quantization at the experimentally employed temperatures and magnetic fields.

The fractional quantum Hall effect in a 2D electron gas with multiple degrees of freedom gives the opportunity to examine the interplay between symmetry breaking and emergent topological order. However, the four-fold isospin symmetry and the unique valley anisotropies modify the FQHE in graphene and result in an unconventional sequence of fractional quantum Hall states. The observation of the FQHE in high-mobility monolayer graphene has been reported and extensively described by several groups, providing insight into the interplay between the electronic correlations and the inherent symmetries of graphene [8, 65, 9, 74]. As a consequence of the strong Coulomb interactions in graphene, the measured energy gaps in the $n = 0$ and especially in the $n = 1$ LL are up to 10 times larger than those reported in the cleanest conventional systems [8], and thus, are accessible in conventional $^4$He cryostats available in most labs. Finally, the appearance of fractional quantum Hall states at moderate temperatures and magnetic fields underlines the exceptional device quality of graphene encapsulated between hBN.

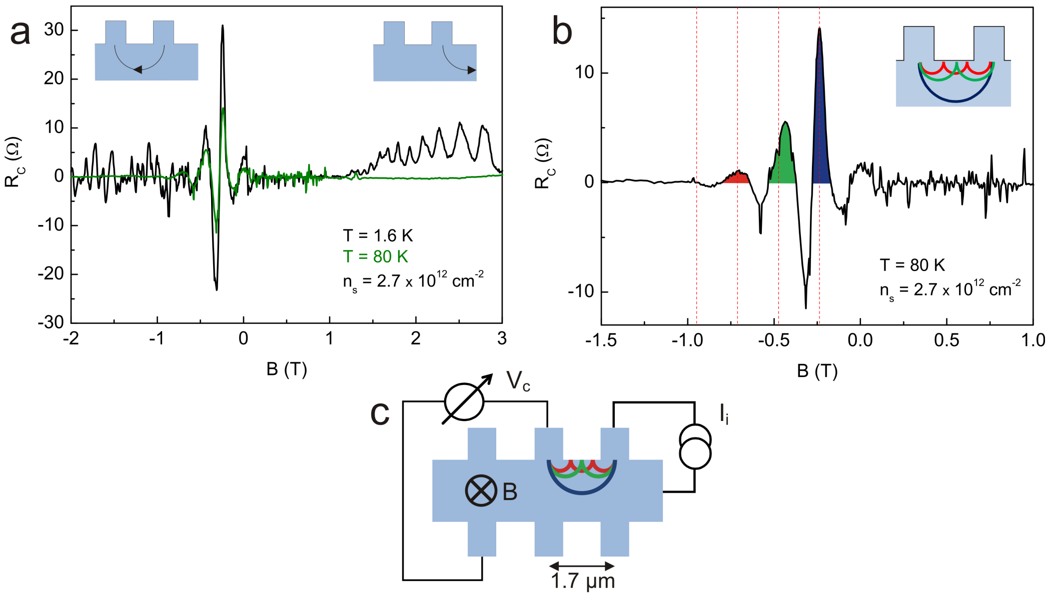

**Figure 6.4:** Transverse magnetic focusing (TMF) in graphene. **(a)** TMF spectra for $T = 1.6$ K and 80 K. For negative magnetic fields, electrons can be focused into the detector probe, resulting in peaks in the collector resistance $R_c$. For positive $B$, electrons are moving in the other direction, eventually resulting in SdHOs at higher $B$. **(b)** TMF spectrum at $T = 80$ K, where peaks can be assigned to first (blue), second (green) and third (red) modes. The vertical red lines depict the expected positions of the peaks and the top inset shows the trajectories of the corresponding modes. **(c)** Schematic of TMF experiment, showing injector and collector geometry and three different focusing modes.

Another experiment that proves ballistic transport and highlights the quality of hBN-graphene heterostructures is transverse magnetic focusing (TMF). This mesoscopic phenomenon, where a transverse magnetic field is used to focus electrons from one probe into another one, has been employed to examine the Fermi surface of semiconductor heterostructures [171], to study spin-orbit interaction [172], or to detect composite fermions [173]. Taychatanapat *et al.* performed TMF experiments in high-mobility graphene, where they continuously tuned the charge carrier density from the hole to the electron regime at temperatures up to $T = 300$ K [174].

The concept of TMF can be understood with Fig. 6.4c, where electrons are injected into the 2DEG at the injector probe and can be detected at the collector probe. In the presence of a perpendicular magnetic field $B$, electrons are constrained to cyclotron orbits with radius $R_C$, and reflections at the edge of the 2D system result in skipping orbit motion with focal points at integer multiples of the $2R_C$. Thus, the magnetic field $B_f$, needed to focus electrons at a distance $L$, can written as

$$B_f = \left(\frac{2\hbar k_F}{eL}\right) p = \left(\frac{2\hbar\sqrt{\pi n_s}}{eL}\right) p, \tag{6.1}$$

where $p-1$ is the number of reflections at the edge, $k_F$ is the Fermi momentum and $n_s$ is the carrier density [174].

We use this experimental geometry to examine TMF in high-mobility encapsulated graphene devices. Transport measurements employing this setup are depicted in Fig. 6.4a for $T = 1.6$ K and 80 K. In this graph, we plotted the resistivity of the collector $R_c$, which is the collector voltage $V_c$ normalized by the injected current $I_i = 100$ nA, as a function of the magnetic field at a carrier density of $n_s = 2.7 \cdot 10^{12}$ cm$^{-2}$. For negative magnetic fields, the charge carriers are focused by cyclotron motion from the injector probe to the collector probe (see left inset), and we observe several pronounced peaks that do not match a potential sequence of SdHOs. The peaks are decreasing as the temperature increases, potentially induced by an enhanced scattering mechanism at longitudinal acoustic phonons [49, 174]. If we reverse the direction of the perpendicular magnetic field, the direction of the cyclotron motion and its skipping orbits is reversed (see right inset), and we cannot detect a similar signal in $R_c$. However, we observe SdHOs for $B > 1.5$ T at $T = 1.6$ K, as expected in a longitudinal resistance measurement. The SdHOs are no longer present at the elevated temperature of $T = 80$ K (Fig. 6.4b), but the peaks originating from TMF into the collector probe are more robust in temperature and remain clearly visible. Whenever the injected electrons are focused into the collector probe, $V_c$ builds up, and we can assign the TMF peaks to different modes according to the formula for $B_f$, shown above. The first and most dominant peak (blue) corresponds to $p = 1$, where electrons are directly focused from the injector to the collector, whereas the subsequent peaks highlighted in green and red are reflected once and twice off the graphene edge, respectively. Here, the amplitude of each peak is lower than the last one by the probability of diffuse scattering. The vertical red lines in the graph mark the expected magnetic field position $B_f$ of the different TMF modes and are nicely matching the experimental data. Considering the carrier mobility of $\mu > 200\,000$ cm$^2$/Vs at the relevant density, we can deduce an electron mean free path of $l_{mfp} > 3.5$ $\mu$m, which is in line with the observation of TMF modes in our experiment.

## 6.3 Conclusion

All in all, we showed that our stacking procedure for hBN-graphene heterostructures is mature and consistently yields high-quality devices with considerably enhanced properties compared to graphene on Si/SiO$_2$ substrates. We examined the symmetry-broken integer as well as the fractional quantum Hall effect in our magnetotransport experiments at $T = 1.4$ K. Moreover, we observed several robust TMF peaks in our measurements on high-mobility graphene at $T = 1.6$ K and 80 K that indicate ballistic transport in the range of a few micrometers, and validate the high quality and low inhomogeneity of encapsulated hBN-graphene hybrid structures.

# CHAPTER 7

# Magnetotransport in graphene antidot lattices

Graphene nanostructures have been studied intensely over the last years and enormous experimental progress has been achieved. However, while the bulk carrier mobility in graphene was significantly improved by the introduction of graphene-hBN heterostructures, any subsequent nanopatterning procedure can add extra damage to graphene and drastically degrade its intrinsic properties.

In this chapter and reference [10][1], we show that full encapsulation of graphene by hBN protects the graphene sheet in a top-down nanofabrication scheme. We demonstrate the high sample quality by preparing graphene-based antidot lattices, which exhibit a nice realization of classical dynamics in the probed magnetoresistance. We report pronounced commensurability features stemming from ballistic orbits around one or several antidots in etched lattices with periods down to 50 nm. Unique to graphene nanostructures, the regime of very small scale modulation is accessible. This fact allows us to explore the boundary between the classical and the quantum transport regime, as the Fermi wavelength of the electrons approaches the smallest length scale of the artificial potential.

In the end, we go beyond our publication [10] and discuss related theoretical studies for ballistic transport in graphene antidot lattices and their explicit consistence with our experimental results [151, 11].

---

[1] Most of the experiments and the relevant discussion shown in sections 7.1 - 7.3 were adapted from our publication: A. Sandner *et al.*, Nano Lett. **15** (2015)

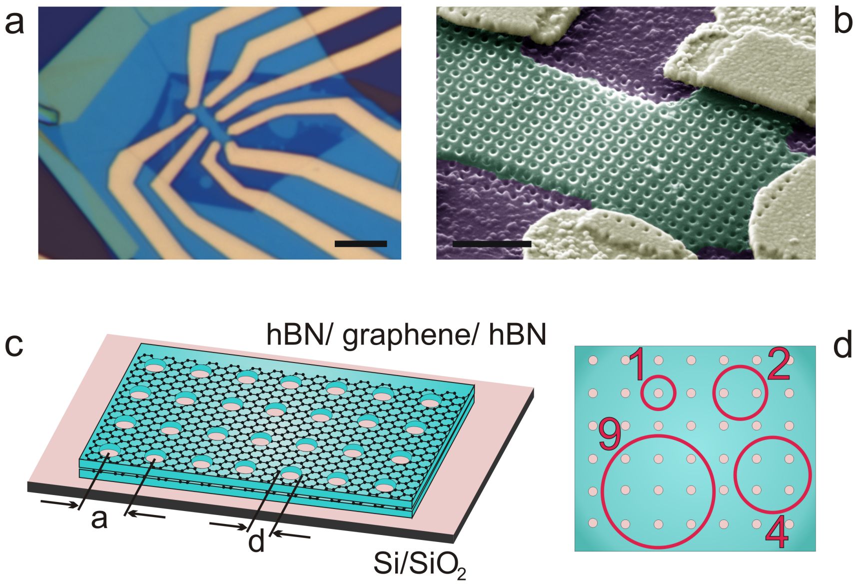

**Figure 7.1:** Graphene-hBN heterostructure with EBL-patterned antidot lattice. **(a)** Optical micrograph of a finished Hall bar structure, etched out of a hBN/graphene/hBN heterostructure and contacted with Cr/Au leads. Scale bar is 5 $\mu$m. **(b)** False-color scanning electron micrograph of a stack with imposed antidot period $a = 100$ nm. Scale bar is 500 nm. **(c)** Sketch of the antidot lattice in an encapsulated graphene structure. The lattice period $a$ ranges from 50 to 250 nm, and the antidot diameter $d$ is about $25 - 30$ nm. **(d)** The most prominent cyclotron orbits fitting into the antidot lattice.

## 7.1 Sample fabrication and architecture

As shown in the chapter before, graphene samples can have a very high carrier mobility when influences from the substrate and the environment are minimized. Employing hBN-graphene heterostructures [175] was shown to improve the carrier mobility [7], allowing the observation of ballistic transport [174, 176], the symmetry-broken integer [6] or the fractional quantum Hall effect in graphene [8]. However, nanopatterning graphene can add extra damage and drastically reduce sample mobility by edge disorder [177, 178, 179]. Preparing etched graphene nanostructures on top of a hBN substrate instead of SiO$_2$ is no remedy, as transport characteristics are still dominated by edge roughness [180]. While chemically prepared graphene nanostructures [181, 182, 183] are a potential route for certain applications, the high flexibility of a top down patterning approach is extremely desirable.

Recently, a dry stacking technique was introduced, which allows complete encapsulation of graphene into layers of hBN and excludes any contamination from process chemicals such as electron beam resist [98]. Here, we show that etching fully encapsulated graphene on the nanoscale is a convenient and gentle approach and high mobilities can be preserved.

To obtain embedded graphene samples, hBN/graphene/hBN stacks were prepared using the dry stacking technique, patterned into Hall bar shape, and contacted using Cr/Au [98]. In hBN/graphene/hBN samples prepared by this method, we routinely obtained carrier mobilities in excess of $\mu = 100\,000\ \mathrm{cm}^2/\mathrm{Vs}$, showing all integer quantum Hall states starting from a few Tesla. A few samples with mobilities of $\mu \approx 300\,000\ \mathrm{cm}^2/\mathrm{Vs}$ also showed the fractional quantum Hall effect at $T = 1.4$ K (see chapter 6). This shows that our fabrication procedure is mature and consistently yields high sample qualities. Moreover, the samples presented in this study had no imposed moiré superlattice potential [117, 113]. Subsequently, an antidot lattice was patterned using electron beam lithography and $\mathrm{CHF}_3$-based reactive ion etching.

Fig. 7.1 shows an optical micrograph of a finished sample and a false-color scanning electron micrograph of a sample after measuring. A sketch of the square antidot lattice, etched into the hBN-graphene-hBN hybrid structure, is also shown. The antidot lattice period $a$ was varied between 50 nm and 250 nm. The antidot diameter $d$ was lithographically defined to be about 40 nm, but due to the conical etching profile, the actual diameter in the graphene plane is smaller. Using SEM inspection, we estimate it to be about $25 \ldots 30$ nm.

## 7.2 Commensurability peaks in graphene antidot arrays

Antidot lattices show a beautiful realization of classical transport in mesoscopic systems. Furthermore, graphene antidot lattices can help circumventing the problem of the missing band gap in transistor applications [184, 185], and were even predicted to serve as the technological basis for spin qubits [186].

To this end, we prepared antidot lattices [14] in graphene, where we observe magnetotransport features stemming from ballistic transport. We performed experiments on graphene antidot lattices [187, 188] etched into hBN/graphene/hBN heterostructures with lattice periods going down to $a = 50$ nm. In a related work, Yagi *et al.* report on the observation of commensurability peaks in triangular antidot lattices in graphene on hBN [131]. While they used a different patterning scheme for non-encapsulated devices, and thus, their apparent mean free path was smaller, they see antidot peaks in magnetotransport experiments.

In contrast to previous work on graphene on SiC [188], we can determine and control the carrier density $n_s$ on samples with different lattice periods. Thus, we can assure unambiguously that magnetotransport on our samples shows commensurability features stemming from ballistic orbits around one or several antidots. This allows us to prove that the high carrier mobility is preserved in the nanopatterning step even though the zero field resistance is dominated by scattering on the artificial nanopattern, giving an apparent reduction of the mobility.

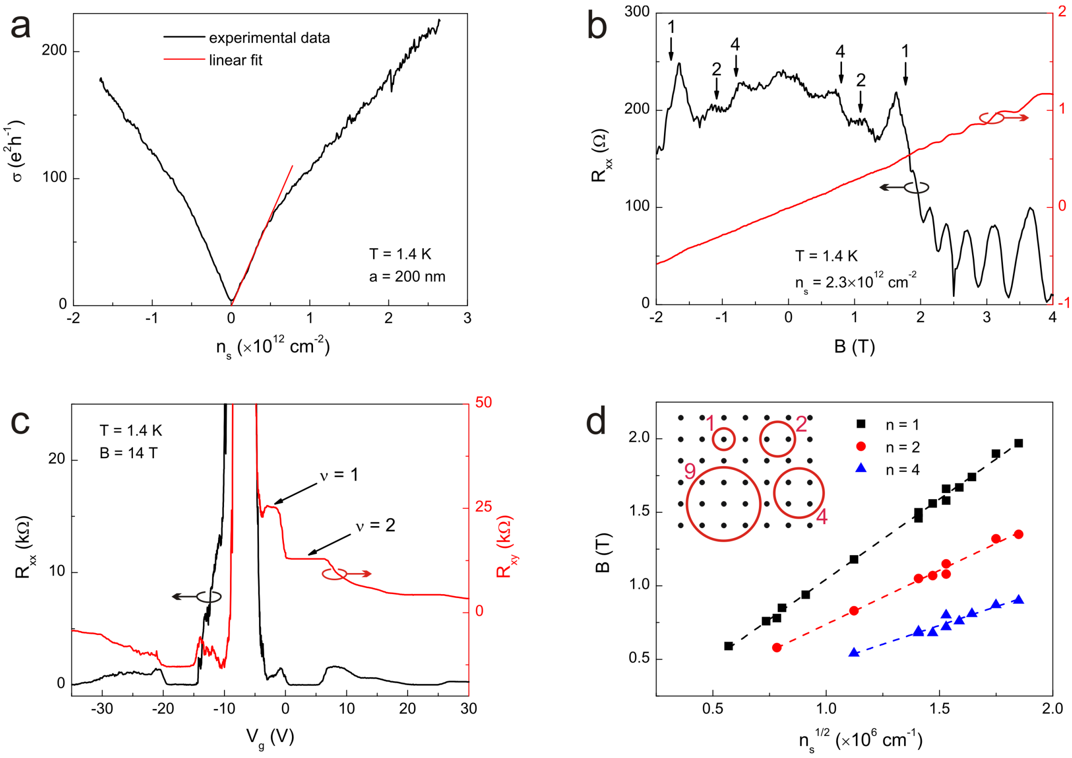

**Figure 7.2:** Transport measurements on a hBN-graphene stack with an antidot period of 200 nm. **(a)** Sheet conductivity as a function of the charge carrier density at $T = 1.4$ K. The linear fit gives an apparent mobility of 35 000 $\text{cm}^2/\text{Vs}$. **(b)** Magnetotransport experiment. The arrows correspond to the expected magnetic field positions of the orbits sketched in Fig. 7.1d. The fine structure in the magnetoresistance $R_{xx}$ is stemming from phase-coherent oscillations visible at low temperatures. **(c)** Gate dependence of $R_{xx}$ and $R_{xy}$ at $B = 14$ T, showing a pronounced $\nu = 1$ quantum Hall plateau. **(d)** Magnetic field positions of the three antidot peaks scale with the square root of the carrier density $n_s$, confirming the classical origin of those peaks.

The small feature size of our samples also allows us to approach the region where the classical picture of cyclotron orbits no longer applies. This classical to quantum crossover is governed by the ratio between the Fermi wavelength $\lambda_F$ of the carriers and the dimensions of the nanopattern.

In Fig. 7.2, we show data for a sample with a lattice period of $a = 200$ nm. From the gate response of the conductivity at a magnetic field $B = 0$, shown in Fig. 7.2a, we extract an apparent field effect mobility of $\mu = 35\,000\ \text{cm}^2/\text{Vs}$. At a carrier density $n_s = 2.3 \cdot 10^{12}\ \text{cm}^{-2}$ this corresponds to an apparent mean free path of about $l_{mfp} = \frac{\hbar}{e}\sqrt{\pi n_s}\mu = 620$ nm.

Ishizaka and Ando [189] discuss the total mean free path $l_{mfp}$ in an antidot sample with intrinsic mean free path $l_e$ and a square antidot lattice with period $a$ and antidot diameter $d$. For hard-wall antidots, they calculate the scattering cross section of a single antidot and evaluate the scattering length $l_{sc}$ due to scattering at the antidot lattice only, at $B = 0$: $l_{sc} = 3a^2/(4d)$. Using Matthiessen's rule, the total mean free path can be written as:

$$\frac{1}{l_{mfp}} = \frac{1}{l_{sc}} + \frac{1}{l_e} \tag{7.1}$$

We estimate the antidot diameter to be $d = 25 \ldots 30$ nm and obtain a scattering length $l_{sc} = 1000 \ldots 1200$ nm for the sample shown in Fig. 7.2 ($a = 200$ nm). Considering the measured total mean free path of $l_{mfp} = 620$ nm, we can deduce an intrinsic electron mean free path of $l_e = 1300 \ldots 1600$ nm in our system.

Magnetotransport traces of this device (see Fig. 7.2b) show pronounced peaks at field values where the cyclotron diameter $2R_C = \frac{2\hbar}{eB}\sqrt{\pi n_s}$ is commensurate to the square antidot lattice. The peak belonging to $2R_C = a$, the fundamental antidot peak, is most prominent. Additional peaks appearing at lower fields correspond to orbits encircling 2 and 4 antidots [14] (see Fig. 7.1d), confirming a mean free path which spans several lattice periods. While in a simple picture only the unperturbed orbits encircling the antidots are responsible for the magnetotransport features, a more detailed analysis based on the Kubo formula shows that velocity correlations in the chaotic trajectories, which occupy the largest part of the phase space, result in the magnetoresistance peaks [152, 190]. Most of the orbits therefore hit the antidot edges several times within a mean free path. Hence, the visibility of the antidot peaks not only proves a high bulk mobility, but also shows that scattering at the edges does not cut off the trajectories and we can conclude that the high carrier mobility also survives after nanopatterning.

At higher fields, the cyclotron diameter $2R_C$ is reduced below the neck width $a - d$ in between the antidots. We can observe Shubnikov-de Haas oscillations, eventually resulting in a well-defined quantum Hall effect. At $B = 14$ T we clearly observe the $\nu = 1$ plateau, which again shows the high sample quality (Fig. 7.2c). We evaluated the carrier density dependence of the magnetoresistance peaks corresponding to orbits around 1, 2 and 4 antidots (Fig. 7.2d) and found that the peaks were always well described by a square root dependence of the cyclotron diameter on the carrier density down to $n_s = 3.2 \cdot 10^{11}$ cm$^{-2}$. Quantitatively, we confirmed the formula for the cyclotron diameter for graphene given above, which contains spin and valley degeneracy.

Fig. 7.3a shows the magnetoresistance of a sample with $a = 100$ nm at a carrier density of $n_s = 2.8 \cdot 10^{12}$ cm$^{-2}$. The apparent Hall mobility at this density is about $\mu = 8\,000$ cm$^2$/Vs. Again, scattering at the antidot potential limits the apparent mobility [189], but the intrinsic mobility is higher as we clearly observe magnetoresistance peaks for $n = 1, 2, 4$ antidots. Also, the $\nu = 1$ quantum Hall state is visible in this sample, again indicating a higher intrinsic mobility. Ishizaka and Ando studied how the visibility of the higher order antidot peaks depends

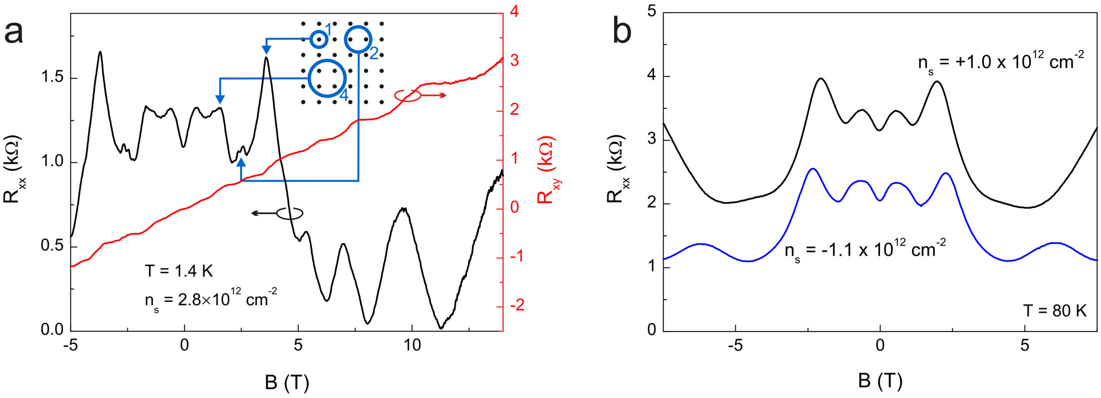

**Figure 7.3:** Magnetotransport data taken on a sample with $a = 100$ nm. **(a)** The three pronounced peaks in $R_{xx}$ correspond to electron orbits around 1,2 and 4 antidots. (b) Magnetoresistance measured at similar electron and hole density at $T = 80$ K. Both graphs are virtually identical, proving the identical potential profile for electrons and holes.

on the mobility [190]. From their data, we estimate that the intrinsic mean free path must be at least 400 nm, well in excess of the apparent mean free path of 160 nm.

The good visibility of the $n = 2$ peak confirms the small aspect ratio $d/a \leq 0.3$ [190], in agreement with our SEM analysis and also with the onset of the well-defined Shubnikov-de Haas oscillations in our magnetotransport data. All these approaches give an antidot diameter of $d = 25\ldots30$ nm.

In experiments in GaAs based antidot lattices it was found that due to depletion at the antidot boundaries, the potential can be very soft and small lattice periods are hard to realize. In our case the data compares well to hard-wall potential lattices in GaAs, which could be realized in GaAs only at much larger lattice periods [14]. We also compared data for similar carrier densities in the electron and hole regime in Fig. 7.3b and found the graphs to be virtually identical. This proves that there is no edge doping at the antidot boundaries, which would have led to different potential shapes in the electron and hole regime due to Fermi level pinning at the edges.

## 7.3 Transport characterization of the low density regime

Now let us discuss the transition between the quantum and the classical transport regime at low carrier densities. In GaAs-based heterostructures, the smallest lattice period realized so far was $a = 80$ nm, and required critical tuning of the etch depth [191]. In contrast, due to the lack of a depletion region in graphene, the fabrication of samples with a very small lattice period is less critical, and the carrier density is widely tunable. Also, due to valley degeneracy, the Fermi wavelength in graphene $\lambda_F = 2\sqrt{\frac{\pi}{n_s}}$ is a factor of $\sqrt{2}$ larger than in GaAs based 2DEGs at the same carrier density. Thus, we can explore the transition from the semi-classical to the quantum regime [192], where a description in terms of classical orbits is no longer justified. In the samples with $a \leq 100$ nm we are able to study this transition. Fig. 7.4a shows the disappearance of the main antidot peak in a sample with $a = 75$ nm as the carrier density is lowered, making $\lambda_F$ longer. We find that this peak is only visible at densities above $n_s = 4.3 \cdot 10^{11}$ cm$^{-2}$, corresponding to $\lambda_F = 54$ nm. Also, in two samples with $a = 100$ nm, we observe that the main antidot peak becomes visible for densities larger than $n_s = 2.2 \times 10^{11}$ cm$^{-2}$, which corresponds to $\lambda_F = 75$ nm. In a sample with $a = 50$ nm, we observed a weak antidot peak only at $n_s = 2.5 \times 10^{12}$ cm$^{-2}$ ($\lambda_F = 22$ nm). To be in the classical limit of a quantum system, the Fermi wavelength must satisfy a condition $\frac{\lambda_F}{2\pi} \ll l$ [193], where $l$ is a typical dimension of the system. In our case, the neck width $a - d$ of the constriction between the antidots is the shortest length scale in the problem, and we find that when $\lambda_F \approx a - d$ the classical regime sets in and the antidot peak becomes visible.

The fact that the antidot peaks disappear at low densities can not be attributed to a relative increase of disorder such as deviation of the position and diameter of the antidots in our system, since we see well defined features without any deviation at higher densities. The suppression of the commensurability peaks can be either due to a limited mean free path or the breakdown of the classical picture. In Fig. 7.2d (lattice period $a = 200$ nm) all the antidot peaks disappear at roughly the same magnetic field, $B \approx 0.5$ T (where $\mu B$ exceeds some constant), but different carrier density. This behavior is clearly governed by a limited mean free path. In contrast, in the sample of Fig. 7.4a ($a = 75$ nm), we find that the classical features at both $B \approx 1$ T and $B \approx 2.5$ T disappear at the same carrier densities, making a $\lambda_F$-driven scenario more realistic.

Finally, at low densities, we can observe a weak localization (WL) feature at low temperatures: a peak in the magnetoresistance at $B = 0$ (see Fig. 7.4b). Using a standard analysis for WL in graphene [194] that we employed in earlier work on graphene antidot lattices on SiO$_2$ [187], we extracted the phase coherence length $L_\phi$. For the sample with $a = 100$ nm (same as in Fig. 7.3a) we found it

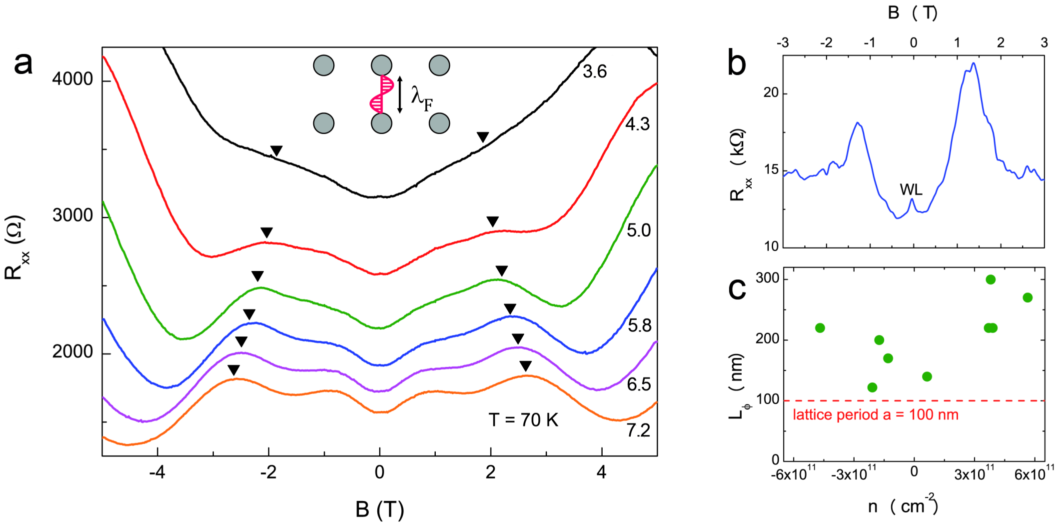

**Figure 7.4:** Transition between classical and quantum regime at low densities. **(a)** $R_{xx}$ data of a device with $a = 75$ nm at very low densities, at the transition into the regime of classical transport. The densities are given in units of $10^{11}$ cm$^{-2}$, shown next to the corresponding graphs. The expected position of the fundamental antidot peak is marked with a triangle for each density. As the carrier density is decreased, the antidot peaks disappear. Inset: Sketch of the Fermi wavelength corresponding to $n_s = 4.3 \cdot 10^{11}$ cm$^{-2}$. **(b)** Weak localization (WL) peak in a sample with $a = 100$ nm, taken at $n_s = 1.3 \cdot 10^{11}$ cm$^{-2}$. There is no commensurability peak visible. **(c)** Phase coherence length $L_\phi$ extracted from the WL fits of a sample with $a = 100$ nm at different low densities and $T = 1.4$ K. The phase coherence length exceeds the lattice period, indicating that the etched boundaries do not induce severe phase-breaking.

to be between 120 nm and 300 nm (see Fig. 7.4c). It clearly exceeds the lattice period, unlike in graphene antidot samples on SiO$_2$ where $L_\phi$ was significantly below $a$ [187]. We therefore again conclude that nanopatterning of embedded graphene leads to greatly reduced scattering at the sample edges.

## 7.4 Discussion of related simulations for graphene antidot lattices

The experimental observations in graphene antidot lattices, discussed in the sections before, were reproduced with two different theoretical approaches by Power *et al.* [11] and Datseris *et al.* [195], exhibiting a striking agreement with our results.

Power and coworkers performed large-scale quantum mechanical transport simulations of graphene antidot devices, employing a fully atomistic approach, and explain the mechanisms standing behind the commensurability features [11].

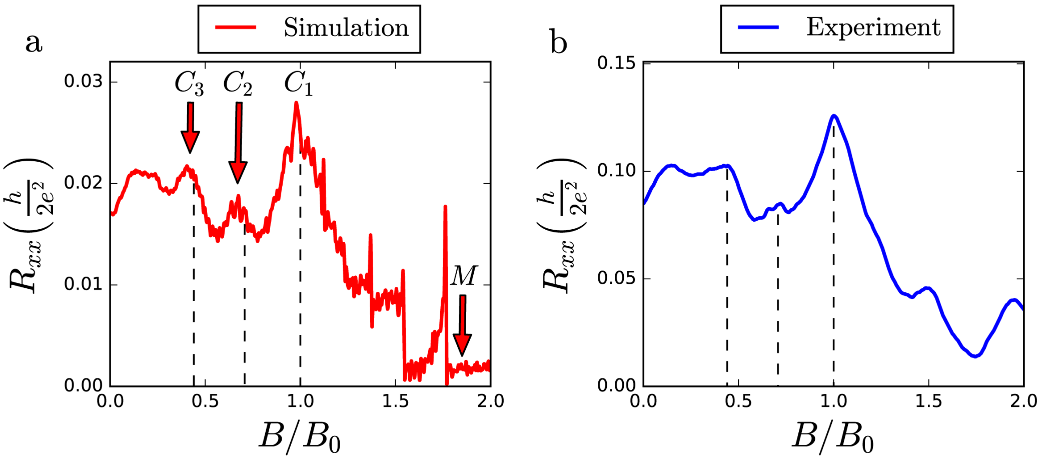

**Figure 7.5:** Comparison of our experiment with a simulation by Power *et al.* **(a)** $R_{xx}$ versus magnetic field $B$, normalized by the magnetic field position of the fundamental peak $B_0$, from a Hall bar simulation for a size-reduced graphene antidot system with antidot diameter $d \approx 10$ nm and separation $a \approx 26$ nm at $\lambda_F \approx 3$ nm $< a, d$. The three modified commensurability peaks ($C_{1,2,3}$) and the modified quantum Hall regime (M) are marked with red arrows. **(b)** Our experimental results for a lattice period of $d = 100$ nm, similar to the data shown in Fig. 7.3a. An excellent match of both graphs can be noted. Fig. adapted from [11].

Therefore they considered a six probe Hall bar structure, built by a 100 nm wide graphene zigzag nanoribbon and six external leads consisting of semi-infinite graphene nanoribbons. The reduced size, compared to our experiment, is also reflected in the smaller lattice period of $a \approx 26$ nm and an antidot diameter of $d = 10$ nm, and is necessary to conduct the simulations ($\approx 750\,000 - 950\,000$ atoms). In this way, they could map the longitudinal and the Hall resistances in the composed multi-terminal Hall bar system. A transport simulation with an exceptional agreement of the commensurability peak positions ($C_{1,2,3}$), as well as their relative magnitudes with our experimental results (same data as shown in Fig. 7.3a) is depicted in Fig. 7.5.

By examining the local current flow in the system, they are able to explain the appearance and the mechanisms behind the commensurability peaks in the magnetoresistance. On the one hand, the two highest field peaks around n = 1 and 2 antidots are induced by scattering between localized states around individual antidots, following a generalized picture of skipping orbits. On the other hand, higher order peaks can be understood with the migration between quasi-pinned orbits around groups of antidots, where scattering at neighboring antidots plays an important role.

Datseris *et al.* follow a different approach, establishing a classical transport theory of chaotic trajectories in the present antidot lattice [195]. They numer-

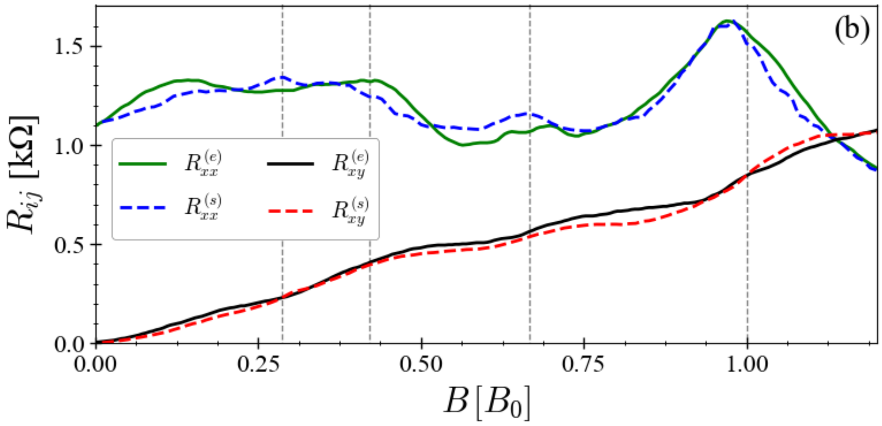

**Figure 7.6:** Comparison of resistance simulations $R^{(s)}$ by Datseris *et al.* with our experimental results $R^{(e)}$ for a graphene antidot lattice with $a = 100$ nm (same data as plotted in Fig. 7.3a). There is a striking agreement of simulation and experiment, featuring distinct commensurability peaks. $B_0 = 3.7$ T. Fig. adapted from [195].

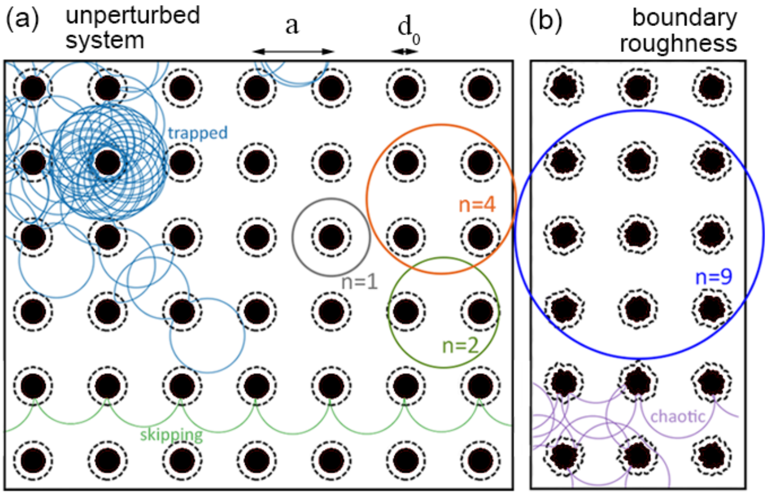

**Figure 7.7:** Potential contour plot of an antidot system with different kinds of orbits. **(a)** Unperturbed system and **(b)** antidot system with boundary roughness. Black (antidots) being a potential $U \geq 1$ and dashed lines being $U = 0$. Numerically integrated orbits (chaotic, skipping, trapped) for $B = B_0$ and pinned orbits for commensurate fields are sketched in the antidot lattice. Fig. adapted from [195].

ically reproduced our experiment with $a = 100$ nm (depicted in Fig. 7.3a), using suitable quasi-classical electron dynamics. The authors report a striking agreement of their calculations with our experimental data, featuring surprisingly robust commensurability peaks at low magnetic fields (see Fig. 7.6). These magnetoresistance simulations are using the employed experimental geometry, a rather smooth antidot potential ($c = 0.2$) and a short impurity scattering time $\tau_i = 2.5$. Fig. 7.7 shows a potential contour plot for an unperturbed antidot system and a system with boundary roughness. Different trajectories are sketched in this graph, corresponding to pinned orbits around a certain number of antidots, skipping orbits and trapped, chaotic orbits. Datseris and coworkers found that details of the exact potential shape along with possible boundary roughness do not play an important role for formation of the antidot peaks.

Moreover, chaotic dynamics and nonlinear resonances in the phase space are accounted for the formation of distinct antidot peaks, although the mean free time due to impurity scattering is short compared to the fastest time-scales of the chaotic dynamics. The distinguished robustness of the antidot features can be explained in terms of a reduced collision time, induced by nonlinear resonances in the chaotic phase space [195].

## 7.5 Conclusion

In summary, we prepared antidot lattices in stacks of hBN/graphene/hBN and observed well-developed commensurability features in samples with lattice periods from $a = 50$ nm to 250 nm. This proves that the etching procedure preserves the high sample quality. In the short-period graphene samples, we could observe the disappearance of classical features when the Fermi wavelength $\lambda_F$ exceeds $a - d$, marking a classical to quantum transition. Moreover, our experimental results were nicely reproduced by two different theories by Datseris *et al.* and Power *et al.*, employing a quasi-classical [195] and a fully atomistic approach [11], respectively.

Our experiments pave the way for well-controlled, high-quality nanodevices for the investigation of novel phenomena in graphene. For example, the recursive Hofstadter spectrum and magnetic band gap closing were predicted for triangular antidot lattices in graphene [196, 197] and are experimentally accessible, now.

# CHAPTER 8

# Interplay between moiré and antidot superlattice potentials

Antidot lattices exhibit a beautiful realization of classical transport in mesoscopic systems, where commensurability features arise from the correspondence between nano-patterned feature size and electron cyclotron orbits [11]. Recent progress in fabrication procedures allowed the observation of pronounced commensurability peaks in hBN-graphene antidot lattices [10, 131].

However, graphene coupled to hBN exhibits a rotation-dependent moiré pattern, acting as a lateral superlattice structure with unusual electronic dispersion and high electron mobility in highly-aligned hBN-graphene van der Waals heterostructures. The electronic spectrum in these hybrid structures can be explored by tuning the carrier density, approaching moiré miniband edges and saddle-point van Hove singularities (VHSs) [198, 199].

In this chapter, we study the interplay between a moiré and an imposed antidot superlattice potential and their influence on magnetotransport experiments. We characterized several highly-aligned moiré superlattices prior to the antidot patterning and compare the results to measurements achieved for the same stacks after the antidot etching procedure. We observe a gradual suppression of the classical commensurability features by approaching the satellite Dirac points of the moiré potential. There is a breakdown of cyclotron motion near the VHSs and we do not see a recurrence of the commensurability peaks at even higher densities, beyond the singularities. Moreover, the classical features in our experiments are considerably superposed with $1/B$-periodic oscillations, a phenomenon which has not been reported for antidot lattices in graphene or conventional 2DEGs.

## 8.1 Design and device preparation

Employing fully encapsulated graphene was shown to improve the carrier mobility [98], and subsequent nanopatterning steps in a top-down fabrication scheme do not drastically degrade the sample quality (see chapter 7). Moreover, etching encapsulated graphene on the nanoscale is a convenient and gentle approach where high mobilities can be preserved [10]. For the assembly of our hBN-graphene heterostructures we used a dry transfer technique inspired by Dean *et al.* and Wang *et al.* [7, 98] (see section 5.2 for more details). Since we wanted to prepare hBN-graphene heterostructures with imposed moiré superlattice [111, 115, 117], an adequate choice of exfoliated flakes and an appropriate alignment of the different crystals during the stacking procedure was indispensable. In order to succeed, we used hBN and graphene flakes with straight edges and aligned them with respect to each other, guessing they were following crystallographic edges. Next, the assembled stacks were patterned into Hall bar shape and contacted with 1D Cr/Au side contacts. For the confirmation of an imposed moiré potential, we conducted preliminary transport experiments and excluded all stacks without superlattice. All the other structures were patterned with an additional antidot array, using EBL and RIE [10]. This fabrication sequence could be justified by the relatively low yield of stacked heterostructures featuring a distinct moiré potential. All in all, we prepared four samples with moiré and antidot lattices and examined the interplay between both superlattice potentials in magnetotransport experiments.

Fig. 8.1a depicts a sketch of the device layout, featuring a moiré as well as an antidot superlattice, and Fig. 8.1b shows an optical micrograph of a finished sample, etched into Hall bar geometry and contacted with Cr/Au leads. The antidot lattice period $a$ in our experiments was varied between 60 nm and 250 nm and the diameter $d$ could be estimated to be about $25 \ldots 30$ nm.

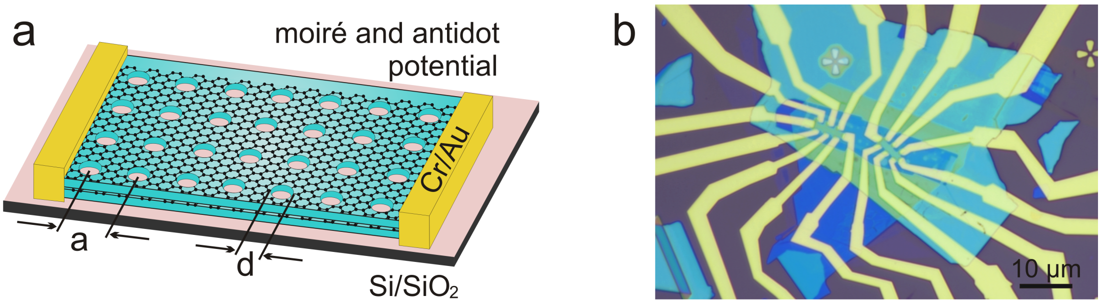

**Figure 8.1:** Device geometry of a sample with moiré and antidot superlattice. **(a)** Sketch of the sample layout with etched antidot array in a hBN-graphene-hBN heterostructure with moiré potential. **(b)** Optical micrograph of such a finished hBN-graphene-hBN hybrid structure with Cr/Au metallization.

## 8.2 Transport measurements on graphene with moiré and antidot potential

Lateral periodic superlattices were shown to generate a quantized energy spectrum consisting of discrete bands. The lateral potential induces a Landau band dispersion over a reduced Brillouin zone and interesting transport phenomena can be experimentally observed. Artificial superlattice structures, subjected to a magnetic field, have been studied intensively in semiconductor heterostructures [13, 14] and recently in graphene [10, 131]. These experiments revealed pronounced commensurability features arising from the interplay of the magnetic miniband structure and the periodic superlattice potential.

However, graphene-hBN heterostructures give the possibility for another, well-defined and periodic superlattice potential. Primarily, hBN has been used as a supporting substrate for high-mobility graphene structures [7], but scanning tunneling experiments on highly-aligned hybrid structures suggested the formation of a superlattice structure [97, 200]. The periodic potential, imposed to the electrons in graphene, is generated by the hexagonal moiré pattern resulting from incommensurability and misalignment of both crystals [199, 198, 118]. Several groups conducted magnetotransport measurements, employing moiré superlattice potentials in graphene heterostructures [117, 113, 115] and experimentally approached the Hofstadter butterfly [122]. In 1976 Douglas Hofstadter theoretically considered electrons, subjected to a periodic electrostatic potential as well as a quantizing magnetic field, and his calculations led to a self-similar recursive spectrum, known as the Hofstadter butterfly (see section 3.3).

Here, we want to discuss the interplay between an artificially patterned, rectangular antidot potential and a hexagonal moiré superlattice structure and report their influence on transport properties in graphene. Since the potential periodicity of the moiré ($\lambda \approx 12 \ldots 14$ nm) and the antidot lattice ($a = 60 \ldots 250$ nm) differ significantly, we expect commensurability features that can be assigned to one of both potentials. All heterostructures were probed in a $^4$He cryostat at low temperatures, employing a standard Lock-in setup at low frequencies.

### 8.2.1 Characterization before the antidot etching

Before the patterning procedure of the antidots, we performed a preliminary analysis of the transport properties of the assembled stacks. An easy and convenient way to assure an imposed moiré potential is conducting a back gate sweep. By tuning the carrier density one can move through the superlattice spectrum and approach additional satellite Dirac points in the case of a sufficiently large moiré wavelength $\lambda$.

Fig. 8.2 shows the low-temperature gate response of one of our highly-aligned hBN-graphene-hBN heterostructure and a candidate scenario for a corresponding

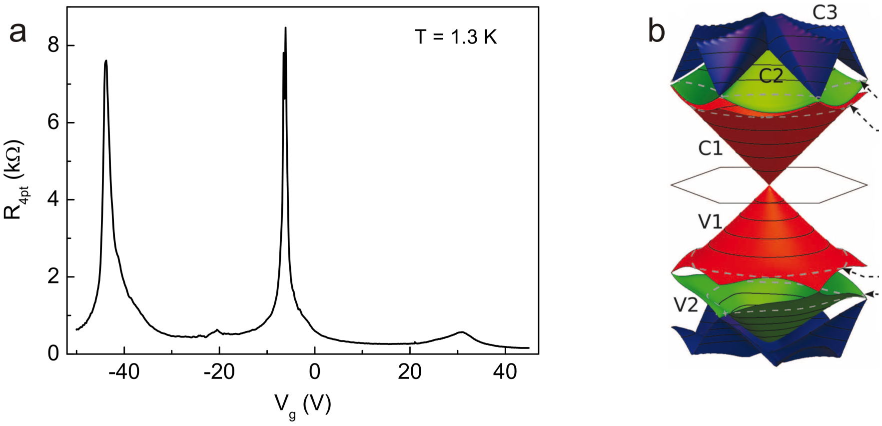

**Figure 8.2:** Device characterization of a graphene moiré superlattice. **(a)** Gate response of the longitudinal resistivity $R_{4pt}$ with the main and secondary Dirac peaks for a moiré superlattice in graphene at $T = 1.3$ K. We calculate a rotation angle of $\phi < 1°$ between the hBN and graphene lattice. **(b)** Miniband structure of a graphene-hBN superlattice, as calculated in [198, 199]. Equipotential contours are shown and the dashed contours are the energy levels of saddle-point VHSs. Fig. (b) adapted from [199].

miniband structure [198], adapted from reference [199]. In this sketch relevant minibands in the conduction and valence band are labeled and equipotential contours are shown. The satellite peaks in the gate sweep are consistent with a decrease in the density of states at the superlattice Brillouin zone band edge [113, 111]. Assuming a filled band model, where one miniband contains four electrons per unit cell (two-fold spin and valley degeneracy), we can deduce the moiré wavelength $\lambda$ and the rotation angle $\phi$ between the graphene and the hBN crystal from the gate sweep experiment (see equation 3.5). Using this assumption, we extract $\lambda = 13.7$ nm and $\phi < 1°$ for our sample.

The evolution of the magnetoresistance $R_{4pt}$ as a function of the magnetic field $B$ and the back gate voltage $V_g$ is plotted in Fig. 8.3. Here, Fig. 8.3a is depicting the experiment for the moiré superlattice before patterning of the antidots. In a conventional graphene quantum Hall system the Landau fan originates from the Dirac point and follows straight lines, tracking minima in the longitudinal resistance and plateaus in the Hall resistance [113]. This behavior can be observed in our experiments, too. However, the imposed moiré potential induces secondary Dirac points ($n_s = \pm n_0$, where $n_0 = 4/A$ corresponds to 4 charge carriers per moiré unit cell) and secondary Landau fans emerge. Intersections of the Landau levels result in third-generation neutrality points at finite fields [115, 201].
Several groups have intensively studied magnetotransport traces in moiré superlattices at high fields [117, 115, 113] and reported a series of additional, anomalous QHE states besides the usual sequence. The anomalous quantum Hall features were precisely characterized and associated to spectral gaps in the fractal

Hofstadter-like spectrum.

### 8.2.2 Characterization after the antidot patterning

Fig. 8.3b shows the corresponding color plot of the magnetoresistance $R_{4pt}$ for the same sample after etching of the antidot lattice ($a = 100$ nm). Both graphs look very similar and the Landau fans, originating from the main and secondary Dirac points, are clearly visible. The main difference, resulting from the etching procedure of the antidots, is the blurring of the quantum Hall features. For comparability, both plots use the same scaling for $R_{4pt}$. The etched voids in the graphene plane are acting as additional scatterers and the longitudinal resistance is increased. However, the used scaling and the interpolation procedure does not allow us to report any indications for commensurability features arising from the antidot lattice.

Hence, we want to focus on selected magnetotransport traces and discuss the influence of the moiré as well as the antidot superlattice potential on the transport properties in our experiment. Fig. 8.4a compares magnetoresistance traces of a device with moiré potential and one without for a similar carrier density of $n_s = 2.0 \cdot 10^{12}$ cm$^{-2}$. Both samples were patterned with a rectangular antidot array with $a = 100$ nm. The blue curve for the device without moiré superlattice shows distinct commensurability features and we can assign the antidot peaks to electron orbits around $n = 1, 2$ and 4 antidots. At higher fields, where the cyclotron diameter $2R_C = \frac{2\hbar}{eB}\sqrt{\pi n_s}$ is reduced below the neck width $a - d$ in between the antidots, we observe pronounced quantum Hall features [10]. However, things seem to be different for the sample with moiré potential (black curve). We can still identify a maximum in $R_{xx}$ that we can attribute to $n = 1$ and probably there is a weak one for $n = 4$ at lower fields. But obviously, the commensurability peaks are superposed with additional $1/B$-periodic oscillations. An analysis of the periodicity and the density-dependence of these oscillations suggests emerging Shubnikov-de Haas oscillations (see appendix C for details). Most likely, SdHOs are present down to low fields and superposed to the semiclassical features.

The same observation can be made in Fig. 8.4b, where low temperature magnetotransport experiments for a sample with antidot and moiré potential are depicted. For the relatively low density related to a back gate voltage of $V_g = +10$ V, we see a pronounced fundamental antidot peak for $2R_C = a$ and a set of weak SdHOs at fields even below the peak. Similarly, there are commensurability peaks for $n = 1$ and 4 in the measurement with $V_g = +25$ V (see arrows marking the expected field positions). However, the additional oscillations are more prominent and considerably covering the semiclassical features. We recognize a distinct density-dependence of the $1/B$-periodic oscillations in this graph, making a Brown-Zak-type (BZ) origin unlikely [202, 203]. BZ oscillations feature a $1/B$-periodicity independent of the carrier density $n_s$ and emerge most profoundly at high $T$ [201]. The minima in the magnetoresistance $R_{xx}$ can

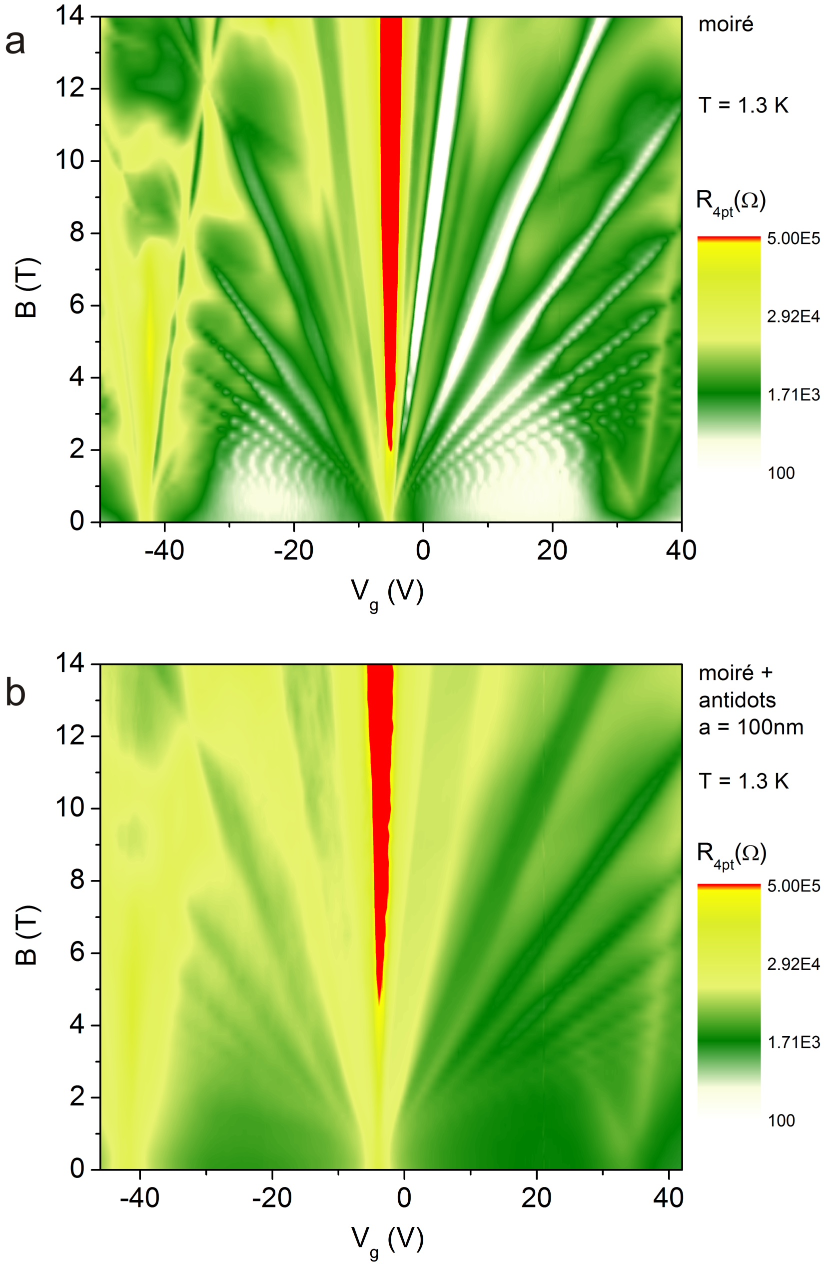

**Figure 8.3:** Color plot of the magnetoresistance $R_{4pt}$ as a function of magnetic field $B$ and gate voltage $V_g$ for a graphene moiré superlattice before and after antidot patterning. **(a)** Experiment before antidot etching. Scaling from white to red; gaps appear as white/bright lines. We observe the fractal spectrum with the main Landau fan in the middle and two additional ones originating from the satellite Dirac points. **(b)** Similar experiment on the same device after patterning of a rectangular antidot array with lattice constant $a = 100$ nm. The color plot is blurred compared to the one without antidots, but we can still identify the different Landau fans. For comparability, we used the same scaling for $R_{4pt}$ in both graphs.

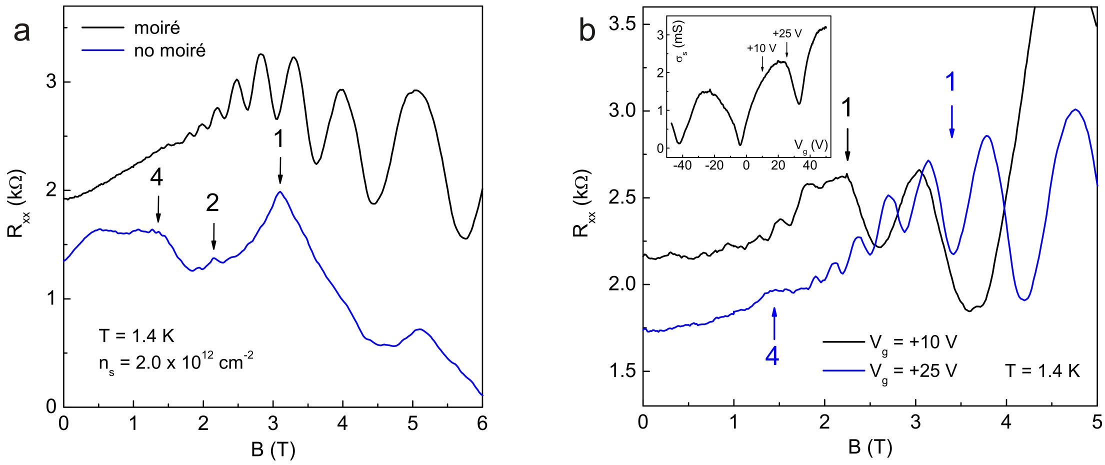

**Figure 8.4:** Magnetotransport experiments in graphene with moiré and antidot superlattice potentials. **(a)** Magnetoresistance traces of one device with moiré superlattice and one without. Both samples were patterned with a rectangular antidot lattice with $a = 100$ nm. The experiments were performed with the same carrier density of $n_s \approx 2.0 \cdot 10^{12}$ cm$^{-2}$ at $T = 1.4$ K. The arrows mark the expected magnetic field positions for the different commensurability peaks. We observe a strict separation between the classical and the quantum Hall regime for the sample without moiré potential, but with moiré, we see SdHOs superposed to the classical features. **(b)** Magnetotransport experiment for a sample with moiré and antidot potential ($a = 100$ nm). As we increase the carrier density and approach the satellite Dirac points, the superposition of the quantum Hall regime on the classical features increases. For $V_g = +10$ V, we observe a pronounced fundamental antidot peak, but for $V_g = +25$ V, the SdHOs are more prominent and covering the antidot peaks. The inset of the graph depicts the sheet conductivity $\sigma_s$ versus gate voltage $V_g$, and the arrows are marking the densities shown in the graph.

be found at $\phi/\phi_0 = p/q$, indicating the same periodicity as the Hofstadter butterfly spectrum. Nevertheless, BZ oscillations are a phenomenon independent of the spectral gaps of the Hofstadter butterfly and induced by the formation of BZ minibands for several unit fractions of $\phi_0$ [201]. In this way, the Hofstadter spectrum can be regarded as a collection of Landau levels that originate from numerous BZ minibands in an effective magnetic field $B_{eff} = B - \phi_0(p/q)/A$ ($A$ being the area of the moiré superlattice unit cell) [112, 113].

There is a clear relation between the charge carrier density in our system and the magnitude of the Shubnikov-de Haas oscillations, superposed to the commensurability features. As we increase the carrier density and approach the satellite Dirac points, the superposition of the quantum Hall regime on the classical features increases. The inset of Fig. 8.4b illustrates the sheet conductivity $\sigma_s$ versus gate voltage $V_g$, and the arrows clarify the probed densities with respect to the secondary Dirac points.

A prominent superposition of the antidot features with SdHOs has been reported neither in conventional 2DEGs [14] nor in graphene [10, 131]. All experiments demonstrated a separation between the classical "antidot regime" at low fields and a distinct quantum Hall regime, featuring SdHOs at higher fields. Since we observe the mixing of both regimes in several samples with moiré and antidot potentials, we can exclude fabrication issues such as insufficient etching depth of the antidots, etc. We assign this phenomenon to the presence of a moiré superlattice and its interplay with the antidot potential.

A related experiment on a different graphene moiré superlattice with etched antidots ($a = 250$ nm) can be seen in Fig. 8.5. It features measurements obtained at various carrier densities, approaching one of the secondary Dirac points. Fig. 8.5e shows the sheet conductivity $\sigma_s$ versus gate voltage $V_g$ with minima at the main and the secondary Dirac points. Here, the carrier densities corresponding to the graphs (a)-(d) are marked with color-coded arrows. Similar to before, the experiments with $V_g = +15$ V and +20 V demonstrate a pronounced antidot peak, superposed with Shubnikov-de Haas oscillations. However, the commensurability peak is severely suppressed in the measurements for $V_g = +25$ V and +30 V, in the vicinity of the satellite Dirac point. The black arrows mark the calculated $B$-field position of the fundamental antidot feature, but we cannot report any features besides SdHOs for these gate voltages. Though, the features related to the moiré superlattice, such as $R_{xx}$ minima emanating from the main and secondary Landau fans and strong magnetoresistance around zero field, remain prominent. Fig. 8.6 shows these characteristics in more detail, where the blue curve is from a device with moiré and antidot potential (same as depicted in Fig. 8.5d), and the black curve stems from a sample with similar moiré wavelength $\lambda \approx 14$ nm, but without antidots. There is a striking conformity of both curves, highlighting the dominance of moiré features in the experiment.

We explain the suppression of the classical antidot features in our experiments by an orbital switching of the cyclotron motion near van Hove singularities (VHSs), bearing some resemblance to a magnetic breakdown [204, 205]. Lee *et al.* reported a similar observation in transverse magnetic focusing (TMF) experiments on graphene moiré superlattices [199], where the classical TMF oscillations abruptly terminated at densities around saddle-point VHSs. Fig. 8.2b shows a simulated moiré bandstructure, as calculated in reference [198]. The dashed contours, marked with arrows, are depicting the energy levels of the VHSs, where the miniband dispersion percolates across all repeated Brillouin minizones [199]. At these saddle points near the edges of minibands, electrons do not run on circular orbits, but follow "run-away" trajectories. In this way, we cannot observe commensurability features arising from the antidot lattice around the satellite Dirac points.

However, in contrast to the TMF experiment by Lee and coworkers, the classical features in our measurements do not recur at higher densities beyond the VHSs. We performed experiments with gate voltages up to $V_g = \pm 90$ V for one

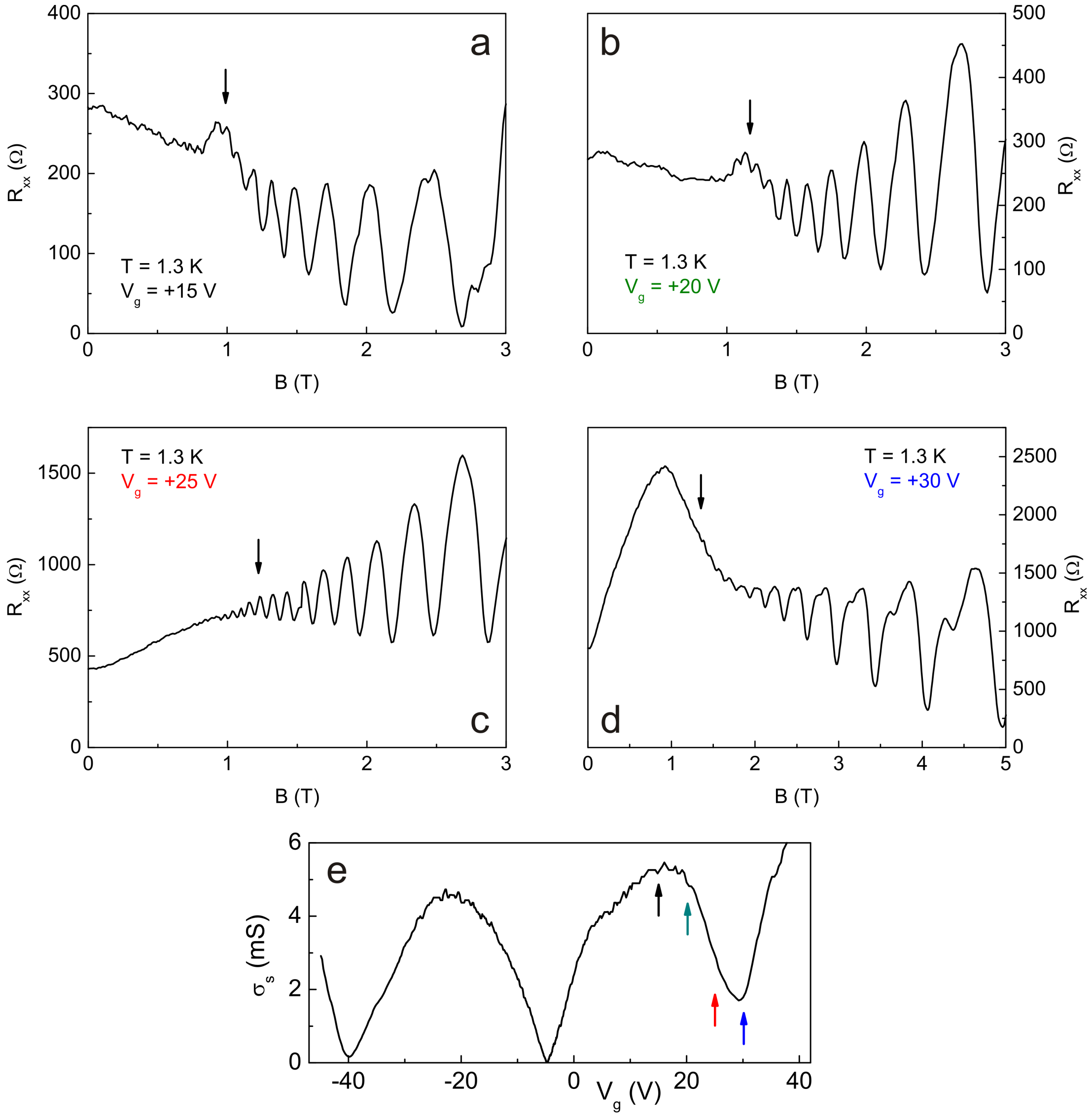

**Figure 8.5:** Commensurability peaks in a moiré superlattice with an antidot periodicity of $a = 250$ nm. Magnetotransport traces of the graphene device for different back gate voltages with arrows marking the expected positions of the antidot peaks. We observe a pronounced fundamental antidot peak for $V_g = +15$ V **(a)** and +20 V **(b)**, partially superposed with SdHOs. **(c)+(d)** For higher gate voltages, approaching the satellite Dirac point, the commensurability features vanish and only the SdHOs from the main and the secondary Dirac peaks survive. **(e)** Sheet conductivity $\sigma_s$ versus gate voltage $V_g$ with minima at the main and the secondary Dirac points, depicting the examined densities with color-coded arrows.

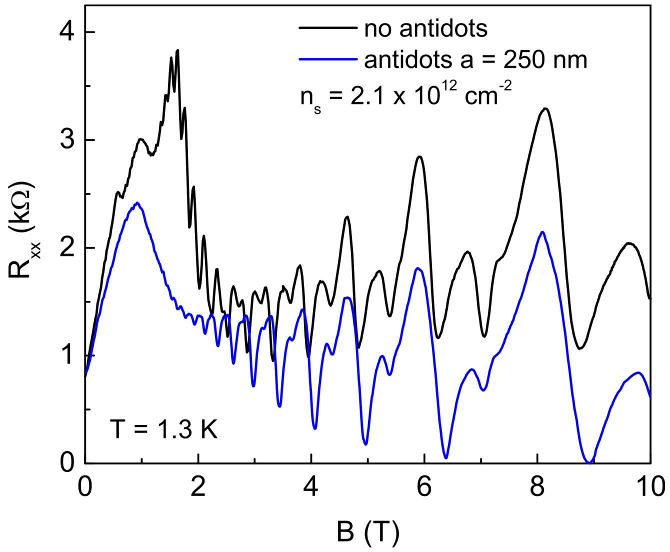

**Figure 8.6:** Magnetotransport traces in the vicinity of the extra DP. Comparison of an experiment with etched antidot lattice an one without for the same density. Both stacks had a moiré wavelength of $\lambda \approx 14$ nm. The strong magnetoresistance at low fields is characteristic for the moiré potential, not the antidots.

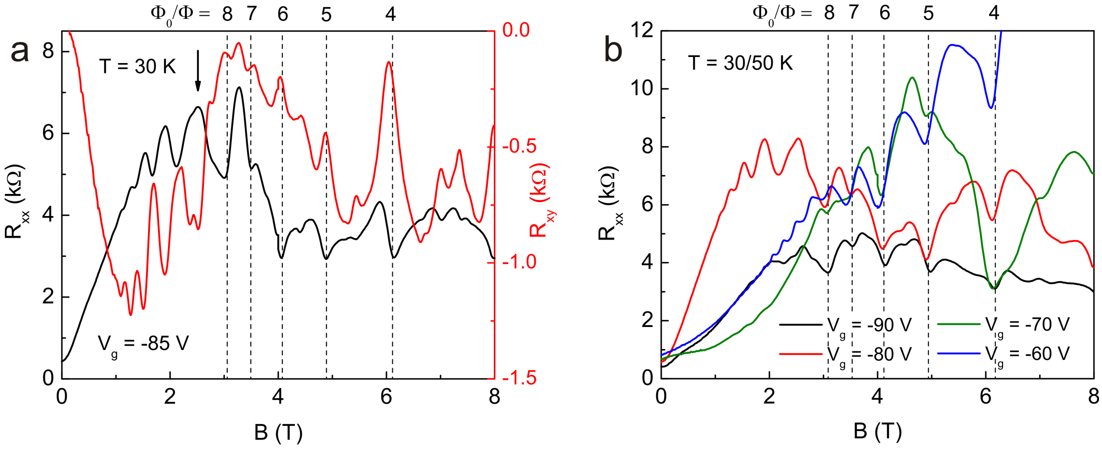

**Figure 8.7:** Magnetotransport experiments on a moiré device with antidot period $a = 150$ nm, performed at high densities, beyond the sat. Dirac point. **(a)** $R_{xx}$ and $R_{xy}$ for $V_g = -85$ V. There is no indication of antidot features (see position of arrow), but several pronounced BZ oscillations can be reported. The dashed vertical lines correspond to $B = \phi_0/qA$, featuring minima in $R_{xx}$. **(b)** Set of curves for different carrier densities, proving stability and independence on the carrier density of the BZ oscillations.

stack ($V_{sat} \approx \pm 40$ V), but cannot present any reappearing antidot peaks. Fig. 8.7a illustrates a measurement at $V_g = -85$ V, where the black arrow marks the expected position of the fundamental antidot peak beyond the VHS. But we cannot observe a distinct commensurability feature. There is a prominent magnetoresistance at low fields and some oscillations in $R_{xx}$ and $R_{xy}$ at higher fields. The minima in the longitudinal resistance $R_{xx}$ can be assigned to Brown-Zak oscillations at $\phi_0/\phi = q$ ($q$ being an integer). Simultaneously, the Hall resistance $R_{xy}$ is undergoing a transition, tending towards zero. The carrier independence of the apparent BZ oscillations can be proved with the graph depicted in Fig. 8.7b, where the magnetoresistance minima appear at $B = \phi_0/qA$ for several different carrier densities. The reason for the relatively high temperature $T = 30 - 50$ K in the experiment is our interest in semiclassical antidot features and BZ oscillations, both being more robust to temperature than SdHOs [10, 201]. Nevertheless, we cannot exclude that weakly pronounced commensurability peaks are present, but covered with the evident moiré features.

Because of gate breakdown issues, we were not able to repeat this measurement at very high densities for any of our other heterostructures. All other experiments were limited to $V_g \approx \pm 50$ V, several volts beyond the secondary Dirac points, featuring moiré transport characteristics without a hint for recurring antidot peaks.

## 8.3 Conclusion

In conclusion, we fabricated several graphene moiré devices and characterized their transport properties before and after patterning of an additional square antidot lattice. We were able to observe commensurability features, stemming from the moiré as well as the antidot superlattice potential in our experiments and studied the interplay between both modulations. At moderate carrier densities, we reported distinct commensurability peaks, which get progressively suppressed as we increase the carrier density and approach the satellite Dirac points. We can explain this extinction in terms of an orbital switching of the cyclotron motion in the vicinity of the VHSs, but we cannot examine any recurring antidot features at higher densities beyond the VHSs. Moreover, we see additional $1/B$-periodic oscillations in our experiments. While the features at high densities can be identified as Brown-Zak oscillations, the superposed oscillations at moderate densities below the extra Dirac points can be most likely assigned to Shubnikov-de Haas oscillations. However, the anomalous mixing of the quantum Hall and the classical antidot regime in form of a superposition of the classical features with SdHOs remains unclear and requires further studies.

# CHAPTER 9

## hBN-graphene heterostructures with patterned bottom gates

Embedding graphene into a heterostructure with hexagonal boron nitride was shown to be an efficient way of achieving a high bulk mobility. The encapsulated graphene is protected in any further top-down fabrication procedure and pronounced commensurability peaks could be observed in 2D antidot lattices [10, 131].

In this chapter and in reference [12][1], we introduce a new method for periodical modulation of the carrier density, employing a few-layer graphene patterned bottom gate (PBG). The bottom gate is defined by etching a 2D hole array into the few layer graphene and adapts perfectly to the commonly used stacking method for van der Waals heterostructures. By tuning the local patterned bottom gate and the global back gate voltage, we can consistently switch between the unipolar and bipolar transport regime, and erase or enhance the induced potential modulation in our system.

We fabricated graphene patterned bottom gates with square lattice periods down to $a = 100$ nm and observe commensurability features in magnetotransport experiments, stemming from weak or strong potential modulation in the unipolar and bipolar regime, respectively. The commensurability peaks in the bipolar regime can be nicely compared to experiments with hard-wall graphene antidot lattices and the commensurability oscillations in the unipolar regime can be attributed to Weiss oscillations in a weakly modulated 2D system [13, 129]. A variation of the induced modulation strength strongly influences the carrier mobility in graphene, with a fluctuation of almost one order of magnitude between unipolar and bipolar case in some samples. Moreover, our measurements indicate

---

[1] Some details of device fabrication and zero-field characterization, reported in this chapter, are adapted from our publication: M. Drienovsky, A. Sandner *et al.*, arXiv:1703.05631 (2017)

a strong robustness of the commensurability features in graphene with respect to temperature.

## 9.1 Device geometry and characteristics

To assure full screening of the global back gate electric field, we select multilayer graphene flakes consisting of 2-5 layers for the bottom gates in our experiments. Additionally, the minimal height of the few-layer graphene flake allows us to neglect any spatial perturbation of the heterostructure transferred on top of the graphene gate structure [12]. Moreover, the graphene PBG adapts perfectly to the commonly used stacking method for van der Waals crystals [7, 98], and in combination with hBN, sharp potential steps on a nanoscale can be created. The few-layer graphene is patterned via electron beam lithography and oxygen plasma reactive ion etching and features a 2D periodic array of holes. Subsequently, a hBN-graphene-hBN hybrid structure is put on top of the PBG and further patterning steps are conducted. Fig. 9.1c depicts a finished stack with a purple few-layer graphene PBG, independently contacted from both Hall bar structures. A more detailed description of the fabrication procedure is given in section 5.4.

We successfully fabricated and measured transport properties of encapsulated graphene on patterned gates with lattice constants of $a = 100 \ldots 300$ nm and hole diameters of $d = 50 \ldots 150$ nm. Fig. 9.1a shows a semi-transparent sketch of an encapsulated graphene structure with a few-layer graphene PBG on a Si/SiO$_2$ wafer. The lateral modulation of the charge carrier density in this setup can be influenced by the interplay between the global Si back gate and the local graphene PBG. The Si back gate only affects the graphene areas above the holes and the rest of the biased graphene sheet is screened by the PBG (see Fig. 9.1b). Using ultra-thin hBN as an insulating substrate between the PBG and the graphene layer, stray fields can be significantly reduced and sharp potential profiles can be created. The most interesting feature of this device design is the possibility to tune between the unipolar and bipolar transport regime, i.e. generating a 2D array of *pn*-junctions.

We probed the sheet conductivity as a function of the voltage applied to the PBG $V_p$ for different global back gate voltages $V_g$ for a sample with $a = 300$ nm and $d = 150$ nm (see Fig. 9.1d). The interplay between the two gates has a clear influence on the transport properties of the device. While the curve for $V_g = 0$ V is quite narrow and symmetric, this is no longer true for measurements with applied $V_g$. There, we see a difference in the $\sigma_s(V_p)$-curves between the unipolar (e.g. $V_g, V_p > 0$) and the bipolar case (e.g. $V_g > 0, V_p < 0$). If we extract the corresponding charge carrier mobilities from the slopes, we get $\mu \approx 10\,000$ cm$^2$/Vs in the bipolar and $\mu \approx 40\,000$ cm$^2$/Vs in the unipolar regime, which is essentially the same as in the case of $V_g = 0$ V. While the mobility in the bipolar regime is considerably decreased by reflections and scattering at the imposed *pn*-junctions

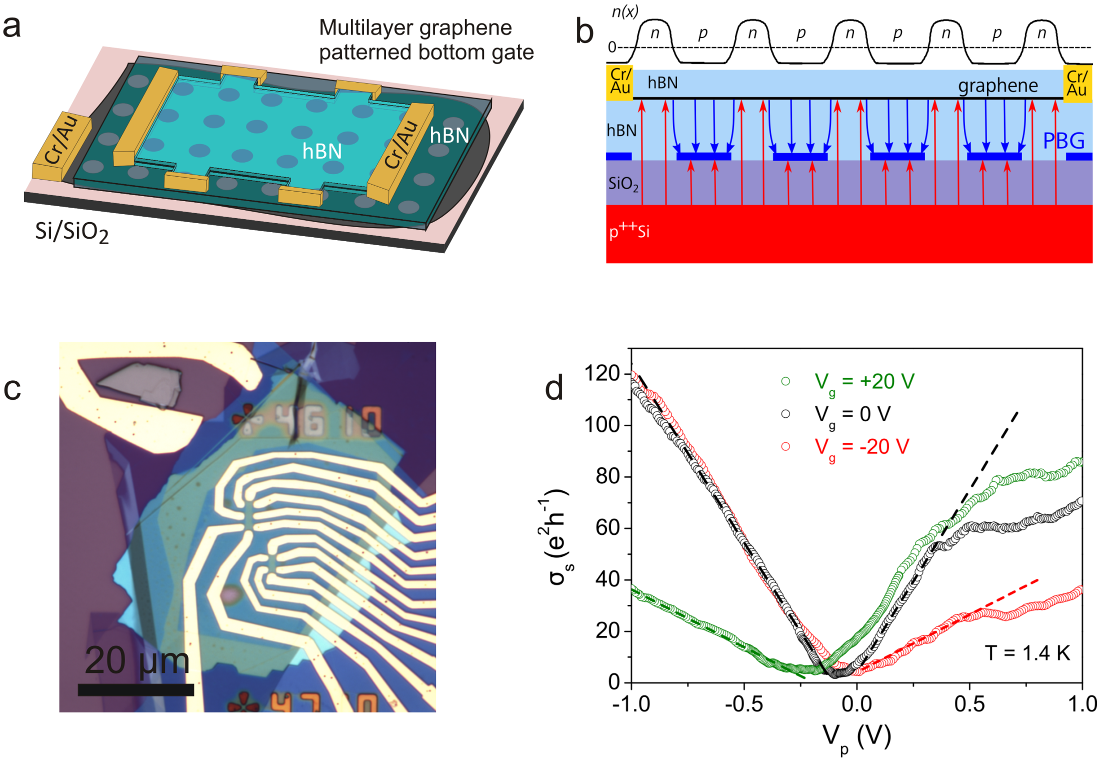

**Figure 9.1:** Sample layout, electrostatics and characterization of both gates. **(a)** Semitransparent sketch of the sample architecture for a hBN-graphene-hBN heterostructure with a multilayer graphene patterned bottom gate (PBG) and a global Si back gate. First, the hole array for the multilayer graphene bottom gate is fabricated, and subsequently, the hBN-graphene heterostructure is transferred on top and patterned (see chapter for details). **(b)** Cross section shows the different layers and the field lines of the gate electrodes. The global Si back gate is acting on the graphene areas above the holes of the patterned graphene gate, and the remaining area is screened by the few-layer graphene gate. Employing this design, we can tune both gates independently and generate different density profiles $n(x)$, e.g. bipolar ($npn$) for different polarities of both gates (as shown in this figure). **(c)** Optical micrograph of a finished sample. The large purple multilayer graphene PBG is contacted independently from the two Hall bar structures. **(d)** Sheet conductivity $\sigma_s$ as a function of the PBG voltage $V_p$ for different global back gate voltages $V_g$ at $T = 1.4$ K.

in the graphene layer, this effect seems to be much weaker in the unipolar case.

## 9.2 Magnetotransport experiments with tunable superlattice potential modulation

Lateral superlattices on 2DEGs have been studied intensively and revealed several new effects stemming from a commensurability of the imposed potential period $a$ and the magnetic length $l_B$ [14, 13, 129]. An important parameter for experiments with imposed superlattice structures is the strength of the potential modulation $V_0$ compared to the Fermi energy $E_F$ of the 2DEG [206]. Commensurability oscillations, so-called Weiss oscillations [14, 121], are dominating the magnetoresistance for weak potential modulation, $V_0 \ll E_F$. In a semi-classical picture, the commensurability oscillations can be explained by an average drift of the center of weakly perturbed cyclotron orbits in the system [139]. In the strongly modulated system, however, electrons are classically excluded from “islands” in the Fermi sea and the magnetoresistance peaks [130, 206, 207] are resulting from pinned orbits induced by nonlinear resonances in a prevalent chaotic phase space [152, 189, 208].

One advantage of monolayer graphene over conventional 2DEGs is the ability to continuously tune its Fermi energy $E_F$ from electron to hole regime without crossing any gap. This allows us to induce *pn*-junctions in graphene via local electrostatic gating [41, 42, 209] and move from a unipolar ($nn'n$ or $pp'p$) to a bipolar transport regime (*pnp*). In this way, we can approach the extreme modulation regimes in the unipolar and bipolar case (weak and strong modulation, respectively) and the transition in between, just by tuning the local PBG and the global back gate [12].

In the following parts, we show experimental data of encapsulated graphene on a multilayer graphene PBG with a 2D hole array of periodicity $a = 300$ nm and diameter $d = 150$ nm. All the measurements were performed in a $^4$He cryostat at low temperatures, using a standard Lock-in setup at low frequencies.

### 9.2.1 Experiments with zero back gate voltage

Fig. 9.2 depicts a magnetotransport trace for $V_g = 0$ V and $V_p = +3.0$ V. The potential modulation in the biased graphene sheet is induced by the graphene PBG and the areas above the holes are fixed to zero potential by the back gate. This situation can be seen in the sketch on the right hand side, depicting the carrier density distribution $n(x, y)$ and matching electron orbits for an idealized case of sharp potential steps. We can see two pronounced commensurability peaks at low magnetic fields (positive and negative $B$), corresponding to the fundamental antidot peaks around the depleted “antidot zones” in our system. The dominant commensurability peaks indicate a strong potential modulation in the graphene

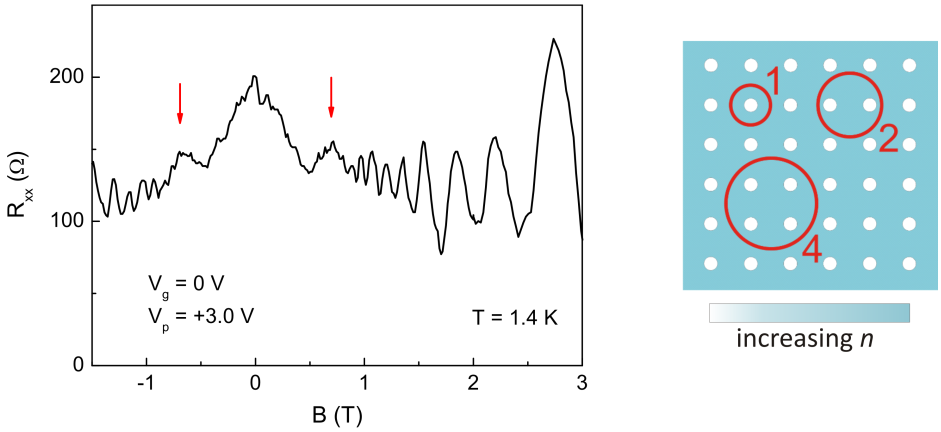

**Figure 9.2:** Magnetotransport with $V_g = 0$ V. Potential modulation is induced by graphene PBG (hole array with $a = 300$ nm and $d = 150$ nm). The areas above the holes of the PBG are fixed to zero potential. Electrons are orbiting around almost depleted "antidot zones" in this setup, and we observe a pronounced commensurability peak at low magnetic fields, indicating strong potential modulation. The red arrows show the expected $B$-field position of the fundamental commensurability features. The sketch on the right hand side is depicting the carrier density distribution $n(x, y)$ and matching electron orbits for an idealized case with sharp potential junctions and depleted zones.

device, and the red arrows in Fig. 9.2 mark the expected $B$-field position according to the commensurability condition, where the cyclotron diameter at the Fermi energy $2R_C = \frac{2\hbar}{eB}\sqrt{\pi n_s}$ is commensurate to the square antidot lattice. The magnetic field values are fitting well and we can compare our experimental situation with $V_g = 0$ V and $V_p \neq 0$ V to hard-wall antidot lattices, where the fundamental antidot peak belonging to $2R_C = a$ is most prominent [10, 14]. Therefore, the exact shape [210, 211] of the depleted regions and the steepness of the induced potential profile is not so important. The voids act as an array of artificial scatterers, similar to an antidot lattice, and chaotic dynamics along with nonlinear resonances in the phase space are responsible for the appearance of robust commensurability peaks in magnetotransport experiments [152, 195].

We estimate a charge carrier density of $n_s = 1.0 \cdot 10^{12}$ cm$^{-2}$ from the Shubnikov-de Haas oscillations at higher fields and deduce an apparent mobility of around $\mu = 48\,000$ cm$^2$/Vs for this density. Still, scattering at the potential steps limits the apparent carrier mobility [189], and the intrinsic electron mean free path $l_e$ might be well above the supposed mean free path of $l_{mfp} = \frac{\hbar}{e}\sqrt{\pi n_s}\mu = 560$ nm.

Moreover, we conducted magnetotransport experiments for several different gate voltages $V_p \neq 0$ V (and $V_g = 0$ V) and observe commensurability peaks at carrier densities down to $n_s = 3 \cdot 10^{11}$ cm$^{-2}$.

### 9.2.2 Commensurability peaks for strong modulation in the bipolar regime

Now, we want to discuss the bipolar transport regime, e.g. negative $V_g$ and positive $V_p$. This situation is depicted in Fig. 9.3 for the same sample as before ($a$ = 300 nm, $d$ = 150 nm). Fig. 9.3a shows an experiment with back gate voltage $V_g = -30$ V and patterned gate voltage $V_p = +3.5$ V. Again, we observe a commensurability peak at low fields, matching the expected position, and SdHOs at higher $B$, eventually resulting in a well-defined quantum Hall effect, similar to measurements on etched antidot lattices. In comparison to the experiments with $V_g = 0$ V (Fig. 9.2), the fundamental antidot peaks are enhanced and more dominant. On the right hand side, next to the measurement graph, is the corresponding carrier density map $n(x, y)$ for the applied gate voltages (see Fig. 9.3b)[2]. These maps are visualizing the induced carrier densities in the biased graphene sheet and the transitions between the differently gated areas. The red circles are representing $pn$-junctions in the system.

If we decrease the PBG voltage to $V_p = +1.5$ V for the same $V_g = -30$ V (Fig. 9.3c), we increase the gate-induced potential modulation and the fundamental antidot peaks are becoming more evident. We can extract an apparent mobility of around 30 000 cm$^2$/Vs from this measurement, which is a further decrease compared to the experiment for $V_g = 0$ V, shown in Fig. 9.2. The strongly enhanced potential modulation can be noticed in the complementary density map (Fig. 9.3d). Even if both simulations for the bipolar configurations are looking similar, the essential parameter is the different scaling of the maps.

What is new in our experiment, compared to etched antidot lattices, is the ability of electrons to perform Klein tunneling at the boundaries of the imposed $pn$-junctions. In addition to chaotic and pinned orbits in the superlattice structure [152], this mechanism can considerably influence the formation of commensurability peaks. There is an angle dependent transmission at the $pn$-transitions where not all of the incident carriers are reflected. Some charge carriers might tunnel through the “islands” or get trapped inside of them. What makes the situation even more complicated is the magnetic field dependence of the angular-dependent transmission [88, 93]. Thus, Klein tunneling at the imposed “antidot” definitely influences transport characteristics and commensurability features in our experiment. However, the exact mechanism and its impact on the formation of distinct antidot peaks remains unclear and requires substantial calculations.

---

[2] all simulations for the density maps were provided by Ming-Hao Liu, NCKU Taiwan

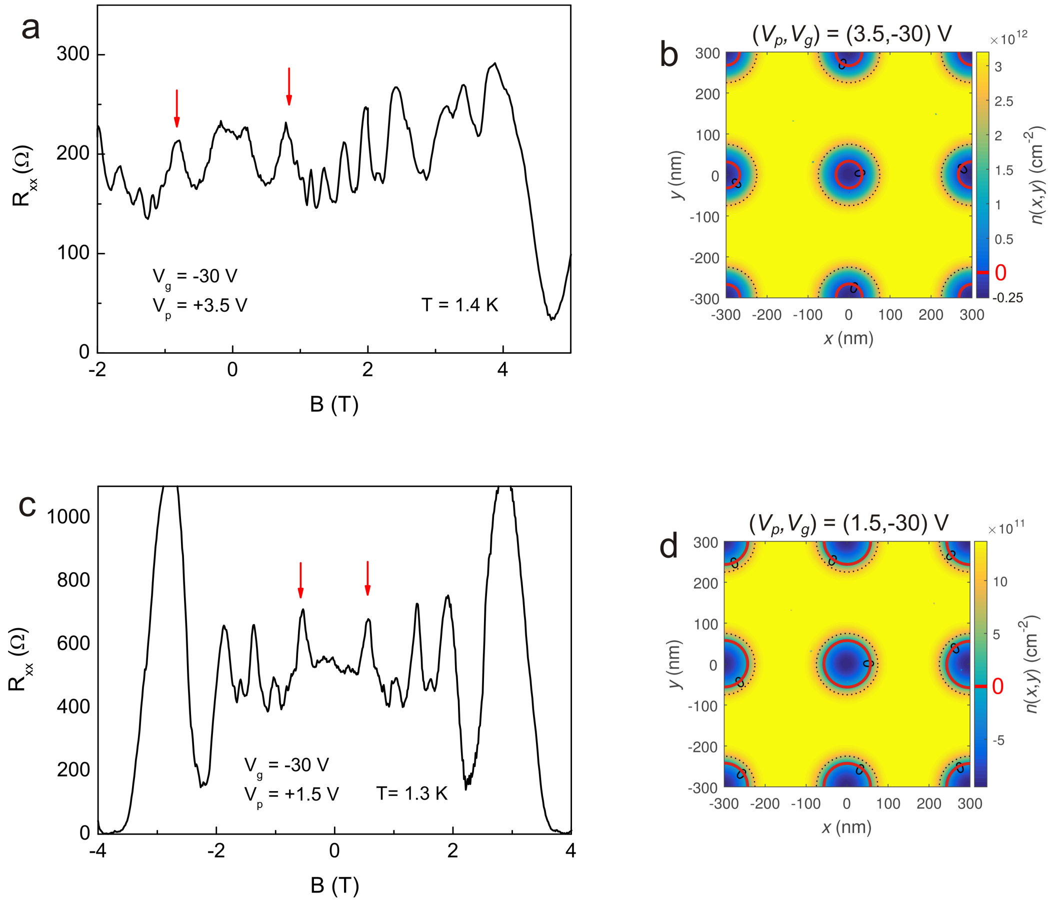

**Figure 9.3:** Transport experiments in the bipolar regime. The global back gate voltage is $V_g = -30$ V and a positive voltage is applied to the multilayer graphene PBG ($a = 300$ nm, $d = 150$ nm). **(a)** Experiment with $V_p = +3.5$ V. We observe additional commensurability peaks in $R_{xx}$ and their B-field position is matching the classical orbits known from hard-wall antidot lattices (see arrows for expected position). **(c)** Enhanced potential modulation for $V_p = +1.5$ V. The commensurability peak is sharp and pronounced, indicating strong potential modulation similar to etched antidot arrays. **(b)+(d)** Corresponding carrier density maps $n(x,y)$ for the experimental traces depicted in (a) and (c), respectively. Bipolar junctions (circles of zero density) are shown in red and dotted circles are depicting the geometrical positions of the holes in the PBG. The simulations were provided by Ming-Hao Liu, NCKU Taiwan.

### 9.2.3 Weiss oscillations in a weakly modulated unipolar regime

The situation changes drastically for transport experiments in the unipolar regime. Similar to before, we fixed the global back gate voltage to $V_g = -30$ V and varied the voltage applied to the PBG $V_p$. Fig. 9.4a depicts a magnetotransport trace for $V_p = -2.5$ V and we can not observe any commensurability feature at low magnetic fields. Moreover, the measurement is comparable to experiments in high-mobility graphene without superposed potential modulation, exhibiting a distinct quantum Hall regime down to fields below $B < 1$ T. An explanation for this behavior can be given with the connected carrier density map on the right hand side. The simulation supposes a lateral variation of the charge carrier density between the hole areas and remaining graphene plane of less than 10%. Thus, the superlattice potential, induced with this gate combination, is not sufficiently developed for the appearance of commensurability features in magnetotransport experiments.

An enhancement of the modulation strength by decreasing the PBG voltage to $V_p = -1.5$ V was done for the measurement illustrated in Fig. 9.4c. The modeling in Fig. 9.4d gives a stronger lateral alteration of the carrier density $n$ across the graphene sheet of roughly 30%. Again, the corresponding magnetotransport experiment features distinct SdHOs along a wide magnetic field range, but at low fields, we observe $1/B$-periodic commensurability oscillations, known as Weiss oscillations [13]. Weiss oscillations are a well understood phenomenon in 2DEGs submitted to a weak superlattice potential, reflecting the commensurability of cyclotron diameter $2R_C$ at the Fermi energy and the modulation period $a$. The appearance of Weiss oscillations in our magnetotransport experiment proves the ability to tune the superlattice potential from a quite homogeneous modulation to a weakly modulated regime in a unipolar gating setup. The minima of these oscillations can be expressed with the commensurability condition

$$2R_C = (\lambda - \frac{1}{4})a \qquad\qquad \lambda = 1, 2, ... \tag{9.1}$$

In a quantum mechanical context, Weiss oscillations are a result of the oscillatory dependence of the bandwidth of modulation-broadened Landau levels on the band index, and thus, the arising group velocity leads to a strongly anisotropic oscillatory Landau band conduction [129, 132]. The band-conductivity can be calculated employing a Kubo formalism [121, 212]. Equation 9.1 is the flat band condition for the Landau bands of oscillating width.

In the case of $V_p = -2.5$ V (Fig. 9.4a) the superlattice-induced potential modulation is just to weak to prevent the resolution of individual subbands, and distinct Landau bands with an oscillating miniband conductivity are not formed, yet. A simple approximation of the modulation amplitude

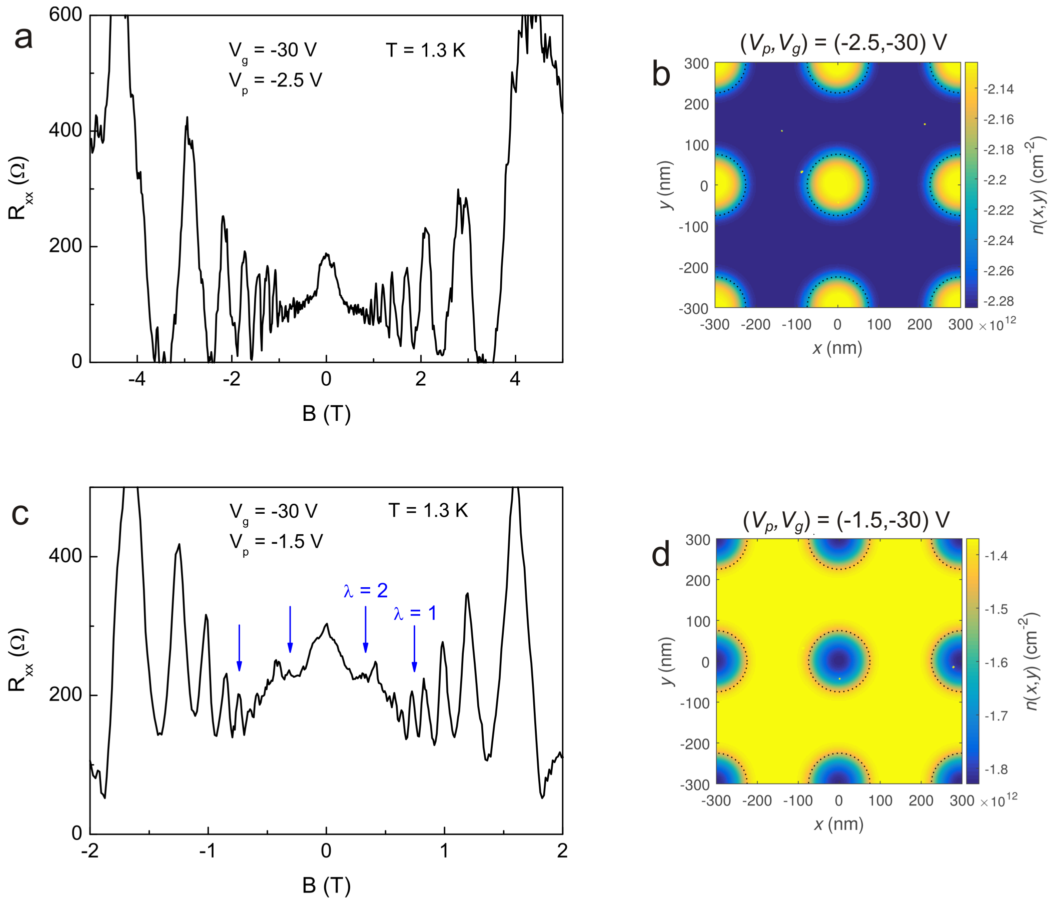

**Figure 9.4:** Magnetoresistance $R_{xx}$ in the unipolar regime. The global gate voltage is $V_g = -30$ V and a negative voltage is applied to the multilayer graphene PBG ($a = 300$ nm, $d = 150$ nm). **(a)** Experiment with $V_p = -2.5$ V. There is no indication of additional commensurability features. The magnetotransport trace is similar to measurements in high-mobility graphene without any modulation. **(b)** Corresponding carrier density map $n(x, y)$ for the experiment in (a). The density variation between the hole areas and remaining graphene plane is less than 10% and we achieve an almost homogeneous potential modulation. **(c)** Measurement for $V_p = -1.5$ V in a weakly modulated system. We observe two well pronounced commensurability oscillations $\lambda = 1, 2$ in $R_{xx}$, where the cyclotron diameter satisfies a flat band commensurability condition involving the lattice constant. **(d)** Relevant density map for the experiment in (c). The system shows a weak potential modulation with a density variation of around 30% across the graphene plane. The simulations were provided by Ming-Hao Liu, NCKU Taiwan.

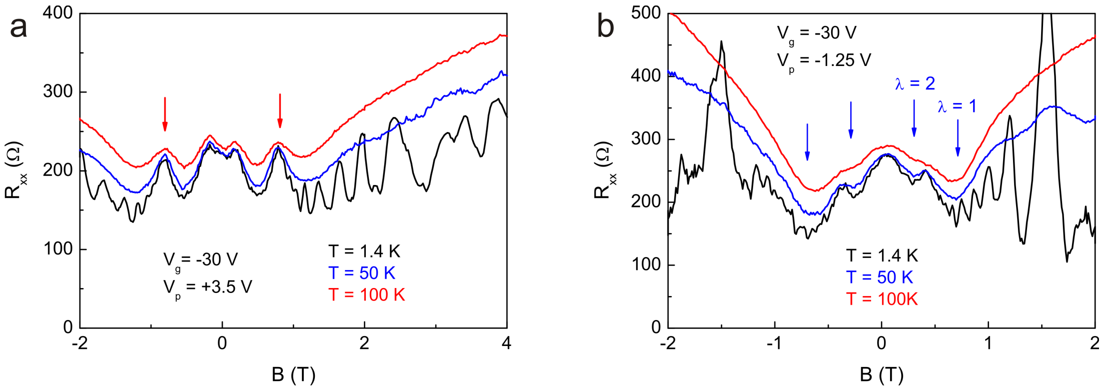

**Figure 9.5:** Temperature dependence of the commensurability features for weak and strong potential modulation. **(a)** Experiment for strong modulation in the bipolar regime ($V_g = -30$ V, $V_p = +3.5$ V). **(b)** Experiment for a weak superlattice potential in the unipolar regime ($V_g = -30$ V, $V_p = -1.25$ V). The commensurability features in both graphs are more robust to temperature than the Shubnikov-de Haas oscillations at higher fields, proving the semiclassical origin from cyclotron trajectories.

$$V_0 = \Delta E = \sqrt{\pi}\hbar v_F(\sqrt{n_{s,max}} - \sqrt{n_{s,min}}) \tag{9.2}$$

for this gate configuration gives $V_0 \approx 6$ meV. If we compare this value to the global Fermi level of our experiment, we can deduce a relatively weak induced superlattice modulation of $V_0/E_F < 5\%$, which explains the absence of commensurability features in our measurement. Doing the same valuation for the experiment with enhanced modulation corresponding to $V_p = -1.5$ V (Fig. 9.4c) results in a relative modulation of $V_0/E_F \approx 15\%$. The considerably stronger superlattice modulation is sufficient to enter the weak modulation regime, accompanied with Weiss oscillations in magnetotransport experiments.

### 9.2.4 Temperature dependence of the commensurability oscillations

Commensurability features exhibit a clearly different temperature dependence than quantum oscillations. Fig. 9.5 depicts temperature-dependent experiments in the bipolar and unipolar regime, featuring commensurability peaks and Weiss oscillations, respectively. In the bipolar case (Fig. 9.5a) at $T = 1.4$ K, we observe dominant magnetoresistance peaks at low fields and distinct SdHOs in the quantum Hall regime at higher $B$. However, increasing temperature leads to a extinction of the SdHOs, while the commensurability peaks remain clearly visible. The same behavior can be reported for the weakly modulated unipolar regime in Fig. 9.5b, where Weiss oscillations are more robust to temperature and can be observed up to $T = 100$ K. We ascribe the different $T$-dependence of the commensurability features to the semi-classical origin from cyclotron orbits in a magnetic field. In the case of strong modulation, the peaks can be explained in terms of pinned orbits and chaos, and experiments on hard-wall antidot lattices showed a similar $T$-dependence [123]. At very low temperatures, commensurability and Shubnikov-de Haas oscillations can be superposed with quantum oscillations, e.g. Aharanov-Bohm type oscillations [148, 147]. Increasing the temperature results in thermal smearing of the cyclotron orbits at the Fermi energy and quantum oscillations vanish. The relevant energy scale for the SdHOs is the Landau level spacing $\Delta E_n$, and quantum Hall features disappear for $k_B T > \Delta E_n$. Commensurability features can be still observed at even higher temperatures, and experiments by Heremans *et al.* on semiconductor 2DEGs propose a combination of thermal smearing and increasing electron-scattering rate as reason for the reduction of the amplitudes of the commensurability peaks with increasing temperature [213].

Beton *et al.* give a similar classical argument for the fading of the commensurability oscillations in a weakly modulated 2DEG [136]. The thermal smearing of the cyclotron diameter $\Delta 2R_C$ needs to be smaller than the superlattice potential period $a$. Otherwise the commensurability features get suppressed. This energy scale, where the classical features can be resolved, is typically considerably larger than the cyclotron energy $\hbar\omega_c$ for SdHOs in semiconductor heterostructures. Since the critical temperature, where the semi-classical features vanish, is proportional to the Fermi velocity in graphene, commensurability features should be observable at even higher temperatures than in conventional 2DEGs [214].

## 9.3 Experiments on further devices

Moreover, we performed similar experiments on stacks with different patterned bottom gate periodicities $a$ and diameters $d$. Overall, the observations are complimentary to the measurements on stack 38, shown in the sections before. Fig. 9.6 shows low-temperature magnetotransport traces of a stack with a hole array of $a = 200$ nm and $d = 50$ nm, etched in the multilayer graphene PBG.

The left graph depicts an experiment in the unipolar transport regime for $V_g = +20$ V and $V_p = +2.5$ V. We report no indication of commensurability features in this measurement. In fact, the superlattice potential modulation is very weak and almost as homogeneous as we can get. This fact reflects in the high apparent Hall mobility of $\mu = 150\,000$ cm$^2$/Vs in this experiment.

On the other hand, there are prominent commensurability peaks in the bipolar regime for $V_g = +20$ V and $V_p = -2.5$ V (see Fig. 9.6b). We see a rich magnetotransport structure and can identify pronounced commensurability peaks corresponding to orbits around $n = 1$ and 2 gate-induced “islands” at low fields. Furthermore, the apparent mobility for this bipolar configuration is limited to $\mu = 25\,000$ cm$^2$/Vs. So our experimental device layout, employing two interact-

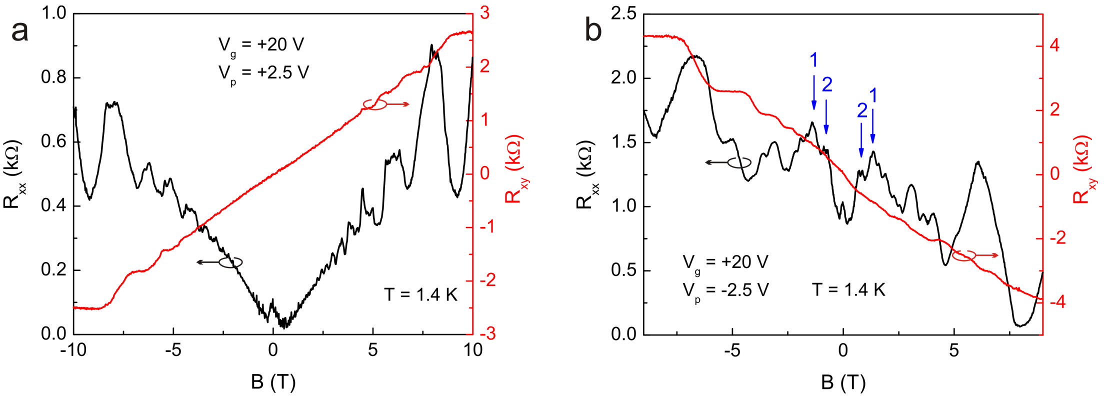

**Figure 9.6:** Magnetotransport experiments in the unipolar and bipolar regime for a device with a multilayer graphene PBG with $a = 200$ nm and $d = 50$ nm. **(a)** Experiment for a quite homogeneous potential distribution in a unipolar case, induced by the PBG and the global back gate. We do not observe any commensurability features, and the carrier mobility is as high as $\mu = 150\,000$. **(b)** Experiment for strong potential modulation in the bipolar regime. We see two commensurability peaks that we can assign to electron orbits around $n = 1$ and 2 induced "holes" in the graphene plane.

ing gates, allows us to efficiently tune the carrier mobility over a wide range in our system.

## 9.4 Conclusion

In conclusion, we showed that employing graphene patterned bottom gates is a versatile approach for the investigation of lateral superlattice effects in graphene heterostructures. The PBG can be customized for any experiment, easily implemented in the commonly used van der Waals stacking method, and offers several advantages over conventional metal top gates. Our geometry allowed us to tune the PBG and the global back gate independently and thus, to move from a homogeneous to a unipolar and bipolar potential distribution. In this way, we could probe commensurability features in the unipolar (Weiss oscillations) and bipolar regime (antidot peaks), induced by weak and strong potential modulation, respectively. The experimental results can be nicely compared to similar measurements on conventional 2DEGs with the distinct discrepancy resulting from Klein tunneling in bipolar graphene. However, the impact of present Klein tunneling in our magnetotransport experiments remains unclear. Furthermore, we demonstrated the ability to tune the apparent carrier mobility in this experiment over the wide range of almost one order of magnitude.

# CHAPTER 10

# Conclusions and outlook

The first aim of this work was the successful implementation and optimization of the transfer process in our lab. High-mobility graphene devices were indispensable for our intention to investigate superlattice effects. In the beginning, we started with a wet, layer-by-layer stacking method that provided only marginally improved samples compared to conventional graphene structures on $SiO_2$. However, the subsequent employment of a dry van der Waals pick-up procedure and the fabrication of 1D edge contacts significantly improved sample quality and regularly yielded graphene heterostructures with mobilities exceeding 100 000 $cm^2/Vs$.

The considerably enhanced sample quality could be proved in magnetotransport experiments on encapsulated hBN-graphene hybrid structures, where we observed symmetry-broken quantum Hall states at fields down to only a few T, accompanied with several fractional quantum Hall states at higher fields. Another confirmation for the high quality was the experimental observation of transverse magnetic focusing in our encapsulated devices.

So, the bulk mobility of graphene could be improved with the introduction of hBN-graphene heterostructures, but any further nanostructuring procedure could potentially degrade graphene's intrinsic properties. In this work, we showed that an encapsulation of graphene between hBN protects and conserves the high quality of graphene in subsequent patterning steps. Accordingly, magnetotransport experiments on graphene antidot lattices displayed several commensurability peaks that could be assigned to electron orbits around one or several etched antidots. In our experiments, we could approach the transition between the classical and the quantum transport regime at low carrier densities, where the semiclassical commensurability peaks vanish if the Fermi wavelength exceeds the neck width of the constrictions in between the antidots of the rectangular lattice. Moreover, our experimental results were nicely reproduced by theoretical simulations of Power *et al.* [11] and Datseris *et al.* [195].

The same fabrication scheme can be used for encapsulated graphene moiré samples, where we studied the interplay between the moiré and an additionally imposed antidot potential. For this purpose, we fabricated several graphene moiré devices and characterized them via transport measurement before and after patterning of the additional antidot array. The moiré superlattice potential leads to a suppression of the antidot features at higher densities, approaching the satellite Dirac points. This phenomenon can be understood in terms of an orbital switching of the cyclotron motion in the vicinity of van Hove singularities of the moiré dispersion, manifesting in “run-away” orbits instead of closed orbits. Another observation, induced by the moiré potential, is the superposition of the classical antidot features with Shubnikov-de Haas oscillations. This behavior has not been reported for antidot lattices in conventional 2DEGs nor in graphene, and the origin of this effect is not totally understood, yet.

Another interesting geometry for superlattice potential modulation is the utilization of patterned graphene bottom gates. In combination with the global Si back gate of our wafers, we can consistently tune the potential distribution in the biased graphene sheet from unipolar to bipolar, and examine the resulting commensurability effects in the respective transport regimes. We reported well-developed Weiss oscillations in the unipolar case, for weak potential modulation, and distinct antidot peaks for strong modulation, in the bipolar regime, for a graphene gate with a 2D array of holes. Furthermore, our measurements showed a clear dependence of the carrier mobilities in our samples on the magnitude of the superlattice potential, strongly decreasing with an enhancement of the potential strength.

All in all, we were able to investigate 2D superlattices on high-mobility graphene heterostructures, employing different geometries and sample layouts. We proved that our approach of nanopatterning encapsulated graphene structures is convenient and encouraging for a multitude of experiments and gives the chance to experimentally access interesting physics such as the Hofstadter butterfly in graphene antidot lattices with very small lattice constants. Furthermore, patterned graphene gates provide the possibility to fabricate complex gate structures and superlattice potential profiles, which can be used to examine commensurability features in transport experiments or for lensing electron beams in graphene electron optics experiments [215].

# APPENDIX A

## List of Symbols and Abbreviations

| | |
|---|---|
| **1D, 2D, 3D** | One-, two-, three-dimensional |
| **2DEG** | Two-dimensional Electron Gas |
| $a$ | Antidot lattice period |
| **AC** | Alternating current |
| **AFM** | Atomic Force Microscopy |
| **AD** | Antidot |
| $B$ | Magnetic field |
| $B_0$ | Normalized magnetic field ($B/B_0 = 1$ for fundamental AD peak) |
| **BZ** | Brown-Zak |
| $C_g$ | Capacitive gate coupling |
| **COs** | Commensurability Oscillations |
| **CVD** | Chemical vapor deposition |
| $d$ | Diameter of the antidots |
| **DC** | Direct current |
| **DOS** | Density of states |
| **DP** | Dirac point |
| $\epsilon$ | Dielectric constant |
| $e$ | Elementary charge |
| **EBL** | Electron Beam Lithography |
| $E_F$ | Fermi energy |
| $E_n$ | Landau level energy |
| $\phi, \phi_0$ | Magnetic flux, flux quantum |
| $h = 2\pi\hbar$ | Planck constant |
| **hBN** | Hexagonal Boron Nitride |
| **HOPG** | Highly-Oriented Pyrolitic Graphite |
| $k_B$ | Boltzmann constant |

| | |
|---|---|
| $\lambda$ | Moiré superlattice wavelength, index of Weiss oscillations |
| $\lambda_F$ | Fermi wavelength |
| $l_B$ | Magnetic length |
| $l_e$, $l_{mfp}$ | Intrinsic mean free path, apparent mean free path |
| **LL** | Landau level |
| $\mu$ | Charge carrier mobility |
| $\nu$ | Filling factor |
| $n$ | Landau quantum number, index of antidot peaks |
| $n_s$ | Charge carrier density |
| **PBG** | Patterned bottom gate |
| **PMMA** | Polymethyl methacrylate |
| **(F/I)QHE** | (Fractional/Integer) Quantum Hall effect |
| $R_C$ | Cyclotron radius |
| **RIE** | Reactive Ion Etching |
| $\sigma_s$ | Sheet conductivity |
| **SBZ** | Superlattice Brillouin zone |
| **SEM** | Scanning electron microscope |
| **SdHOs** | Shubnikov-de Haas oscillations |
| **STM** | Scanning Tunneling Microscopy |
| **SU** | Special Unitary group |
| $T$ | Temperature |
| $t$ | Transmission probability |
| **TMF** | Transverse magnetic focusing |
| **UHV** | Ultra-high Vacuum |
| $V_0$ | Potential modulation |
| $v_F$ | Fermi velocity |
| $V_g$ | Global gate voltage |
| **VHS** | Van Hove Singularity |
| $V_p$ | Patterned gate voltage |
| **WL** | Weak localization |

# APPENDIX B

## Fabrication details and recipes

### Exfoliation of graphene

- Cleaning of the p$^{++}$-doped Si/SiO$_2$ substrates with sonication in acetone and isopropanol
- Plasma asher: Pressure 2.0 mbar, power: 30 %, 4 min
- Mechanical exfoliation of graphene, using HOPG or natural graphite and Nitto tape ELP BT- 150ECM (Nitto Denko Corp.)

### Exfoliation of hBN

- Cleaning procedure is similar to graphene
- Mechanical exfoliation of hBN, using hBN single crystals provided by Taniguchi and Watanabe and Nitto tape ELP BT- 150ECM

### Fabrication of PMGI/PMMA stacks as for transfer

- Cleaning of the p$^{++}$ doped Si/SiO$_2$ substrates (90 nm SiO$_2$) with sonication in acetone and isopropanol
- Plasma asher: Pressure 2.0 mbar, power: 40 %, 4 min
- Spincoating PMGI SF6 (Microchem):
  first layer: 4500 rpm 30 s, hotplate 90° C 4 min
  second layer: 3000 rpm 5 s and 6000 rpm 30 s, hotplate 90° C 8 min
- Spincoating PMMA 950k A5 (5% in chlorbenzene):
  first layer: 2000 rpm 35s, hotplate 90° C 4 min
  second layer: 3000 rpm 5 s and 6000 rpm 30 s, hotplate 90° C 8 min

## Fabrication of Hall bar structures in hBN-graphene-hBN heterostructures

- Annealing of the transferred hBN-graphene hybrid structure at 320-400° C for several hours (in forming gas atmosphere)
- AFM characterization of the stack for identification of suitable areas
- Spincoating PMMA 950k A5: 3000 rpm 5 s and 6000 rpm 30 s, hotplate 150° C 6 min
- EBL for Hall bar etching (with Supra SEM): EHT 30 kV, aperture 30 $\mu$m, area dose 310 $\mu$C/cm$^2$
- Developing: MIBK/isopropanol (1:3) 80 s + isopropanol 30 s
- RIE etching of Hall bar: $CHF_3$ 40 sccm + $O_2$ 6 sccm, 55 mTorr, 35 W, etching rate for hBN is approximately 0.8 nm/s
- Spincoating PMMA 200k A9: 3000 rpm 5 s and 6000 rpm 30 s, hotplate 150° C 4 min + PMMA 950k A5: 3000 rpm 5 s and 6000 rpm 30 s, hotplate 150° C 6 min
- EBL for contacts (with Supra SEM): EHT 30 kV, aperture 30+120 $\mu$m, area dose 450 $\mu$C/cm$^2$
- Developing: MIBK/isopropanol (1:3) 80 s + isopropanol 30 s
- RIE etching of contact areas: $O_2$ 20 sccm, 27 mTorr, 20 W, 30 s
- Metal e-beam evaporation (Univex B): 4 nm Cr and 80 nm Au
- Lift-off in warm acetone for 60 min

## Patterning of antidot lattices

- Start with a finished hBN-graphene heterostructure with etched Hall bar and contact metalization
- Spincoating PMMA 950k A2: 3000 rpm 5 s and 6000 rpm 30 s, hotplate 150° C 6 min
- EBL of antidots (with Auriga REM): EHT 30 kV, aperture 30 $\mu$m, point dose 3.5 fC
- Developing: MIBK/isopropanol (1:3) 80 s + isopropanol 30 s
- RIE etching of antidots: $CHF_3$ 40 sccm + $O_2$ 6 sccm, 55 mTorr, 60 W, etching rate for hBN is approximately 1.2 nm/s

## Fabrication of few layer graphene patterned bottom gates

- Start with a suitable few-layer graphene flake (3-5 layers)
- Spincoating PMMA 950k A5: 3000 rpm 5 s and 6000 rpm 30 s, hotplate 150° C 6 min
- EBL for patterned gate (with Auriga REM): EHT 30 kV, aperture 30 $\mu$m, area dose 350 $\mu$C/cm$^2$
- Developing: MIBK/isopropanol (1:3) 80 s + isopropanol 30 s
- RIE etching of the flake: $O_2$ 20 sccm, 30 mTorr, 20 W, 75 s

# APPENDIX C

# Analysis of SdHOs in moiré and antidot superlattices

In this chapter we will give a detailed analysis of the Shubnikov-de Haas oscillations in our magnetotransport experiments on graphene moiré devices with an etched antidot array. As discussed in chapter 8, we observe a superposition of the commensurability features with $1/B$-periodic oscillations as we approach the satellite Dirac points in the moiré potential. Here, we will show that these oscillations are most likely SdHOs with the same periodicity from high fields down to low fields, well below the antidot peaks. Fig. C.1 and C.2 depict the corresponding graphs of magnetotransport experiments at different carrier densities and some analysis of the SdHOs. Both figures are similar, with antidot periodicities of $a = 250$ and 100 nm for Fig. C.1 and Fig. C.2, respectively. Graphs (a)-(c) are illustrating measurements and the vertical dashed lines are marking the positions of the SdHOs at the particular density. The expected positions are matching the minima in $R_{xx}$, proving the same origin of all $1/B$-periodic oscillations, even of those below the antidot peaks (marked with arrows). This observation is in line with the evaluation of the $R_{xx}$ minima as function of $1/B$, shown in graphs (d). The squares and dots correspond to SdHOs at fields higher and lower than the $n = 1$ antidot peak, respectively, and are linear in $1/B$. Moreover, we see a pronounced dependence of the additional oscillations on the carrier density, similar to the expected behavior of Shubnikov-de Haas oscillations in graphene, and the extracted densities $n_s$ are matching the induced carriers by the capacitive gate coupling (according to equation 3.1).

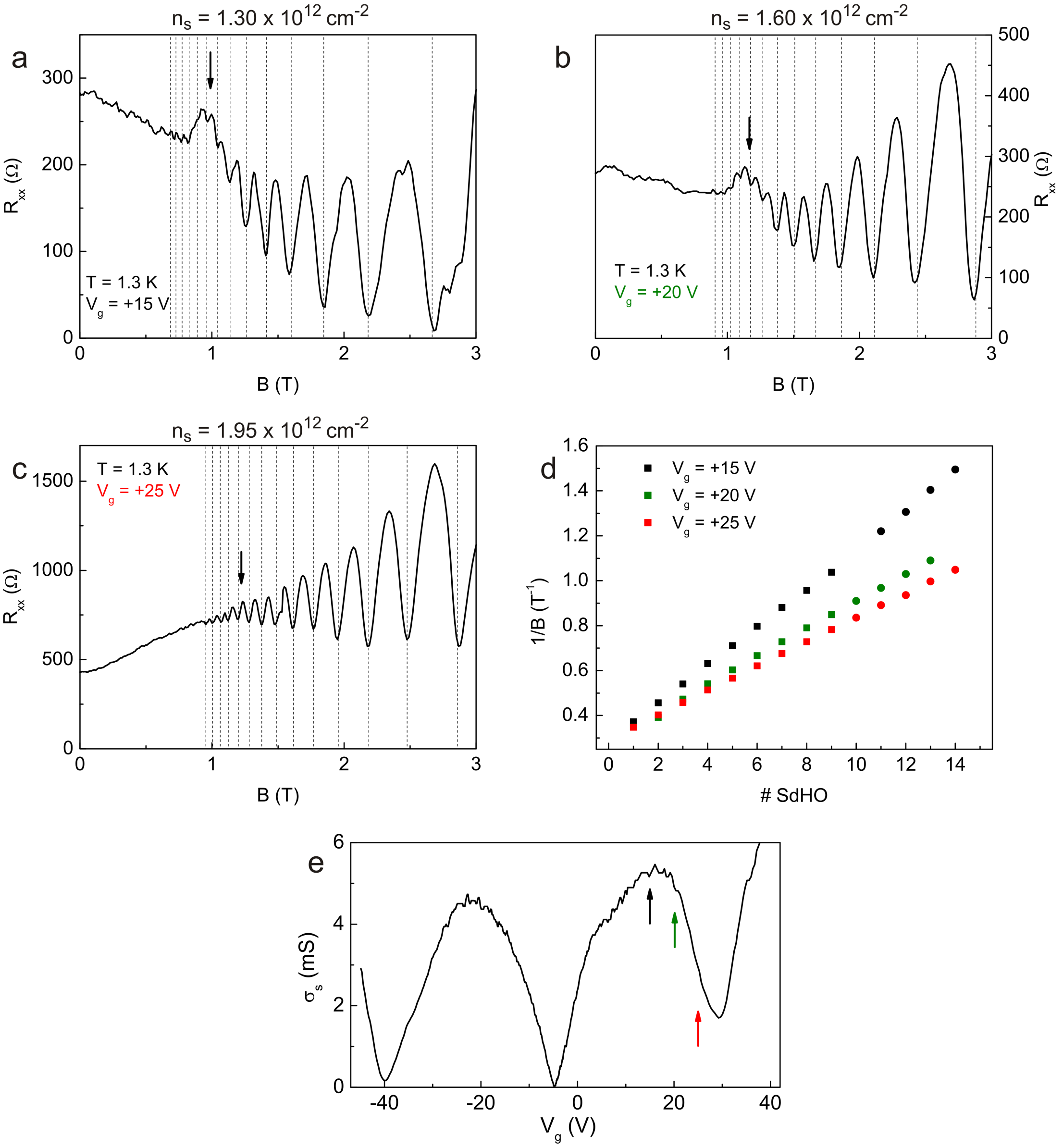

**Figure C.1:** Analysis of the periodicity of the SdHOs for a moiré device with $a = 250$ nm. **(a)-(c)** Same experiments as shown in Fig. 8.5 with vertical dashed lines for the expected positions of the SdHOs for the extracted carrier densities. **(d)** Analysis of the periodicity of the $R_{xx}$-minima in our curves, showing the same $1/B$-periodicity at higher fields above the fundamental antidot peak (squares), and below (circles). **(e)** Sheet conductivity $\sigma_s$ versus gate voltage $V_g$ with minima at the main and the secondary Dirac points, depicting the examined densities with color-coded arrows.

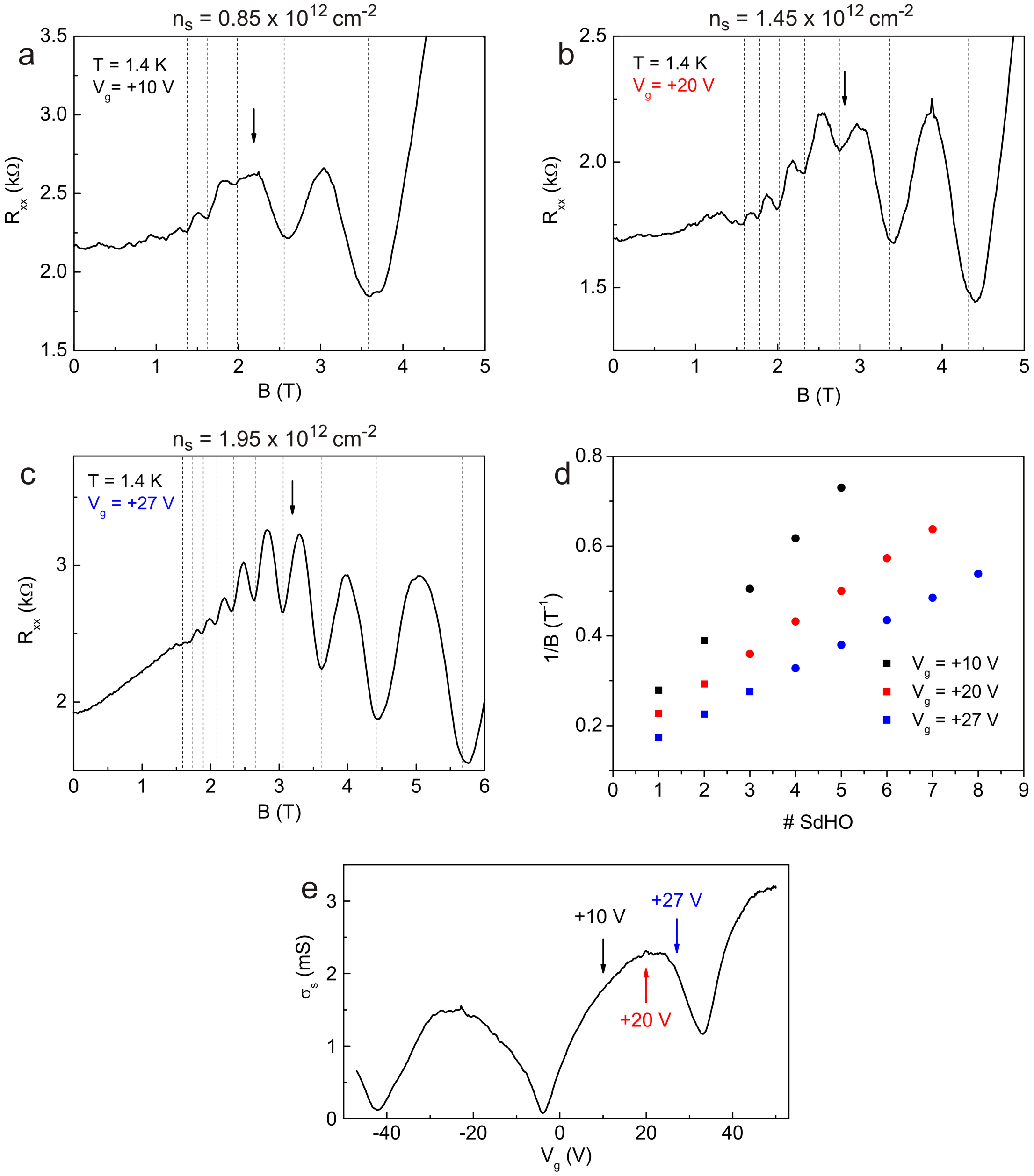

**Figure C.2:** Analysis of the periodicity of the SdHOs for a moiré device with $a =$ 100 nm. **(a)-(c)** Magnetotransport experiments with vertical dashed lines for the expected positions of the SdHOs for the extracted carrier densities. **(d)** Analysis of the periodicity of the $R_{xx}$-minima in our curves, showing the same $1/B$-periodicity at higher fields above the fundamental antidot peak (squares), and below (circles). **(e)** Sheet conductivity $\sigma_s$ versus gate voltage $V_g$ with minima at the main and the secondary Dirac points, depicting the examined densities with color-coded arrows.

# Bibliography

[1] V. Umansky, M. Heiblum, Y. Levinson, J. Smet, J. Nübler, and M. Dolev, "MBE growth of ultra-low disorder 2DEG with mobility exceeding $35 \times 10^6$ cm$^2$/Vs," *Journal of Crystal Growth*, vol. 311, no. 7, pp. 1658–1661, 2009. (Cited on page 1)

[2] K. S. Novoselov, A. K. Geim, S. V. Morozov, D. Jiang, M. I. Katsnelson, I. V. Grigorieva, S. V. Dubonos, and A. A. Firsov, "Two-dimensional gas of massless Dirac fermions in graphene," *Nature*, vol. 438, pp. 197–200, Nov. 2005. (Cited on pages 1, 10, 19 and 20)

[3] H. Lammer, "Sporting goods with graphene material," April 11 2013. US Patent App. 13/690,693. (Cited on page 1)

[4] S. Bae, H. Kim, Y. Lee, X. Xu, J.-S. Park, Y. Zheng, J. Balakrishnan, T. Lei, H. Ri Kim, Y. I. Song, Y.-J. Kim, K. S. Kim, B. Ozyilmaz, J.-H. Ahn, B. H. Hong, and S. Iijima, "Roll-to-roll production of 30-inch graphene films for transparent electrodes," *Nat Nano*, vol. 5, pp. 574–578, Aug. 2010. (Cited on page 2)

[5] M. F. El-Kady, V. Strong, S. Dubin, and R. B. Kaner, "Laser Scribing of High-Performance and Flexible Graphene-Based Electrochemical Capacitors," *Science*, vol. 335, pp. 1326–, Mar. 2012. (Cited on page 2)

[6] A. F. Young, C. R. Dean, L. Wang, H. Ren, P. Cadden-Zimansky, K. Watanabe, T. Taniguchi, J. Hone, K. L. Shepard, and P. Kim, "Spin and valley quantum Hall ferromagnetism in graphene," *Nat Phys*, vol. 8, pp. 550–556, July 2012. (Cited on pages 2, 20, 21, 59, 61 and 68)

[7] C. R. Dean, A. F. Young, I. Meric, C. Lee, L. Wang, S. Sorgenfrei, K. Watanabe, T. Taniguchi, P. Kim, S. K. L., and H. J., "Boron nitride

substrates for high-quality graphene electronics," *Nat. Nano.*, vol. 5, no. 10, pp. 722–726, 2010. (Cited on pages 2, 21, 29, 30, 59, 68, 80, 81 and 92)

[8] C. R. Dean, A. F. Young, P. Cadden-Zimansky, L. Wang, H. Ren, K. Watanabe, T. Taniguchi, P. Kim, J. Hone, and K. L. Shepard, "Multicomponent fractional quantum Hall effect in graphene," *Nat Phys*, vol. 7, pp. 693–696, Sept. 2011. (Cited on pages 2, 11, 22, 59, 63 and 68)

[9] K. I. Bolotin, F. Ghahari, M. D. Shulman, H. L. Stormer, and P. Kim, "Observation of the fractional quantum Hall effect in graphene," *Nature*, vol. 462, pp. 196–199, Nov. 2009. (Cited on pages 2, 21, 22, 59 and 63)

[10] A. Sandner, T. Preis, C. Schell, P. Giudici, K. Watanabe, T. Taniguchi, D. Weiss, and J. Eroms, "Ballistic Transport in Graphene Antidot Lattices," *Nano Lett.*, vol. 15, pp. 8402–8406, Dec. 2015. (Cited on pages 2, 39, 67, 79, 80, 81, 84, 85, 89, 91 and 95)

[11] S. R. Power, M. R. Thomsen, A.-P. Jauho, and T. G. Pedersen, "Electron trajectories and magnetotransport in nanopatterned graphene under commensurability conditions," *Phys. Rev. B*, vol. 96, pp. 075425–, Aug. 2017. (Cited on pages 2, 67, 74, 75, 77, 79 and 104)

[12] M. Drienovsky, A. Sandner, C. Baumgartner, M.-H. Liu, T. Taniguchi, K. Watanabe, K. Richter, D. Weiss, and J. Eroms, "Few-layer graphene patterned bottom gates for can der Waals heterostructures," *eprint arXiv:1703.05631*, 2017. (Cited on pages 3, 47, 54, 56, 91, 92 and 94)

[13] D. Weiss, K. V. Klitzing, K. Ploog, and G. Weimann, "Magnetoresistance Oscillations in a Two-Dimensional Electron Gas Induced by a Submicrometer Periodic Potential," *EPL (Europhysics Letters)*, vol. 8, no. 2, pp. 179–, 1989. (Cited on pages 3, 39, 41, 81, 91, 94 and 98)

[14] D. Weiss, M. L. Roukes, A. Menschig, P. Grambow, K. von Klitzing, and G. Weimann, "Electron pinball and commensurate orbits in a periodic array of scatterers," *Phys. Rev. Lett.*, vol. 66, pp. 2790–2793, May 1991. (Cited on pages 3, 39, 44, 45, 69, 71, 72, 81, 85, 94 and 95)

[15] A. K. Geim and K. S. Novoselov, "The rise of graphene," *Nat Mater*, vol. 6, pp. 183–191, Mar. 2007. (Cited on pages 6, 9, 10, 11, 12 and 15)

[16] R. Saito, G. Dresselhaus, and M. S. Dresselhaus, *Physical Properties of Carbon Nanotubes*. Imperial College Press, 1999. (Cited on pages 6, 8 and 9)

[17] P. R. Wallace, "The Band Theory of Graphite," *Phys. Rev.*, vol. 71, pp. 622–634, May 1947. (Cited on pages 6 and 8)

[18] L. Landau and E. M. Lifshitz, *Statistical Physics*. Pergamon Press, Oxford, 1980. (Cited on page 6)

[19] K. S. Novoselov, A. K. Geim, S. V. Morozov, D. Jiang, Y. Zhang, S. V. Dubonos, I. V. Grigorieva, and A. A. Firsov, "Electric Field Effect in Atomically Thin Carbon Films," *Science*, vol. 306, no. 5696, pp. 666–669, 2004. (Cited on pages 7 and 11)

[20] J. R. Williams, *Electronic Transport in Graphene: p-n Junctions, Shot Noise, and Nanoribbons*. PhD thesis, Harvard University, 2009. (Cited on pages 8 and 9)

[21] A. F. Young, *Quantum Transport in Graphene Heterostructures*. PhD thesis, Columbia University, 2012. (Cited on pages 9, 59 and 61)

[22] D. R. Cooper, B. D'Anjou, N. Ghattamaneni, B. Harack, M. Hilke, A. Horth, N. Majlis, M. Massicotte, L. Vandsburger, E. Whiteway, and V. Yu, "Experimental review of graphene," 2012. (Cited on pages 9, 10, 13, 15, 16, 17, 19 and 22)

[23] D. W. Boukhvalov, M. I. Katsnelson, and A. I. Lichtenstein, "Hydrogen on graphene: Electronic structure, total energy, structural distortions and magnetism from first-principles calculations," *Phys. Rev. B*, vol. 77, pp. 035427–, Jan. 2008. (Cited on page 9)

[24] A. H. Castro Neto, F. Guinea, N. M. R. Peres, K. S. Novoselov, and A. K. Geim, "The electronic properties of graphene," *Rev. Mod. Phys.*, vol. 81, pp. 109–162, Jan. 2009. (Cited on pages 9 and 10)

[25] M. I. Katsnelson, "Graphene: Carbon in two dimensions," *Materials Today*, vol. 10, pp. 20–27, Jan. 2007. (Cited on pages 9 and 10)

[26] G. W. Semenoff, "Condensed-Matter Simulation of a Three-Dimensional Anomaly," *Phys. Rev. Lett.*, vol. 53, pp. 2449–2452, Dec. 1984. (Cited on page 9)

[27] Y. Zhang, Y.-W. Tan, H. L. Stormer, and P. Kim, "Experimental observation of the quantum Hall effect and Berry's phase in graphene," *Nature*, vol. 438, pp. 201–204, Nov. 2005. (Cited on pages 10 and 19)

[28] A. K. Geim and A. H. MacDonald, "Graphene: Exploring carbon flatland," *Physics Today, vol. 60, 8, pp35-41)*, 2007. (Cited on page 10)

[29] N. M. R. Peres, "Colloquium," *Rev. Mod. Phys.*, vol. 82, pp. 2673–2700, Sept. 2010. (Cited on pages 10 and 13)

[30] S. Das Sarma, S. Adam, E. H. Hwang, and E. Rossi, "Electronic transport in two-dimensional graphene," *Rev. Mod. Phys.*, vol. 83, pp. 407–470, May 2011. (Cited on pages 10 and 13)

[31] T. Ando, T. Nakanishi, and R. Saito, "Berry's Phase and Absence of Back Scattering in Carbon Nanotubes," *J. Phys. Soc. Jpn.*, vol. 67, pp. 2857–2862, Aug. 1998. (Cited on page 10)

[32] P. Kim, "Graphene and Relativistic Quantum Physics," in *Séminaire Poincaré XVIII*, 2014. (Cited on page 10)

[33] M. V. Berry, "Quantal phase factors accompanying adiabatic changes," *Proc R Soc Lond A Math Phys Sci*, vol. 392, pp. 45–, Mar. 1984. (Cited on page 10)

[34] J. Martin, N. Akerman, G. Ulbricht, T. Lohmann, J. H. Smet, K. von Klitzing, and A. Yacoby, "Observation of electron-hole puddles in graphene using a scanning single-electron transistor," *Nat Phys*, vol. 4, pp. 144–148, Feb. 2008. (Cited on pages 11, 12, 29 and 36)

[35] C. Dean, A. Young, L. Wang, I. Meric, G.-H. Lee, K. Watanabe, T. Taniguchi, K. Shepard, P. Kim, and J. Hone, "Graphene based heterostructures," *Solid State Commun.*, vol. 152, pp. 1275–1282, Aug. 2012. (Cited on pages 11, 29, 30 and 53)

[36] K. I. Bolotin, K. J. Sikes, J. Hone, H. L. Stormer, and P. Kim, "Temperature-Dependent Transport in Suspended Graphene," *Phys. Rev. Lett.*, vol. 101, pp. 096802–, Aug. 2008. (Cited on page 11)

[37] F. Oberhuber, *Untersuchung kristallographisch definierter Graphen-Ränder.* PhD thesis, Universität Regensburg, 2015. (Cited on page 11)

[38] B. Gelmont, M. Shur, and R. Mattauch, "Disk and stripe capacitances," *Solid-State Electronics*, vol. 38, pp. 731–734, Mar. 1995. (Cited on page 12)

[39] S. Minke, *Transport measurements on graphene.* PhD thesis, Universität Regensburg, 2012. (Cited on page 12)

[40] J. R. Williams, L. DiCarlo, and C. M. Marcus, "Quantum Hall Effect in a Gate-Controlled p-n Junction of Graphene," *Science*, vol. 317, pp. 638–, Aug. 2007. (Cited on page 12)

[41] A. F. Young and P. Kim, "Quantum interference and Klein tunnelling in graphene heterojunctions," *Nat Phys*, vol. 5, pp. 222–226, Mar. 2009. (Cited on pages 12, 23, 27 and 94)

[42] P. Rickhaus, R. Maurand, M.-H. Liu, M. Weiss, K. Richter, and C. Schönenberger, "Ballistic interferences in suspended graphene," *Nature Communications*, vol. 4, pp. 2342–, Aug. 2013. (Cited on pages 12, 56 and 94)

[43] J.-H. Chen, C. Jang, S. Adam, M. S. Fuhrer, E. D. Williams, and M. Ishigami, "Charged-impurity scattering in graphene," *Nat Phys*, vol. 4, pp. 377–381, May 2008. (Cited on pages 12, 15, 16 and 29)

[44] J.-H. Chen, W. G. Cullen, C. Jang, M. S. Fuhrer, and E. D. Williams, "Defect Scattering in Graphene," *Phys. Rev. Lett.*, vol. 102, p. 236805, Jun 2009. (Cited on pages 12 and 16)

[45] J.-H. Chen, C. Jang, S. Xiao, M. Ishigami, and M. S. Fuhrer, "Intrinsic and extrinsic performance limits of graphene devices on SiO2," *Nat Nano*, vol. 3, pp. 206–209, Apr. 2008. (Cited on page 13)

[46] A. N. Morozovska, E. A. Eliseev, and M. V. Strikha, "Ballistic conductivity of graphene channel with p-n junction at ferroelectric domain wall," *Appl. Phys. Lett.*, vol. 108, pp. 232902–, June 2016. (Cited on page 13)

[47] M. I. Katsnelson, "Zitterbewegung, chirality, and minimal conductivity in graphene," *The European Physical Journal B - Condensed Matter and Complex Systems*, vol. 51, no. 2, pp. 157–160, 2006. (Cited on page 13)

[48] D. K. Efetov and P. Kim, "Controlling Electron-Phonon Interactions in Graphene at Ultrahigh Carrier Densities," *Phys. Rev. Lett.*, vol. 105, pp. 256805–, Dec. 2010. (Cited on pages 14 and 15)

[49] E. H. Hwang and S. Das Sarma, "Acoustic phonon scattering limited carrier mobility in two-dimensional extrinsic graphene," *Phys. Rev. B*, vol. 77, pp. 115449–, Mar. 2008. (Cited on pages 14 and 65)

[50] T. Ando, "Screening Effect and Impurity Scattering in Monolayer Graphene," *J. Phys. Soc. Jpn.*, vol. 75, pp. 074716–, July 2006. (Cited on pages 14 and 29)

[51] S.-H. Ji, J. B. Hannon, R. M. Tromp, V. Perebeinos, J. Tersoff, and F. M. Ross, "Atomic-scale transport in epitaxial graphene," *Nat Mater*, vol. 11, pp. 114–119, Feb. 2012. (Cited on page 16)

[52] T. Stauber, N. M. R. Peres, and F. Guinea, "Electronic transport in graphene: A semiclassical approach including midgap states," *Phys. Rev. B*, vol. 76, pp. 205423–, Nov. 2007. (Cited on page 16)

[53] E. H. Hall, "On a New Action of the Magnet on Electric Currents," vol. 2, no. 3, pp. 287–292, 1879. (Cited on page 17)

[54] K. v. Klitzing, G. Dorda, and M. Pepper, "New Method for High-Accuracy Determination of the Fine-Structure Constant Based on Quantized Hall Resistance," *Phys. Rev. Lett.*, vol. 45, pp. 494–497, Aug. 1980. (Cited on page 17)

[55] Y. Zhao, *Quantum Hall Transport in Graphene and its Bilayer*. PhD thesis, Columbia University, 2012. (Cited on pages 17, 18 and 19)

[56] B. I. Halperin, "Quantized Hall conductance, current-carrying edge states, and the existence of extended states in a two-dimensional disordered potential," *Phys. Rev. B*, vol. 25, pp. 2185–2190, Feb. 1982. (Cited on page 18)

[57] M. Büttiker, "Absence of backscattering in the quantum Hall effect in multiprobe conductors," *Phys. Rev. B*, vol. 38, pp. 9375–9389, Nov. 1988. (Cited on page 19)

[58] N. M. R. Peres, F. Guinea, and A. H. Castro Neto, "Electronic properties of disordered two-dimensional carbon," *Phys. Rev. B*, vol. 73, pp. 125411–, Mar. 2006. (Cited on page 19)

[59] V. P. Gusynin and S. G. Sharapov, "Unconventional Integer Quantum Hall Effect in Graphene," *Phys. Rev. Lett.*, vol. 95, p. 146801, Sep 2005. (Cited on page 19)

[60] K. S. Novoselov, Z. Jiang, Y. Zhang, S. V. Morozov, H. L. Stormer, U. Zeitler, J. C. Maan, G. S. Boebinger, P. Kim, and A. K. Geim, "Room-Temperature Quantum Hall Effect in Graphene," *Science*, vol. 315, pp. 1379–, Mar. 2007. (Cited on page 20)

[61] K. Nomura and A. H. MacDonald, "Quantum Hall Ferromagnetism in Graphene," *Phys. Rev. Lett.*, vol. 96, pp. 256602–, June 2006. (Cited on pages 20, 21 and 59)

[62] M. O. Goerbig, "Electronic properties of graphene in a strong magnetic field," *Rev. Mod. Phys.*, vol. 83, pp. 1193–1243, Nov. 2011. (Cited on page 20)

[63] Y. Zhang, Z. Jiang, J. P. Small, M. S. Purewal, Y.-W. Tan, M. Fazlollahi, J. D. Chudow, J. A. Jaszczak, H. L. Stormer, and P. Kim, "Landau-Level Splitting in Graphene in High Magnetic Fields," *Phys. Rev. Lett.*, vol. 96, pp. 136806–, Apr. 2006. (Cited on pages 21 and 59)

[64] X. Du, I. Skachko, F. Duerr, A. Luican, and E. Y. Andrei, "Fractional quantum Hall effect and insulating phase of Dirac electrons in graphene," *Nature*, vol. 462, pp. 192–195, Nov. 2009. (Cited on page 21)

[65] D. A. Abanin, B. E. Feldman, A. Yacoby, and B. I. Halperin, "Fractional and integer quantum Hall effects in the zeroth Landau level in graphene," *Phys. Rev. B*, vol. 88, pp. 115407–, Sept. 2013. (Cited on pages 21, 22 and 63)

[66] A. J. M. Giesbers, L. A. Ponomarenko, K. S. Novoselov, A. K. Geim, M. I. Katsnelson, J. C. Maan, and U. Zeitler, "Gap opening in the zeroth Landau level of graphene," *Phys. Rev. B*, vol. 80, pp. 201403–, Nov. 2009. (Cited on page 21)

[67] J. Alicea and M. P. A. Fisher, "Graphene integer quantum Hall effect in the ferromagnetic and paramagnetic regimes," *Phys. Rev. B*, vol. 74, p. 075422, Aug 2006. (Cited on page 21)

[68] J. Jung and A. H. MacDonald, "Theory of the magnetic-field-induced insulator in neutral graphene sheets," *Phys. Rev. B*, vol. 80, p. 235417, Dec 2009. (Cited on page 21)

[69] M. Yankowitz, J. Xue, and B. J. LeRoy, "Graphene on hexagonal boron nitride," *Journal of Physics: Condensed Matter*, vol. 26, no. 30, pp. 303201–, 2014. (Cited on pages 21, 22 and 31)

[70] J. G. Checkelsky, L. Li, and N. P. Ong, "Zero-Energy State in Graphene in a High Magnetic Field," *Phys. Rev. Lett.*, vol. 100, pp. 206801–, May 2008. (Cited on page 21)

[71] C. Töke, P. E. Lammert, V. H. Crespi, and J. K. Jain, "Fractional quantum Hall effect in graphene," *Phys. Rev. B*, vol. 74, pp. 235417–, Dec. 2006. (Cited on page 22)

[72] M. O. Goerbig and N. Regnault, "Analysis of a SU(4) generalization of Halperin's wave function as an approach towards a SU(4) fractional quantum Hall effect in graphene sheets," *Phys. Rev. B*, vol. 75, pp. 241405–, June 2007. (Cited on page 22)

[73] J. K. Jain, *Composite Fermions*. New York: Cambridge University Press, 2007. (Cited on page 22)

[74] B. E. Feldman, B. Krauss, J. H. Smet, and A. Yacoby, "Unconventional Sequence of Fractional Quantum Hall States in Suspended Graphene," *Science*, vol. 337, pp. 1196–1199, Sept. 2012. (Cited on pages 22 and 63)

[75] E. H. Hwang, S. Adam, and S. D. Sarma, "Carrier Transport in Two-Dimensional Graphene Layers," *Phys. Rev. Lett.*, vol. 98, pp. 186806–, May 2007. (Cited on pages 22 and 29)

[76] S. Chen, Z. Han, M. M. Elahi, K. M. M. Habib, L. Wang, B. Wen, Y. Gao, T. Taniguchi, K. Watanabe, J. Hone, A. W. Ghosh, and C. R. Dean, "Electron optics with p-n junctions in ballistic graphene," *Science*, vol. 353, pp. 1522–, Sept. 2016. (Cited on pages 22 and 56)

[77] P. Rickhaus, *Electron Optics in Ballistic Graphene*. PhD thesis, Universität Basel, 2015. (Cited on pages 22, 23, 24, 25 and 27)

[78] V. G. Veselago, "The Electrodynamics of Substances With Simultaneously Negative Values Of $\epsilon$ And $\mu$," *Sov. Phys. Usp. 10, 509-514*, 1968. (Cited on page 23)

[79] V. V. Cheianov, V. Fal'ko, and B. L. Altshuler, "The Focusing of Electron Flow and a Veselago Lens in Graphene p-n Junctions," *Science*, vol. 315, pp. 1252–, Mar. 2007. (Cited on pages 23 and 54)

[80] O. Klein, "Die Reflexion von Elektronen an einem Potentialsprung nach der relativistischen Dynamik von Dirac," *Zeitschrift für Physik*, vol. 53, no. 3, pp. 157–165, 1929. (Cited on page 23)

[81] M. Katsnelson and K. Novoselov, "Graphene: New bridge between condensed matter physics and quantum electrodynamics," *Solid State Communications*, vol. 143, pp. 3–13, July 2007. (Cited on pages 23 and 24)

[82] F. Sauter, "Zum Kleinschen Paradoxon," *Zeitschrift für Physik*, vol. 73, no. 7, pp. 547–552, 1932. (Cited on pages 23 and 26)

[83] M. I. Katsnelson, K. S. Novoselov, and A. K. Geim, "Chiral tunnelling and the Klein paradox in graphene," *Nat Phys*, vol. 2, pp. 620–625, Sept. 2006. (Cited on pages 23, 25 and 54)

[84] B. Huard, J. A. Sulpizio, N. Stander, K. Todd, B. Yang, and D. Goldhaber-Gordon, "Transport Measurements Across a Tunable Potential Barrier in Graphene," *Phys. Rev. Lett.*, vol. 98, pp. 236803–, June 2007. (Cited on page 23)

[85] R. V. Gorbachev, A. S. Mayorov, A. K. Savchenko, D. W. Horsell, and F. Guinea, "Conductance of p-n-p Graphene Structures with "Air-Bridge" Top Gates," *Nano Lett.*, vol. 8, pp. 1995–1999, July 2008. (Cited on page 23)

[86] I. Meric, M. Y. Han, A. F. Young, B. Ozyilmaz, P. Kim, and K. L. Shepard, "Current saturation in zero-bandgap, top-gated graphene field-effect transistors," *Nat Nano*, vol. 3, pp. 654–659, Nov. 2008. (Cited on page 24)

[87] P. E. Allain and J. N. Fuchs, “Klein tunneling in graphene: optics with massless electrons,” *The European Physical Journal B*, vol. 83, no. 3, pp. 301–, 2011. (Cited on page 24)

[88] V. V. Cheianov and V. I. Fal’ko, “Selective transmission of Dirac electrons and ballistic magnetoresistance of n-p junctions in graphene,” *Phys. Rev. B*, vol. 74, pp. 041403–, July 2006. (Cited on pages 25, 26, 27, 54 and 96)

[89] M.-H. Liu, J. Bundesmann, and K. Richter, “Spin-dependent Klein tunneling in graphene: Role of Rashba spin-orbit coupling,” *Phys. Rev. B*, vol. 85, pp. 085406–, Feb. 2012. (Cited on page 26)

[90] P. Rickhaus, P. Makk, M.-H. Liu, E. Tovari, M. Weiss, R. Maurand, K. Richter, and C. Schönenberger, “Snake trajectories in ultraclean graphene pn junctions,” *Nat Commun*, vol. 6, pp. –, Mar. 2015. (Cited on pages 26 and 27)

[91] C. W. J. Beenakker, “Colloquium,” *Rev. Mod. Phys.*, vol. 80, pp. 1337–1354, Oct 2008. (Cited on pages 27 and 28)

[92] J. P. Bird, R. Akis, D. K. Ferry, D. Vasileska, J. Cooper, Y. Aoyagi, and T. Sugano, “Lead-Orientation-Dependent Wave Function Scarring in Open Quantum Dots,” *Phys. Rev. Lett.*, vol. 82, pp. 4691–4694, June 1999. (Cited on page 27)

[93] A. V. Shytov, N. Gu, and L. S. Levitov, “Transport in Graphene p-n Junctions in Magnetic Field,” *e-print arXiv:0708.3081*, 2007. (Cited on pages 27 and 96)

[94] V. Lukose, R. Shankar, and G. Baskaran, “Novel Electric Field Effects on Landau Levels in Graphene,” *Phys. Rev. Lett.*, vol. 98, pp. 116802–, Mar. 2007. (Cited on page 28)

[95] K. Bolotin, K. Sikes, Z. Jiang, M. Klima, G. Fudenberg, J. Hone, P. Kim, and H. Stormer, “Ultrahigh electron mobility in suspended graphene,” *Solid State Communications*, vol. 146, pp. 351–355, June 2008. (Cited on page 29)

[96] G. Giovannetti, P. A. Khomyakov, G. Brocks, P. J. Kelly, and J. van den Brink, “Substrate-induced band gap in graphene on hexagonal boron nitride: Ab initio density functional calculations,” *Phys. Rev. B*, vol. 76, pp. 073103–, Aug. 2007. (Cited on page 30)

[97] J. Xue, J. Sanchez-Yamagishi, D. Bulmash, P. Jacquod, A. Deshpande, K. Watanabe, T. Taniguchi, P. Jarillo-Herrero, and B. J. LeRoy, “Scanning tunnelling microscopy and spectroscopy of ultra-flat graphene on hexagonal

boron nitride," *Nat Mater*, vol. 10, pp. 282–285, Apr. 2011. (Cited on pages 30, 31 and 81)

[98] L. Wang, I. Meric, P. Y. Huang, Q. Gao, Y. Gao, H. Tran, T. Taniguchi, K. Watanabe, L. M. Campos, D. A. Muller, J. Guo, P. Kim, J. Hone, K. L. Shepard, and C. R. Dean, "One-Dimensional Electrical Contact to a Two-Dimensional Material," *Science*, vol. 342, no. 6158, pp. 614–617, 2013. (Cited on pages 30, 33, 53, 56, 61, 68, 69, 80 and 92)

[99] L. Britnell, R. V. Gorbachev, R. Jalil, B. D. Belle, F. Schedin, A. Mishchenko, T. Georgiou, M. I. Katsnelson, L. Eaves, S. V. Morozov, N. M. R. Peres, J. Leist, A. K. Geim, K. S. Novoselov, and L. A. Ponomarenko, "Field-Effect Tunneling Transistor Based on Vertical Graphene Heterostructures," *Science*, vol. 335, pp. 947–950, Feb. 2012. (Cited on pages 30 and 32)

[100] R. V. Gorbachev, A. K. Geim, M. I. Katsnelson, K. S. Novoselov, T. Tudorovskiy, I. V. Grigorieva, A. H. MacDonald, S. V. Morozov, K. Watanabe, T. Taniguchi, and L. A. Ponomarenko, "Strong Coulomb drag and broken symmetry in double-layer graphene," *Nat Phys*, vol. 8, pp. 896–901, Dec. 2012. (Cited on pages 30 and 32)

[101] P. Kim, "Bloch, Landau, and Dirac: Hofstadter's Butterfly in Graphene," in *School on Modern Topics in Condensed Matter Physics, NTU Singapore*, 2013. (Cited on page 30)

[102] S. J. Haigh, A. Gholinia, R. Jalil, S. Romani, L. Britnell, D. C. Elias, K. S. Novoselov, L. A. Ponomarenko, A. K. Geim, and R. Gorbachev, "Cross-sectional imaging of individual layers and buried interfaces of graphene-based heterostructures and superlattices," *Nat Mater*, vol. 11, no. 9, pp. 764–767, 2012. (Cited on pages 31 and 32)

[103] K. S. Novoselov, A. Mishchenko, A. Carvalho, and A. H. Castro Neto, "2D materials and van der Waals heterostructures," *Science*, vol. 353, pp. –, July 2016. (Cited on pages 31 and 33)

[104] A. V. Kretinin, Y. Cao, J. S. Tu, G. L. Yu, R. Jalil, K. S. Novoselov, S. J. Haigh, A. Gholinia, A. Mishchenko, M. Lozada, T. Georgiou, C. R. Woods, F. Withers, P. Blake, G. Eda, A. Wirsig, C. Hucho, K. Watanabe, T. Taniguchi, A. K. Geim, and R. V. Gorbachev, "Electronic Properties of Graphene Encapsulated with Different Two-Dimensional Atomic Crystals," *Nano Lett.*, vol. 14, pp. 3270–3276, May 2014. (Cited on pages 31 and 54)

[105] L. Banszerus, M. Schmitz, S. Engels, M. Goldsche, K. Watanabe, T. Taniguchi, B. Beschoten, and C. Stampfer, "Ballistic Transport Ex-

ceeding $\mu$m in CVD Grown Graphene," *Nano Lett.*, vol. 16, pp. 1387–1391, Feb. 2016. (Cited on pages 33 and 48)

[106] M. Xu, T. Liang, M. Shi, and H. Chen, "Graphene-Like Two-Dimensional Materials," *Chem. Rev.*, vol. 113, pp. 3766–3798, May 2013. (Cited on page 33)

[107] A. K. Geim and I. V. Grigorieva, "Van der Waals heterostructures," *Nature*, vol. 499, no. 7459, pp. 419–425, 2013. (Cited on page 33)

[108] C.-H. Park, L. Yang, Y.-W. Son, M. L. Cohen, and S. G. Louie, "New Generation of Massless Dirac Fermions in Graphene under External Periodic Potentials," *Phys. Rev. Lett.*, vol. 101, pp. 126804–, Sept. 2008. (Cited on page 33)

[109] M. Barbier, F. M. Peeters, P. Vasilopoulos, and J. M. Pereira, "Dirac and Klein-Gordon particles in one-dimensional periodic potentials," *Phys. Rev. B*, vol. 77, pp. 115446–, Mar. 2008. (Cited on page 33)

[110] P. Burset, A. L. Yeyati, L. Brey, and H. A. Fertig, "Transport in superlattices on single-layer graphene," *Phys. Rev. B*, vol. 83, pp. 195434–, May 2011. (Cited on page 33)

[111] M. Yankowitz, J. Xue, D. Cormode, J. D. Sanchez-Yamagishi, K. Watanabe, T. Taniguchi, P. Jarillo-Herrero, P. Jacquod, and B. J. LeRoy, "Emergence of superlattice Dirac points in graphene on hexagonal boron nitride," *Nat Phys*, vol. 8, pp. 382–386, May 2012. (Cited on pages 33, 34, 35, 80 and 82)

[112] G. L. Yu, R. V. Gorbachev, J. S. Tu, A. V. Kretinin, Y. Cao, R. Jalil, F. Withers, L. A. Ponomarenko, B. A. Piot, M. Potemski, D. C. Elias, X. Chen, K. Watanabe, T. Taniguchi, I. V. Grigorieva, K. S. Novoselov, V. I. Fal/'ko, A. K. Geim, and A. Mishchenko, "Hierarchy of Hofstadter states and replica quantum Hall ferromagnetism in graphene superlattices," *Nat Phys*, vol. 10, pp. 525–529, July 2014. (Cited on pages 34, 35, 38 and 85)

[113] C. R. Dean, L. Wang, P. Maher, C. Forsythe, F. Ghahari, Y. Gao, J. Katoch, M. Ishigami, P. Moon, M. Koshino, T. Taniguchi, K. Watanabe, K. L. Shepard, J. Hone, and P. Kim, "Hofstadter/'s butterfly and the fractal quantum Hall effect in moire superlattices," *Nature*, vol. 497, pp. 598–602, May 2013. (Cited on pages 35, 37, 38, 69, 81, 82 and 85)

[114] J. Jung, A. M. DaSilva, A. H. MacDonald, and S. Adam, "Origin of band gaps in graphene on hexagonal boron nitride," *Nature Communications*, vol. 6, pp. 6308–, Feb. 2015. (Cited on page 35)

[115] B. Hunt, J. D. Sanchez-Yamagishi, A. F. Young, M. Yankowitz, B. J. LeRoy, K. Watanabe, T. Taniguchi, P. Moon, M. Koshino, P. Jarillo-Herrero, and R. C. Ashoori, “Massive Dirac Fermions and Hofstadter Butterfly in a van der Waals Heterostructure,” *Science*, vol. 340, pp. 1427–1430, June 2013. (Cited on pages 35, 37, 38, 56, 80, 81 and 82)

[116] L. Wang, Y. Gao, B. Wen, Z. Han, T. Taniguchi, K. Watanabe, M. Koshino, J. Hone, and C. R. Dean, “Evidence for a fractional fractal quantum Hall effect in graphene superlattices,” *Science*, vol. 350, pp. 1231–, Dec. 2015. (Cited on page 35)

[117] L. A. Ponomarenko, R. V. Gorbachev, G. L. Yu, D. C. Elias, R. Jalil, A. A. Patel, A. Mishchenko, A. S. Mayorov, C. R. Woods, J. R. Wallbank, M. Mucha-Kruczynski, B. A. Piot, M. Potemski, I. V. Grigorieva, K. S. Novoselov, F. Guinea, V. I. Fal/’ko, and A. K. Geim, “Cloning of Dirac fermions in graphene superlattices,” *Nature*, vol. 497, pp. 594–597, May 2013. (Cited on pages 35, 38, 69, 80, 81 and 82)

[118] C. R. Woods, L. Britnell, A. Eckmann, R. S. Ma, J. C. Lu, H. M. Guo, X. Lin, G. L. Yu, Y. Cao, R. V. Gorbachev, A. V. Kretinin, J. Park, L. A. Ponomarenko, M. I. Katsnelson, Y. N. Gornostyrev, K. Watanabe, T. Taniguchi, C. Casiraghi, H.-J. Gao, A. K. Geim, and K. S. Novoselov, “Commensurate-incommensurate transition in graphene on hexagonal boron nitride,” *Nat Phys*, vol. 10, pp. 451–456, June 2014. (Cited on pages 36 and 81)

[119] R. V. Gorbachev, J. C. W. Song, G. L. Yu, A. V. Kretinin, F. Withers, Y. Cao, A. Mishchenko, I. V. Grigorieva, K. S. Novoselov, L. S. Levitov, and A. K. Geim, “Detecting topological currents in graphene superlattices,” *Science*, vol. 346, pp. 448–451, Oct. 2014. (Cited on page 36)

[120] G. Yu, *Transport Propterties Of Graphene Based Van Der Waals Heterostructures*. PhD thesis, University of Manchester, 2015. (Cited on page 36)

[121] D. Pfannkuche and R. R. Gerhardts, “Theory of magnetotransport in two-dimensional electron systems subjected to weak two-dimensional superlattice potentials,” *Phys. Rev. B*, vol. 46, pp. 12606–12626, Nov. 1992. (Cited on pages 36, 94 and 98)

[122] D. R. Hofstadter, “Energy levels and wave functions of Bloch electrons in rational and irrational magnetic fields,” *Phys. Rev. B*, vol. 14, pp. 2239–2249, Sept. 1976. (Cited on pages 36, 37, 43 and 81)

[123] D. Weiss, "Kommensurabilitätseffekte in lateralen Übergittern." Habilitationsschrift, Max-Planck-Institut für Festkörperforschung, Stuttgart, 1992. (Cited on pages 37, 40, 42, 44 and 100)

[124] D. Weiss, "Solid-state physics: The butterfly emerges," *Nat Phys*, vol. 9, pp. 395–396, July 2013. (Cited on page 37)

[125] C. Albrecht, J. H. Smet, K. von Klitzing, D. Weiss, V. Umansky, and H. Schweizer, "Evidence of Hofstadter's Fractal Energy Spectrum in the Quantized Hall Conductance," *Phys. Rev. Lett.*, vol. 86, pp. 147–150, Jan. 2001. (Cited on page 37)

[126] T. Schlösser, K. Ensslin, J. P. Kotthaus, and M. Holland, "Internal structure of a Landau band induced by a lateral superlattice: a glimpse of Hofstadter's butterfly," *EPL (Europhysics Letters)*, vol. 33, no. 9, pp. 683–, 1996. (Cited on page 37)

[127] G. H. Wannier, "A Result Not Dependent on Rationality for Bloch Electrons in a Magnetic Field," *physica status solidi (b)*, vol. 88, no. 2, pp. 757–765, 1978. (Cited on page 38)

[128] G. Chen, M. Sui, D. Wang, S. Wang, J. Jung, P. Moon, S. Adam, K. Watanabe, T. Taniguchi, S. Zhou, M. Koshino, G. Zhang, and Y. Zhang, "Emergence of Tertiary Dirac Points in Graphene Moiré Superlattices," *Nano Lett.*, vol. 17, pp. 3576–3581, June 2017. (Cited on page 38)

[129] R. W. Winkler, J. P. Kotthaus, and K. Ploog, "Landau band conductivity in a two-dimensional electron system modulated by an artificial one-dimensional superlattice potential," *Phys. Rev. Lett.*, vol. 62, pp. 1177–1180, Mar. 1989. (Cited on pages 39, 40, 91, 94 and 98)

[130] R. Schuster and K. Ensslin, "Antidot superlattices: Classical chaos and quantum transport," in *Festkörperprobleme 34*, pp. 195–218, Berlin, Heidelberg: Springer Berlin Heidelberg, 1994. (Cited on pages 39 and 94)

[131] R. Yagi, R. Sakakibara, R. Ebisuoka, J. Onishi, K. Watanabe, T. Taniguchi, and Y. Iye, "Ballistic transport in graphene antidot lattices," *Phys. Rev. B*, vol. 92, pp. 195406–, Nov. 2015. (Cited on pages 39, 69, 79, 81, 85 and 91)

[132] R. R. Gerhardts, D. Weiss, and K. v. Klitzing, "Novel magnetoresistance oscillations in a periodically modulated two-dimensional electron gas," *Phys. Rev. Lett.*, vol. 62, pp. 1173–1176, Mar 1989. (Cited on pages 40, 41, 42 and 98)

[133] D. Weiss, “Magneto-quantum transport in 2D-electron systems with periodic modulation,” *Physica Scripta*, vol. 1991, no. T35, pp. 226–, 1991. (Cited on pages 40, 43 and 44)

[134] Y. Iye, “Electric and Magnetic Lateral Superlattices,” in *Mesoscopic Physics and Electronics*, pp. 90–95, Berlin, Heidelberg: Springer Berlin Heidelberg, 1998. (Cited on page 41)

[135] D. Weiss, “Lateral superlattices: Magnetoresistance, hall effect and commensurate orbits,” in *Festkörperprobleme 31: Plenary Lectures of the Divisions Semiconductor Physics Thin Films Dynamics and Statistical Physics Magnetism Metal Physics Surface Physics Low Temperature Physics of the German Physical Society (DPG), Münster, April 8 to 12, 1991*, pp. 341–356, Berlin, Heidelberg: Springer Berlin Heidelberg, 1991. (Cited on pages 41 and 42)

[136] P. H. Beton, P. C. Main, M. Davison, M. Dellow, R. P. Taylor, E. S. Alves, L. Eaves, S. P. Beaumont, and C. D. W. Wilkinson, “Temperature dependence of magnetoresistance oscillations in a two-dimensional electron gas subjected to a periodic potential,” *Phys. Rev. B*, vol. 42, pp. 9689–9692, Nov 1990. (Cited on pages 41 and 101)

[137] T. Ando and Y. Uemura, “Theory of Quantum Transport in a Two-Dimensional Electron System under Magnetic Fields. I. Characteristics of Level Broadening and Transport under Strong Fields,” *J. Phys. Soc. Jpn.*, vol. 36, pp. 959–967, Apr. 1974. (Cited on page 42)

[138] C. W. J. Beenakker, “Guiding-center-drift resonance in a periodically modulated two-dimensional electron gas,” *Phys. Rev. Lett.*, vol. 62, pp. 2020–2023, Apr. 1989. (Cited on page 42)

[139] C. Beenakker and H. van Houten, “Quantum Transport in Semiconductor Nanostructures,” *Solid State Physics*, vol. 44, pp. 1–228, 1991. (Cited on pages 42 and 94)

[140] P. G. Harper, “Single Band Motion of Conduction Electrons in a Uniform Magnetic Field,” *Proceedings of the Physical Society. Section A*, vol. 68, no. 10, pp. 874–, 1955. (Cited on page 43)

[141] R. R. Gerhardts, D. Weiss, and U. Wulf, “Magnetoresistance oscillations in a grid potential: Indication of a Hofstadter-type energy spectrum,” *Phys. Rev. B*, vol. 43, pp. 5192–5195, Feb 1991. (Cited on pages 43 and 44)

[142] E. S. Alves, P. H. Beton, M. Henini, L. Eaves, P. C. Main, O. H. Hughes, G. A. Toombs, S. P. Beaumont, and C. D. W. Wilkinson, “The oscillatory magnetoresistance of electrons in a square superlattice potential,” *Journal*

*of Physics: Condensed Matter*, vol. 1, no. 43, pp. 8257–, 1989. (Cited on page 44)

[143] H. Fang and P. J. Stiles, "Novel magnetoresistance oscillations in a two-dimensional superlattice potential," *Phys. Rev. B*, vol. 41, pp. 10171–10174, May 1990. (Cited on page 44)

[144] A. Lorke, J. P. Kotthaus, and K. Ploog, "Magnetotransport in two-dimensional lateral superlattices," *Phys. Rev. B*, vol. 44, pp. 3447–3450, Aug 1991. (Cited on page 44)

[145] R. Fleischmann, T. Geisel, and R. Ketzmerick, "Quenched and Negative Hall Effect in Periodic Media: Application to Antidot Superlattices," *EPL (Europhysics Letters)*, vol. 25, no. 3, pp. 219–, 1994. (Cited on page 44)

[146] T. Ando, S. Uryu, and S. Ishizaka, "Chaos and Quantum Transport in Antidot Lattices," *Japanese Journal of Applied Physics*, vol. 38, no. 1S, pp. 308–, 1999. (Cited on page 44)

[147] F. Nihey and K. Nakamura, "Aharonov-Bohm effect in antidot structures," *Physica B: Condensed Matter*, vol. 184, no. 1, pp. 398–402, 1993. (Cited on pages 44 and 100)

[148] D. Weiss, K. Richter, A. Menschig, R. Bergmann, H. Schweizer, K. von Klitzing, and G. Weimann, "Quantized periodic orbits in large antidot arrays," *Phys. Rev. Lett.*, vol. 70, pp. 4118–4121, June 1993. (Cited on pages 44 and 100)

[149] D. Weiss, G. Lütjering, and K. Richter, "Chaotic Electron Motion in Macroscopic and Mesoscopic Antidot Lattices," *Chaos, Solitons & Fractals*, vol. 8, no. 7, pp. 1337–1357, 1997. (Cited on pages 45 and 46)

[150] M. Berry, "Quantizing a classically ergodic system: Sinai's billiard and the KKR method," *Annals of Physics*, vol. 131, no. 1, pp. 163–216, 1981. (Cited on page 46)

[151] G. Datseris, R. Fleischmann, and T. Geisel Master's thesis, MPI for Dynamics and Self-Organization, Göttingen, 2016. (Cited on pages 46 and 67)

[152] R. Fleischmann, T. Geisel, and R. Ketzmerick, "Magnetoresistance due to chaos and nonlinear resonances in lateral surface superlattices," *Phys. Rev. Lett.*, vol. 68, pp. 1367–1370, Mar 1992. (Cited on pages 46, 71, 94, 95 and 96)

[153] E. M. Baskin, G. M. Gusev, Z. D. Kvon, A. G. Pogosov, and M. V. Entin, "Stochastic dynamics of 2d electrons in a periodic lattice of antidots," *JETP Lett.*, vol. 55, no. 11, p. 678, 1992. (Cited on page 46)

[154] T. Wu, X. Zhang, Q. Yuan, J. Xue, G. Lu, Z. Liu, H. Wang, H. Wang, F. Ding, Q. Yu, X. Xie, and M. Jiang, "Fast growth of inch-sized single-crystalline graphene from a controlled single nucleus on Cu-Ni alloys," *Nat Mater*, vol. 15, pp. 43–47, Jan. 2016. (Cited on page 48)

[155] K. Watanabe, T. Taniguchi, and H. Kanda, "Direct-bandgap properties and evidence for ultraviolet lasing of hexagonal boron nitride single crystal," *Nat Mater*, vol. 3, no. 6, pp. 404–409, 2004. (Cited on page 48)

[156] P. Blake, E. W. Hill, A. H. Castro Neto, K. S. Novoselov, D. Jiang, R. Yang, T. J. Booth, and A. K. Geim, "Making graphene visible," *Appl. Phys. Lett.*, vol. 91, pp. 063124–, Aug. 2007. (Cited on page 48)

[157] M. Drienovsky, "Ballistic transport in density modulated graphene," tech. rep., Talk at University of Basel, 2016. (Cited on page 50)

[158] A. G. F. Garcia, M. Neumann, F. Amet, J. R. Williams, K. Watanabe, T. Taniguchi, and D. Goldhaber-Gordon, "Effective Cleaning of Hexagonal Boron Nitride for Graphene Devices," *Nano Lett.*, vol. 12, pp. 4449–4454, Aug. 2012. (Cited on page 53)

[159] C. Gong, H. C. Floresca, D. Hinojos, S. McDonnell, X. Qin, Y. Hao, S. Jandhyala, G. Mordi, J. Kim, L. Colombo, R. S. Ruoff, M. J. Kim, K. Cho, R. M. Wallace, and Y. J. Chabal, "Rapid Selective Etching of PMMA Residues from Transferred Graphene by Carbon Dioxide," *J. Phys. Chem. C*, vol. 117, pp. 23000–23008, Oct. 2013. (Cited on pages 53 and 54)

[160] D. Wang, G. Chen, C. Li, M. Cheng, W. Yang, S. Wu, G. Xie, J. Zhang, J. Zhao, X. Lu, P. Chen, G. Wang, J. Meng, J. Tang, R. Yang, C. He, D. Liu, D. Shi, K. Watanabe, T. Taniguchi, J. Feng, Y. Zhang, and G. Zhang, "Thermally Induced Graphene Rotation on Hexagonal Boron Nitride," *Phys. Rev. Lett.*, vol. 116, pp. 126101–, Mar. 2016. (Cited on page 54)

[161] J. Baringhaus, A. Stöhr, S. Forti, U. Starke, and C. Tegenkamp, "Ballistic bipolar junctions in chemically gated graphene ribbons," *Scientific Reports*, vol. 5, pp. 9955–, Apr. 2015. (Cited on page 54)

[162] N. Tombros, A. Veligura, J. Junesch, M. H. D. Guimaraes, I. J. Vera-Marun, H. T. Jonkman, and B. J. van Wees, "Quantized conductance of a suspended graphene nanoconstriction," *Nat Phys*, vol. 7, pp. 697–700, Sept. 2011. (Cited on page 54)

[163] B. Fallahazad, S. Kim, L. Colombo, and E. Tutuc, "Dielectric thickness dependence of carrier mobility in graphene with HfO2 top dielectric," *Applied Physics Letters*, vol. 97, no. 12, p. 123105, 2010. (Cited on page 54)

[164] L. A. Ponomarenko, A. K. Geim, A. A. Zhukov, R. Jalil, S. V. Morozov, K. S. Novoselov, I. V. Grigorieva, E. H. Hill, V. V. Cheianov, V. I. Fal/'ko, K. Watanabe, T. Taniguchi, and R. V. Gorbachev, "Tunable metal-insulator transition in double-layer graphene heterostructures," *Nat Phys*, vol. 7, pp. 958–961, Dec. 2011. (Cited on page 56)

[165] A. L. Grushina, D.-K. Ki, and A. F. Morpurgo, "A ballistic pn junction in suspended graphene with split bottom gates," *Applied Physics Letters*, vol. 102, no. 22, p. 223102, 2013. (Cited on page 56)

[166] F. Amet, *Novel Phenomena Driven By Interactions And Symmetry Breaking In Graphene*. PhD thesis, Standford University, 2014. (Cited on page 56)

[167] X.-G. Wen, "Topological orders and edge excitations in fractional quantum Hall states," *Advances in Physics*, vol. 44, pp. 405–473, Oct. 1995. (Cited on page 59)

[168] C. Schell, "Transportuntersuchungen an Graphenschichten auf Bornitrid-Substrat," Master's thesis, Universität Regensburg, 2012. (Cited on page 59)

[169] A.-M. Lang, "AFM Charakterisierung der Nanostrukturierung von Graphen." Bachelor thesis, 09 2014. (Cited on page 60)

[170] T. Lindner, "AFM Charakterisierung eines CO2 basierten Reinigungsprozesses für strukturiertes Graphen." Bachelor thesis, 01 2015. (Cited on page 60)

[171] H. van Houten, C. W. J. Beenakker, J. G. Williamson, M. E. I. Broekaart, P. H. M. van Loosdrecht, B. J. van Wees, J. E. Mooij, C. T. Foxon, and J. J. Harris, "Coherent electron focusing with quantum point contacts in a two-dimensional electron gas," *Phys. Rev. B*, vol. 39, pp. 8556–8575, Apr. 1989. (Cited on page 64)

[172] L. P. Rokhinson, V. Larkina, Y. B. Lyanda-Geller, L. N. Pfeiffer, and K. W. West, "Spin Separation in Cyclotron Motion," *Phys. Rev. Lett.*, vol. 93, p. 146601, Sep 2004. (Cited on page 64)

[173] V. J. Goldman, B. Su, and J. K. Jain, "Detection of composite fermions by magnetic focusing," *Phys. Rev. Lett.*, vol. 72, pp. 2065–2068, Mar. 1994. (Cited on page 64)

[174] T. Taychatanapat, K. Watanabe, T. Taniguchi, and P. Jarillo-Herrero, “Electrically tunable transverse magnetic focusing in graphene,” *Nat Phys*, vol. 9, pp. 225–229, Apr. 2013. (Cited on pages 64, 65 and 68)

[175] T. Taniguchi and K. Watanabe, “Synthesis of high-purity boron nitride single crystals under high pressure by using Ba-BN solvent,” *J. Cryst. Growth*, vol. 303, no. 2, pp. 525 – 529, 2007. (Cited on page 68)

[176] V. E. Calado, S.-E. Zhu, S. Goswami, Q. Xu, K. Watanabe, T. Taniguchi, G. C. A. M. Janssen, and L. M. K. Vandersypen, “Ballistic transport in graphene grown by chemical vapor deposition,” *Appl. Phys. Lett.*, vol. 104, no. 2, p. 023103, 2014. (Cited on page 68)

[177] C. Stampfer, J. Güttinger, S. Hellmüller, F. Molitor, K. Ensslin, and T. Ihn, “Energy Gaps in Etched Graphene Nanoribbons,” *Phys. Rev. Lett.*, vol. 102, p. 056403, Feb 2009. (Cited on page 68)

[178] J.-M. Poumirol, A. Cresti, S. Roche, W. Escoffier, M. Goiran, X. Wang, X. Li, H. Dai, and B. Raquet, “Edge magnetotransport fingerprints in disordered graphene nanoribbons,” *Phys. Rev. B*, vol. 82, p. 041413, Jul 2010. (Cited on page 68)

[179] S. Minke, S. H. Jhang, J. Wurm, Y. Skourski, J. Wosnitza, C. Strunk, D. Weiss, K. Richter, and J. Eroms, “Magnetotransport through graphene nanoribbons at high magnetic fields,” *Phys. Rev. B*, vol. 85, p. 195432, May 2012. (Cited on page 68)

[180] D. Bischoff, T. Krähenmann, S. Dröscher, M. A. Gruner, C. Barraud, T. Ihn, and K. Ensslin, “Reactive-ion-etched graphene nanoribbons on a hexagonal boron nitride substrate,” *Appl. Phys. Lett.*, vol. 101, no. 20, p. 203103, 2012. (Cited on page 68)

[181] L. Jiao, L. Zhang, X. Wang, G. Diankov, and H. Dai, “Narrow graphene nanoribbons from carbon nanotubes,” *Nature*, vol. 458, pp. 877–880, Apr. 2009. (Cited on page 68)

[182] D. V. Kosynkin, A. L. Higginbotham, A. Sinitskii, J. R. Lomeda, A. Dimiev, B. K. Price, and J. M. Tour, “Longitudinal unzipping of carbon nanotubes to form graphene nanoribbons,” *Nature*, vol. 458, pp. 872–876, Apr. 2009. (Cited on page 68)

[183] J. Cai, P. Ruffieux, R. Jaafar, M. Bieri, T. Braun, S. Blankenburg, M. Muoth, A. P. Seitsonen, M. Saleh, X. Feng, K. Mullen, and R. Fasel, “Atomically precise bottom-up fabrication of graphene nanoribbons,” *Nature*, vol. 466, pp. 470–473, July 2010. (Cited on page 68)

[184] J. Bai, X. Zhong, S. Jiang, Y. Huang, and X. Duan, "Graphene nanomesh," *Nat. Nanotechnol.*, vol. 5, pp. 190–194, Mar. 2010. (Cited on page 69)

[185] M. Kim, N. S. Safron, E. Han, M. S. Arnold, and P. Gopalan, "Fabrication and Characterization of Large-Area, Semiconducting Nanoperforated Graphene Materials," *Nano Lett.*, vol. 10, no. 4, pp. 1125–1131, 2010. (Cited on page 69)

[186] T. G. Pedersen, C. Flindt, J. Pedersen, N. A. Mortensen, A.-P. Jauho, and K. Pedersen, "Graphene Antidot Lattices: Designed Defects and Spin Qubits," *Phys. Rev. Lett.*, vol. 100, p. 136804, Apr 2008. (Cited on page 69)

[187] J. Eroms and D. Weiss, "Weak localization and transport gap in graphene antidot lattices," *New Journal of Physics*, vol. 11, no. 9, pp. 095021–, 2009. (Cited on pages 69, 73 and 74)

[188] T. Shen, Y. Q. Wu, M. A. Capano, L. P. Rokhinson, L. W. Engel, and P. D. Ye, "Magnetoconductance oscillations in graphene antidot arrays," *Appl. Phys. Lett.*, vol. 93, no. 12, p. 122102, 2008. (Cited on page 69)

[189] S. Ishizaka and T. Ando, "Classical and Quantum Tranport in Antidot Arrays with Various Periods," *Phys. Low-Dim. Struct.*, vol. 5/6, pp. 5–12, 1999. (Cited on pages 70, 71, 94 and 95)

[190] S. Ishizaka and T. Ando, "Detailed analysis of the commensurability peak in antidot arrays with various periods," *Phys. Rev. B*, vol. 55, pp. 16331–16338, Jun 1997. (Cited on pages 71 and 72)

[191] D. Kozlov, Z. Kvon, A. Plotnikov, and A. Latyshev, "Two-dimensional electron gas in a lattice of antidots with a period of 80 nm," *JETP Letters*, vol. 91, no. 3, pp. 134–138, 2010. (Cited on page 73)

[192] M. Brack and R. K. Bhaduri, *Semiclassical Physics*. Addison-Wesley, 1997. (Cited on page 73)

[193] J. J. Sakurai, *Modern Quantum Mechanics*. Addison-Wesley, 1994. (Cited on page 73)

[194] E. McCann, K. Kechedzhi, V. I. Fal'ko, H. Suzuura, T. Ando, and B. L. Altshuler, "Weak-Localization Magnetoresistance and Valley Symmetry in Graphene," *Phys. Rev. Lett.*, vol. 97, p. 146805, Oct 2006. (Cited on page 73)

[195] G. Datseris, R. Fleischmann, and T. Geisel . Personal communication and provision of unpublished data. Used in this thesis with permission of the authors. (Cited on pages 74, 75, 76, 77, 95 and 104)

[196] J. G. Pedersen and T. G. Pedersen, “Hofstadter butterflies and magnetically induced band-gap quenching in graphene antidot lattices,” *Phys. Rev. B*, vol. 87, pp. 235404–, June 2013. (Cited on page 77)

[197] J. Takahara, A. Nomura, K. Gamo, S. Takaoka, K. Murase, and H. Ahmed, “Magnetotransport in Hexagonal and Rectangular Antidot Lattices,” *Jpn. J. Appl. Phys.*, vol. 34, no. 8S, p. 4325, 1995. (Cited on page 77)

[198] J. R. Wallbank, A. A. Patel, M. Mucha-Kruczynski, A. K. Geim, and V. I. Fal’ko, “Generic miniband structure of graphene on a hexagonal substrate,” *Phys. Rev. B*, vol. 87, pp. 245408–, June 2013. (Cited on pages 79, 81, 82 and 86)

[199] M. Lee, J. R. Wallbank, P. Gallagher, K. Watanabe, T. Taniguchi, V. I. Fal’ko, and D. Goldhaber-Gordon, “Ballistic miniband conduction in a graphene superlattice,” *Science*, vol. 353, pp. 1526–, Sept. 2016. (Cited on pages 79, 81, 82 and 86)

[200] R. Decker, Y. Wang, V. W. Brar, W. Regan, H.-Z. Tsai, Q. Wu, W. Gannett, A. Zettl, and M. F. Crommie, “Local Electronic Properties of Graphene on a BN Substrate via Scanning Tunneling Microscopy,” *Nano Lett.*, vol. 11, pp. 2291–2295, June 2011. (Cited on page 81)

[201] R. Krishna Kumar, X. Chen, G. H. Auton, A. Mishchenko, D. A. Bandurin, S. V. Morozov, Y. Cao, E. Khestanova, M. Ben Shalom, A. V. Kretinin, K. S. Novoselov, L. Eaves, I. V. Grigorieva, L. A. Ponomarenko, V. I. Fal’ko, and A. K. Geim, “High-temperature quantum oscillations caused by recurring Bloch states in graphene superlattices,” *Science*, vol. 357, pp. 181–, July 2017. (Cited on pages 82, 84, 85 and 89)

[202] E. Brown, “Bloch Electrons in a Uniform Magnetic Field,” *Phys. Rev.*, vol. 133, pp. A1038–A1044, Feb. 1964. (Cited on page 84)

[203] J. Zak, “Magnetic Translation Group,” *Phys. Rev.*, vol. 134, pp. A1602–A1606, Jun 1964. (Cited on page 84)

[204] R. S. Markiewicz, “The topological significance of saddle point van Hove singularities: a comparison of orbital switching and magnetic breakdown,” *Journal of Physics: Condensed Matter*, vol. 6, no. 16, pp. 3059–, 1994. (Cited on page 86)

[205] G. G. Naumis, “Topological map of the Hofstadter butterfly: Fine structure of Chern numbers and Van Hove singularities,” *Physics Letters A*, vol. 380, no. 20, pp. 1772–1780, 2016. (Cited on page 86)

[206] O. Steffens, T. Schlösser, P. Rotter, K. Ensslin, M. Suhrke, J. P. Kotthaus, U. Rössler, and M. Holland, “From the two-dimensional electron gas to antidot superlattices: magnetoresistance effects in the transition regime,” *Journal of Physics: Condensed Matter*, vol. 10, no. 17, pp. 3859–, 1998. (Cited on page 94)

[207] D. Weiss, K. Richter, E. Vasiliadou, and G. Lütjering, “Magnetotransport in antidot arrays,” *Surface Science*, vol. 305, no. 1, pp. 408–418, 1994. (Cited on page 94)

[208] G. M. Gusev, Z. D. Kvon, V. M. Kudryashov, L. V. Litvin, and Y. V. Nastaushev, “Magnetoresistance oscillations in a 2D electron system with a periodic potential of antipoints,” *JETP letters*, vol. 54, no. 7, pp. 364–368, 1991. (Cited on page 94)

[209] M. Drienovsky, F.-X. Schrettenbrunner, A. Sandner, D. Weiss, J. Eroms, M.-H. Liu, F. Tkatschenko, and K. Richter, “Towards superlattices: Lateral bipolar multibarriers in graphene,” *Phys. Rev. B*, vol. 89, p. 115421, Mar 2014. (Cited on page 94)

[210] S. de Haan, A. Lorke, R. Hennig, M. Suhrke, W. Wegscheider, and M. Bichler, “Magnetotransport properties of arrays of cross-shaped antidots,” *Phys. Rev. B*, vol. 60, pp. 8845–8848, Sep 1999. (Cited on page 95)

[211] T. Azuma and T. Osada, “Antidot shape dependence of the commensurability oscillation of magnetoresistance in two-dimensional antidot arrays,” *Physica B: Condensed Matter*, vol. 256, pp. 397–400, 1998. (Cited on page 95)

[212] R. R. Gerhardts, “Self-consistent transport equations for the electron-impurity system in a magnetic field,” *Zeitschrift für Physik B Condensed Matter*, vol. 22, no. 4, pp. 327–336, 1975. (Cited on page 98)

[213] J. Heremans, B. K. Fuller, C. M. Thrush, and V. Bayot, “Temperature dependence of the magnetoresistance of $\mathrm{In}_x\mathrm{Ga}_{1-x}\mathrm{As}$ antidot lattices,” *Phys. Rev. B*, vol. 54, pp. 2685–2690, July 1996. (Cited on page 101)

[214] A. Matulis and F. M. Peeters, “Appearance of enhanced Weiss oscillations in graphene: Theory,” *Phys. Rev. B*, vol. 75, pp. 125429–, Mar. 2007. (Cited on page 101)

[215] M.-H. Liu, C. Gorini, and K. Richter, “Creating and Steering Highly Directional Electron Beams in Graphene,” *Phys. Rev. Lett.*, vol. 118, pp. 066801–, Feb. 2017. (Cited on page 104)

# Acknowledgments

An dieser Stelle möchte ich mich bei all jenen bedanken, die zum Erfolg dieser Arbeit maßgeblich beigetragen haben:

- Zuerst Prof. Dr. Dieter Weiss, der mir die Arbeit an diesem interessanten Thema ermöglichte, immer ein offenes Ohr für Probleme aller Art hatte und stets am Fortschritt meiner Arbeit interessiert war.

- Besonderer Dank gilt Dr. Jonathan Eroms, der mir als Leiter der Graphen Arbeitsgruppe stets mit Rat und Tat zur Seite stand und praktisch immer eine Lösung parat hatte. Vielen Dank für die freundliche und vertrauensvolle Zusammenarbeit.

- Prof. Dr. Christian Schüller für die Übernahme des Zweitgutachtens meiner Dissertation.

- Prof. Dr. Christoph Strunk und seiner ganzen Arbeitsgruppe für die Bereitstellung und Erlaubnis zur Nutzung verschiedenster Geräte, unter anderem der RIE-Ätzanlage, ohne die meine Arbeit nicht möglich gewesen wäre.

- Prof. Dr. Ming-Hao Liu, der stets mit produktiven Gesprächen und Diskussionen Unterstützung anbot und wichtige Simulationen und Rechnungen zu unseren Experimenten liefern konnte.

- Dr. Ragnar Fleischmann und George Datseris vom Max Planck Institute for Dynamics and Self-Organization, die wichtige Simulationen und Erklärungen zu unseren Antidot-Experimenten beitragen konnten.

- Meinen beiden Master-Studenten Tobias Preis und Andreas Lex, mit denen eine hervorragende Zusammenarbeit möglich war und deren experimentelle Arbeit unsere Forschung deutlich voran brachte. Insbesondere die gemeinschaftliche Optimierung des Transferprozesses und der nachfolgenden Prozessierungsschritte zusammen mit Tobias Preis war für diese Arbeit unabdingbar. Zusätzlich gilt mein Dank Anne-Marie Lang, Tobias Lindner und Philipp Bauer, die im Rahmen ihrer Bachelorarbeiten wichtige Projekte übernahmen und mich damit sehr unterstützten.

- Bei der gesamten Graphen-Gruppe. Insbesondere bei Martin Drienovsky mit dem ich stets über verschiedenste Probleme bei der Prozessierung und Auswertung unserer Proben diskutieren konnte. Zudem warst Du eine stets angenehme "Begleitung" auf verschiedenen Dienstreisen.

- Allen Kollegen am Lehrstuhl Weiss, speziell meinen Bürokollegen Martin, Franz, Ralf und Jonas, für die nette Zusammenarbeit. Besonderer Dank natürlich auch an Kutschi, Robin, Stefan, Hupfi, Tobias, Thomas, Mo, Basti, Mariusz und vielen anderen, mit denen ich auch außerhalb der Arbeitszeiten einige Zeit verbringen konnte, sei es beim Grillen, Stammtisch oder einem Feierabend-Bier.

- Bei unseren beiden Sekretärinnen Claudia und Elke für das angenehme Arbeitsklima und die stetige Hilfsbereitschaft bei allen bürokratischen Anliegen.

- Den Technikern Uli, Flo, Daniel, Michl und Tom, die mich mit ihrer freundlichen und hilfsbereiten Art bei verschiedensten Problemen im Reinraum und anderen Laboren unterstützten.

- Meinen Freunden außerhalb der Uni, die immer für Abwechslung und Aufheiterung sorgten und mit denen ich viele unvergessliche Stunden verbrachte.

- Meinem Bruder Tobias und meiner Schwester Theresa, die meine Arbeit stets interessiert verfolgten und unterstützen.

- Vor allem meinen Eltern, die mich mit Geduld und Verständnis in jeder Hinsicht unterstützten. Ohne deren Hilfe wäre mein Studium und die Promotion nicht möglich gewesen und ich hätte es niemals so weit geschafft.